Investigation into wakes generated by surface piercing periscopes

by
Alexander Stefan Terry Conway, BE (Hons) (Naval Architecture)

National Centre for Maritime Engineering and Hydrodynamics
Australian Maritime College

Submitted in fulfilment of the requirements for the degree of Doctor of Philosophy
University of Tasmania

October 2017

Declarations

Declaration of Originality

This thesis contains no material which has been accepted for a degree or diploma by the University or any other institution, except by way of background information and duly acknowledged in the thesis, and to the best of the my knowledge and belief no material previously published or written by another person except where due acknowledgement is made in the text of the thesis, nor does the thesis contain any material that infringes copyright.

Alexander Stefan Terry Conway (Date: 31/10/2017)

Authority of Access

This thesis may be made available for loan and limited copying and communication in accordance with the Copyright Act 1968.

Statement regarding published work contained in thesis

The publishers of the papers comprising Chapters 3 to 6 hold the copyright for that content, and access to the material should be sought from the respective journals. The remaining non published content of the thesis may be made available for loan and limited copying and communication in accordance with the Copyright Act 1968.

Statement of Co-authorship

Where the candidate has co-authored a published paper that is included in the body of the text or is included in whole or in part in the appendix, a statement of authorship has been prepared by the candidate's supervisors for inclusion in the thesis.

Statements of Published work contained in thesis

The following people and institutions contributed to the publication of work undertaken as part of this thesis:

Alexander Stefan Terry Conway, University of Tasmania = **Candidate**

Prof. Dev Ranmuthugala, University of Tasmania, Supervisor = **Author 1**

Assoc. Prof. Jonathan Binns, University of Tasmania, Supervisor = **Author 2**

Prof. Martin Renilson, University of Tasmania, Supervisor = **Author 3**

Brendon Anderson, Defence Science and Technology Group = **Author 4**

Sarah Cathcart, University of Tasmania = **Author 5**

Author details and their roles:

Paper 1, Predicting surface wakes using LES and RANS-SST analysis:

Located in chapter 3

Candidate was the primary author on this paper. Author 1, Author 2 contributed with refinement and presentation

[Candidate : 80%, Author 1 : 9%, Author 2 : 11%]

Paper 2, Experimental analysis of surface piercing cylinder at high Froude numbers:

Located in chapter 4

Candidate was the primary author on this paper. Author 5 contributed to assistance in assembling and conducting the experiments. Author 1, Author 2, Author 3 and Author 4 contributed to the refinement and presentation

[Candidate : 72.5%, Author 5 : 10%, Author 1 : 5%, Author 2 : 5%, Author 3 : 5%, Author 4 : 2.5%]

Paper 3, The end effect of surface piercing cylinders with and without an end body:

Located in chapter 5

Candidate was the primary author on this paper. Author 1, Author 2, Author 3 and Author 4 contributed to the refinement and presentation

[Candidate : 75%, Author 1 : 7.5%, Author 2 : 7.5%, Author 3 : 7.5%, Author 4 : 2.5%]

Paper 4, The effect of geometry on the surface waves generated by vertical surface piercing cylinders with a horizontal velocity:

Located in chapter 6

Candidate was the primary author on this paper. Author 1, Author 2 and Author 3 contributed to the refinement and presentation

[Candidate : 77.5%, Author 1 : 7.5%, Author 2 : 7.5%, Author 3 : 7.5%]

We the undersigned agree with the above stated "proportion of work undertaken" for each of the above published (or submitted) peer-reviewed manuscripts contributing to this thesis:

Signed: _____ _____

Prof. Dev Ranmuthugala	Assoc. Prof. Michael Woodward
Supervisor	Director
National Centre for Maritime Engineering and Hydrodynamics	National Centre for Maritime Engineering and Hydrodynamics
University of Tasmania	University of Tasmania

Date: 15/06/2017 19/06/2017

Acknowledgements

The completion of this thesis marks a huge milestone and thus, it is with great pleasure to thank the many people who have made this thesis possible.

Firstly, I wish to thank my supervisors, Prof. Dev Ranmuthugala, Assoc. Prof. Jonathan Binns and Dr Martin Renilson, who provided feedback, direction, advice, insight and great technical and editorial advice well beyond my expectations and created a positive environment in which I could complete this project. I would also like to thank my colleagues and friends from AMC who created a friendly environment for the work. In particular, Zhi Leong, Arno Dubois, Max Haase, Konrad Zurcher, Alex Briggs, Phillip Marsh and Ahmed Swidan.

Special thanks must go to:

- Dr Brendon Anderson from the Defence Science and Technology Group (DST) for his technical and financial support throughout the entire project
- Luciano Mason and Geli Kourakis for their experience and non-stop work on the High Performance Cluster (HPC) without which the Computational Fluid Dynamics work completed during this project would not have been possible
- The entire team working in the Australian Maritime College Tow Tank for their support and guidance in setting up and performing the experimental work presented below. In particular, Tim Lilienthal, Jock Fergusson, A/Professor Gregor Macfarlane, Dr Jonathan Duffy and Michael Underwood

I would also like to thank my family for their support which allowed me to start and complete this thesis. Finally, Pip, thank you for your support and patience during the writing of this thesis.

Abstract

For operational purposes, submarines are required to pierce the free surface with masts, such as periscopes and snorkels. These masts generate a large plume structure which can significantly increase the chance of detection. This thesis develops a numerical technique to accurately model the plume structure generated by a mast piercing the free surface, examining four critical aspects: bow wave height, plume height, plume length, and drag coefficient. The Computational Fluid Dynamics (CFD) model was validated through an experimental programme in a towing tank and against published data. The numerical validation showed that CFD-RANS modelling failed to predict the plume height and plume length while the CFD-LES accurately modelled the plume structure under Froude numbers of 3.0, whilst predicting the overall shape with a small under prediction at Froude numbers greater than 3.0.

The results show aspects of the flow regime within the plume structure and experimental configurations required to accurately replicate real world scenarios. The most critical flow characteristic found for the plume structure was the combination of two flow regimes within the plume structure. The forward section of the plume is generated by the bow wave, whilst the aft section is caused by the submerged section of the mast.

When replicating the mast using a surface piercing cylinder with no end body, it was found that an immersion to depth ratio greater than eight is required to avoid end effects. Additionally, the use of an end body can effectively reduce the impact of the end effect on the plume structure.

Utilising the validated numerical model, several mast configurations were tested in order to reduce the plume signature. Cylindrical double mast configurations and streamlined NACA0012 mast configurations were tested showing potential reductions of the overall plume size. This data can be used to improve the submarine mast configuration, thus reducing the risk of detection due to the generation of a large plume structure.

Table of Contents

List of Figures

List of Tables

Nomenclature

η_b	Bow wave height
C_D	Coefficient of drag
σ	Coefficient of surface tension
A	Cross sectional area
D	Cylinder diameter
ρ	Density
∇	Divergence
μ	Dynamic viscosity
p	Fluid pressure
u_τ	Friction velocity
Fr	Froude number
g	Gravity
T	Immersion depth
T'	Immersion ratio
v	Kinematic viscosity
η_b'	Non-dimensional bow wave height
η_p'	Non-dimensional plume height
λ'	Non-dimensional plume length
y^+	Non-dimensional wall distance
η_p	Plume height
λ	Plume length
Re	Reynolds number
υ_{SGS}	SGS eddy viscosity
S_t	Strouhal number
BL	Turbulence decay
ϵ	Turbulent dissipation
k	Turbulent kinetic energy
U	Velocity
U_z	Velocity in vertical axis (z-axis)

f_v	Vortex shedding frequency
y	Wall distance

Chapter 1

Thesis Introduction

1.1 Introduction

The ability of a submarine to transit and complete tasks without detection is critical to the success of its missions. During these phases, submarines, especially conventional powered boats, are required to approach and pierce the surface with a bluff body such as a periscope for surveillance or a snorkel to operate its diesel engines to recharge its batteries (Figure 1.1). The use of these vertically mounted appendages present a significant signature issue whilst the submarine maintains a forward velocity as they can generate large plumes and wakes that are detectable by a number of methods such as visual sighting or radar (Figure 1.2). Modern sensors allow these signatures to be detected at significant distances and from a variety of platforms, such as ships and aircrafts. Detection can seriously jeopardise the submarine's mission.

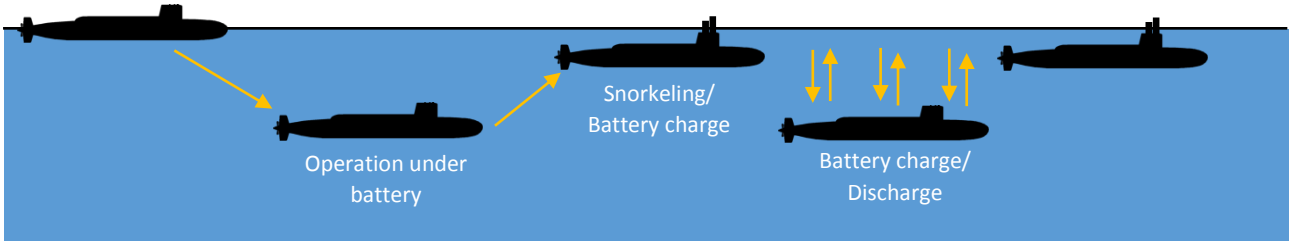

Figure 1.1: Typical conventional submarine snorkeling cycle in order to recharge batteries.

Figure 1.2: Plume and wake generated by a submarine whilst snorkeling (DailyMail, 2012).

In order to quantify the visual signature created by the plume and wake, it is essential to develop validated numerical simulation models that can accurately predict the signature at different configurations and conditions. This will enable designers to optimise the mast configuration and provide the submarine crew with operational envelops to reduce detection. However, there is very little information in the public domain on the flow regimes and wake generation of bluff bodies piercing the free surface in the speed range within which submarines usually operate at periscope or snorkelling depths. Thus, there is little information and understanding on how to improve the design and configuration of these masts to reduce the wake generated by them and in turn reduce the risk of detection. As will be discussed in the following sections, the flow around a bluff body becomes complex as the flow regimes become turbulent, thus increasing the difficulty in studying and understanding the flow. Therefore, a combination of numerical and experimental data representing surface piercing bluff bodies at different forward speeds is required.

1.2 Problem Definition

Given that the success of a mission can depend on manoeuvring without detection, understanding the size and shape of the plume at given speeds and configurations can provide information and guidelines to operational procedures whilst snorkelling or with the periscope extended.

The plume and wake generated by a bluff body piercing the free-surface is a complex flow problem which is a significant area of interest for submarine operations. Whilst the wake generated by a bluff body has been studied both experimentally (Hay, 1947; Metcalf et al., 2006; Slaouti et al., 1981) and numerically (Kawamura et al., 2002; Yu et al., 2008), there is very little information in the public domain at the speed range required to accurately represent the conditions in which a submarine operates near the free surface. Due to the differences in mast diameter used for each set of published data, to compare the results, the diameter based Froude number (*Fr*) was used to generate non-dimensional results. The Froude number is defined in equation (1.1).

$$Fr = \frac{U}{\sqrt{gD}} \tag{1.1}$$

Where *Fr* is Froude number, *U* is the forward velocity, *g* is acceleration due to gravity, and *D* is the diameter of the mast. The corresponding Froude numbers for a submarine at snorkeling/periscope speeds are up to *Fr*=4. Hay (1947) published an extensive range of experimental data up to *Fr*=4.9 using a cylinder with a relatively short depth to the submerged free end (*T'* = 2.0). *T'* is the immersion depth ratio and is defined in Equation (1.2) where *T* is the immersion depth and *D* is the cylinder diameter.

$$T' = \frac{T}{D} \tag{1.2}$$

Whilst the speeds tested by Hay are sufficient to study the flow in relation to the required speed range, the limited submerged depth could result in a reduction in the plume size due to end effects as suggested by Slaouti et al. (1981). These researchers investigated the submerged end effects on the wake generated by a surface piercing cylinder at low Froude numbers. Metcalf et al. (2006) investigated the wake generated by NACA sections at Froude numbers of 0.19, 0.37, and 0.55. Kawamura et al. (2002) investigated the surface waves and vortex shedding using Computational Fluid Dynamics (CFD) - Large Eddy Simulation (LES) and a circular cylinder at Froude numbers of 0.2, 0.5, and 0.8. Other researchers, Yu et al. (2008), also used LES, however, investigated the bow wave height generated by a cylinder up to a Froude number of 3.0. Although this was the greatest Froude number investigated using numerical simulations, the bow wave height was significantly under estimated above Fr=2.0.

It would be possible to study the hydrodynamic characteristics of a submarine mast using an experimental approach through model scale and full scale testing. However, these methods require considerable time and cost, in addition to requiring access to appropriate test and measuring facilities. The complexity, and thus the time and cost increases significantly with the addition of different set-up configurations and conditions. Additional restrictions which are encountered using an experimental approach include speed limitations, depth restrictions, and difficulty to accurately replicate the real world scenarios, in particular, the end effect when the mast is modelled without the submarine. Although full scale testing can be used, they present further complications such as the need to develop

appropriate test rigs and/or access to full scale platforms, while model scale results require appropriate scaling to relate to full scale operations.

Considering these constraints, it is apparent that a purely experimental approach cannot easily solve for all the potential objectives of this project, however its combination with numerical modelling has the potential to reduce or remove the limitations of the experimental approach. As a result of the advances in high performance computing, the capability and accuracy of CFD simulations are continuously increasing with the availability of computational resources and more advanced software (Boysan et al., 2009). However, even with these significant improvements, attempting to generate the most accurate results, especially when dealing with complex flow structures, can result in the computational requirements exceeding the available computing capabilities. Therefore it is essential that the correct numerical methods and approaches are selected and the simulation settings and conditions provide accurate and stable results using available resources within acceptable timeframes.

CFD simulations offer a relatively low cost approach to model complex flow structures around bodies undergoing motion, including those piercing the free surface. However, there are a number of different CFD methods and approaches that can be employed, each having different advantages and limitations.

Reynolds Averaged Navier-Stokes (RANS) based CFD simulations have been extensively developed and have proven to accurately predict the forces and moments of bluff bodies at low speeds. The RANS approach uses a time averaged mean value for the velocity field, since it is assumed that the time-dependent turbulent velocity fluctuations can be separated from the mean flow velocity. This results in the need to model the turbulence to produce a closed system of solvable equations, which greatly reduces the computational effort required when compared to methods such as LES and Direct Numerical Simulation (DNS), although the averaging of the turbulence can reduce accuracy and the fluctuations in the flow are modelled rather than solved. An extension of the RANS model is Unsteady RANS (URANS), which has an additional time derivative in each equation. This means that the unsteady flows are not averaged out as done in RANS simulations, and thus turbulence can potentially be modelled with a higher degree of accuracy. However, similar

to steady RANS, it fails to account for the unsteady fluctuations as URANS still does not resolve turbulence (Salim et al., 2011).

Published data (Young et al., 2007) suggests that LES is a more capable method in capturing the flow instabilities in comparison to RANS simulations as the large scale turbulence is resolved rather than modelled, while the smallest scales of the flow are removed through a filtering operation and modelled using sub-grid scale models. This allows the largest and most important scales of the turbulence to be resolved. However, the computational cost increases significantly due to the requirement of a finer mesh used to capture the turbulence and boundary layers.

In addition to CFD simulations reducing the restrictions encountered with experimental work, the former provides access to a range flow visualisation that is limited or restricted in physical experimental work. However, as the results are highly dependent on the numerical models used, the settings employed, and the computational grid, it is a requirement that the numerical results are verified and validated against experimental data.

As there is limited information available with regard to the plume structure and changes in plume size as a result of the submerged end effects, understanding the hydrodynamic flow around a bluff body is an important aspect of this research.

1.3 Research Question and Objective

The aim of this thesis was to characterise through experimental work and numerical modelling the flow created by a moving submarine snorkel and/or periscope piercing the free surface, in order to predict the resulting plume structure. Furthermore, the changes in the plume size due to experimental limitations, such as limited mast depth, and potential configurations or operational conditions to reduce the size of the plume and thus detection were studied. The motivation for this research was to provide a method in which the plume structure generated by the submarine appendage could be accurately modelled numerically, which would enable further development of the design and configuration to

reduce the associated wake and thus reduce the risk of detection. Therefore, the research question was:

Can the plume structure generated by a submarine appendage piercing the free surface operating at snorkeling/periscope speeds be numerically accurately modelled with respect to the plume shape?

To achieve the research question the following set of objectives were developed:

- Generate a set of experimental results containing the plume size for a range of speeds corresponding to a typical submarine operating at snorkeling/periscope depth speeds for numerical validation.
- Using CFD to accurately model the plume structure generated by a submarine mast piercing the free surface using visual plume size and drag forces for validation.
- Quantify the change in bow wave height and plume size as a result of the submerged end effects.
- Assess possible changes in the mast design and configuration which could reduce the risk of detection through reducing the plume size.

1.4 Methodology

In order to achieve the objectives outlined above, the research project was divided into the following phases:

- Conduct a literature review on the hydrodynamic flow around a cylinder and the potential numerical models which could be used to model the plume generated by a submarine appendage.
- Assess the ability of CFD to model and capture the flow characteristics around a bluff body piercing the free surface and a selection of an appropriate numerical approach such as LES or URANS models.
- Conduct experimental work to generate validation data for a surface piercing cylinder. The experimental approach needed to include varying the length of the

cylinder as well as the addition of a submerged end body to provide a set of data to study the changes in plume size due to the submerged end effects.

- Development of a validated CFD model to predict and model the plume and wake generated by a submarine snorkel and/or periscope and assessment of the sensitivity of the numerical model in detecting the changes in plume size due to variations of the submerged end condition.
- Utilisation of the validated CFD model for development of designs and configurations which reduced the risk of detection due to a surface piercing snorkel and/or periscope. This included the use of multiple smaller masts or non-cylindrical cross sectional masts.

1.5 Research Considerations

This study focused on the plume dimensions generated by a surface piercing appendage such as a periscope or snorkel from a submarine moving under the free surface. In line with the work pioneered by Hay (1947), the size of the plume was investigated using three main dimensions shown in Figure 1.3, i.e. the bow wave height (η_b), plume height (η_p), and plume length (λ). In addition to the plume size, the drag coefficient of the mast due to the fluid interaction was used to increase the parameters in the numerical validation process.

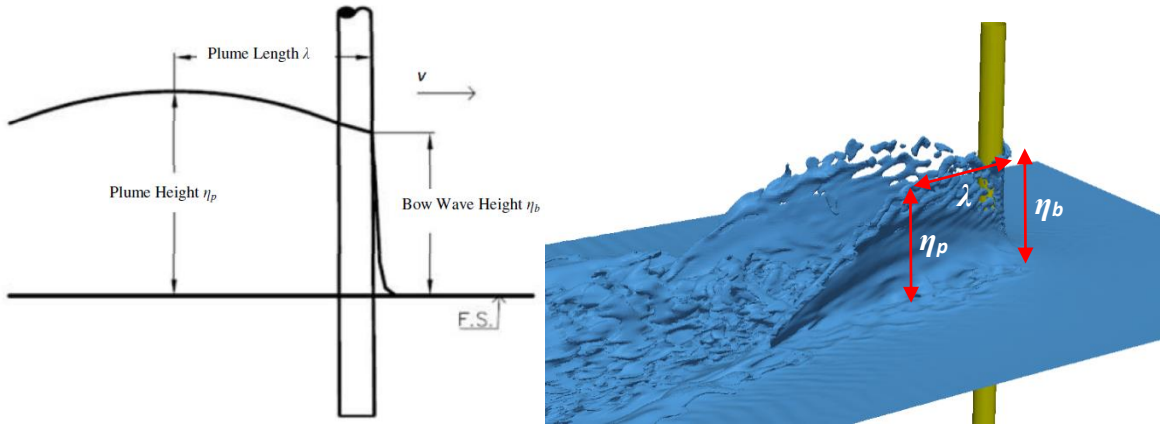

Figure 1.3: Parameters used for measurement of plume dimensions, bow waveheight, plume height and plume length.

The study used a cylinder diameter of 100mm with all non-dimensional data based on either the frontal area, diameter, or water-plane area of the cylinder. Furthermore, for mast optimisations, it was considered that the area of the mast(s) was a set requirement and thus the water-plane area remained constant. Figure 1.4 shows the range of mast geometries assessed to reduce the plume size as a results of mast optimisations. This included the double mast configurations and streamlined cross sectional masts. The former were tested as it was presumed that a smaller mast would generate a smaller plume profile and thus by dividing the required area of a mast between two smaller masts, a reduction in overall plume size should be possible. In addition, the wake from the forward mast may reduce the plume profile generated by the aft mast. Conventionally, submarines have used cylindrical masts, however, the possibility for use of streamlined bodies has the potential to greatly reduce the plume profile and therefore, a single and a double truncated NACA section was also analysed.

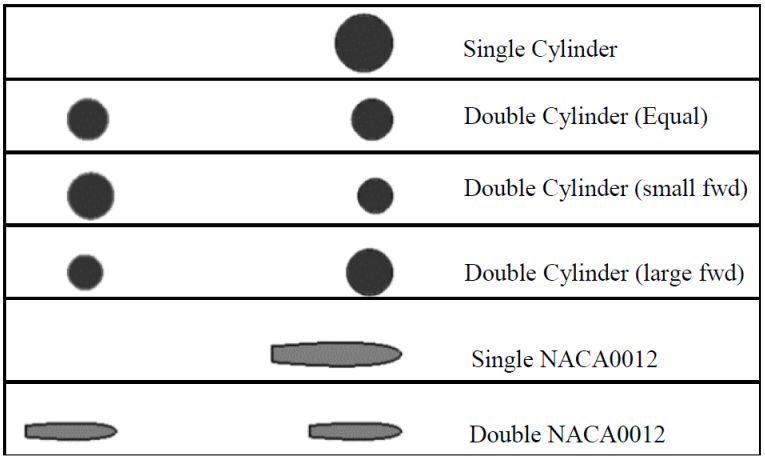

Figure 1.4: Variation of mast geometries used to analyse possible reductions in plume size to decrease risk of submarine detection (note: for a constant water-plane area).

1.6 Novel Aspects of the Project

As mentioned earlier, the flow around a bluff body piercing the free surface is extremely important for submarine operations as this can increase the risk of detection. Thus, it is essential that the flow can be accurately modelled and a good understanding of the flow regime around the body is acquired. However, very little information is available in the public domain on research carried out on the wake and plume generated by bluff bodies at the required operational conditions of a submarine. Thus, this project provides original contributions to the field of experimental hydrodynamics and CFD in the following three areas:

- The flow around a bluff body piercing the free surface at submarine snorkeling/periscope speeds has had very little research completed using experimental or real-world data. Hay (1947) generated an extensive amount of data using still imagery of a range of cylinder sizes at speeds up to and greater than that required for this project (i.e. up to Fr=4.6). However, the results presented by Hay were limited to a very short submerged cylinder depths, and thus the change in cylinder drag and plume size as a result of submerged end effects were unknown. Slaouti et al. (1981) highlighted this, and stated that the end effects would influence both the bow wave height and drag coefficient of the cylinder. There are several

other examples of experiments using cylinders piercing the free surface (Chaplin et al., 2003; Hsieh, 1964; Lang et al., 2000), however, they concentrate on a much lower Froude number range than required to assist in the design of surface piercing masts of submarines operating near the surface. Therefore, developing a set of experimental results with a cylinder of significant submerged length would provide experimental data which could be used either as raw data for further research conducted on bluff bodies piercing the free surface or numerical validation for simulation models developed to examine variations in the geometry and configuration of such masts.

- The development of a numerical simulation model for cylinders piercing the free surface at Froude numbers which correlate to typical submarine snorkeling/periscope speeds to study the flow and hydrodynamic characteristics. Similar to the experimental data, there is little information of numerical data of a bluff body piercing the free surface (Avital et al., 2009; Kawamura et al., 2002; Yu et al., 2008) in the public domain. However, no numerical simulation results are currently available at the required Froude number range.

- The end effects of a flow over a three dimensional body is a well-known flow phenomena (Slaouti et al., 1981), which can alter the comparison of experimental data to real world scenarios. The quantification of the end effects using both experimental and numerical data would allow both currently published data and future results to be post-processed such that the data will represent real world applications.

1.7 Outline of the thesis

This thesis comprises scientific papers supplemented by supporting chapters, which follow a 'chapterised thesis' structure as outlined below.

Chapter 1: The introduction chapter outlines the research questions, aims, methodology, and novel aspects of the thesis.

Chapter 2: A summary of the flow around a cylinder and various numerical models are discussed in this chapter. The benefits and negatives of each model are presented to determine the numerical models applicable for use throughout this thesis.

Chapter 3: This chapter established the possibility of using CFD to generate and model the plume structure generated by a cylinder piercing the free surface using the open source CFD package OpenFOAM. A comparison between two fundamentally different numerical models was performed to assess the most applicable model for future CFD simulations. The results from a RANS model using the k-ω SST turbulence model and an LES model were compared against available published data. The methodology and key findings from this study were used to develop the CFD results and generate a complete set of simulations with varying mast geometries in the following chapters.

Chapter 4: This chapter focused on establishing a set of experimental data which investigated the plume size generated in comparison to published data for a cylinder with relatively short immersion depth. The immersed cylinder length was then extended to investigate the differences between the previously published data and potential real-world results. The data obtained from this chapter was used to validate the numerical code used in Chapter 5 and 6 whilst also providing insight and information required for further experimental work.

Chapter 5: Using the findings from the previous experimental programme and the numerical results, the former was expanded to improve and increase the data collected. This included improved measurements of the plume structure and an improved test rig to measure and calculate the drag coefficient of the immersed cylinder. The latter enabled the further validation of the numerical simulations as well as providing data on the drag

generated by the different configurations. This chapter also investigates the change in plume size due to immersed end effect using both an experimental and numerical approach through the addition of a streamlined end body to both the short and long immersed cylinders. This enabled the variation of the plume size due to the end effects to be quantified.

Chapter 6: With the addition of the experimental results generated from Chapters 4 and 5, and the methodology and findings from the numerical investigation in Chapter 3, the plume structure was studied in closer detail using the CFD-LES model. This was validated against the experimental data, both for the short and long immersion depths, thus allowing the numerical set-up to be utilised for varying mast geometries and configuration to reduce the plume size and hence the risk of detection. Each mast configuration maintained the same water-plane area as this was considered an operational requirement. The configurations tested included double mast set-ups, where a secondary mast was located aft of the first mast, and streamlined mast shapes. The findings showed that the numerical models were able to model the plume structure generated by a submarine's mast as well as providing a potential decrease in the plume structure through the use of a suitable double mast configuration.

Chapter 7: During the experimental work and numerical validation included in the previous chapters, a constant under prediction of the bow wave height and plume height was recorded. This chapter investigates the stagnation pressure predicted by the numerical models as the major contributing factor. Additionally, the requirements for the cell aspect ratio required to accurately model the spray within the plume structure were studied and discussed.

Chapter 8: This is the concluding chapter and provides a brief summary of the project followed by the body of the chapter that collates the findings and outcomes from the various chapters. These conclusions are then discussed in terms of the implications of the research and possible future work to address issues raised within the project, and to allow further development of options to reduce the plume structure and thus detection.

Appendix I: This appendix presents the data collected from the towing tank experiments with regard to bow wave height to establish the percentage of experimental error.

Appendix II: This contains a conference paper presented at *PACIFIC 2015 International Maritime Conference.* The paper summarises the data presented in Chapters 4 and 6 with an emphasis on the application for submarines.

Appendix III: This contains a conference paper published in the conference proceedings for *RINA Warship 2017*. This paper summarises the data presented in Chapters 5 and 6 with an emphasis on reducing the plume structure for submarines.

Chapter 2

Flow Characteristics and Numerical Modelling

2.1 Flow around a cylinder

This thesis concentrates on the wake and plume structure generated by a surface piercing cylinder and thus published data and studies concerning the plume size will be discussed in the appropriate chapters. However, the flow around a cylinder is critical to understand the fluid dynamics of the situation and how it will affect both the numerical and experimental set ups.

The flow around a cylinder changes characteristics at different Reynolds number. As the Reynolds number increases, the flow changes from a completely laminar flow to a turbulent flow in stages. The stages are outlined in the Table 2.1. The CFD simulations are required to be versatile and robust to enable the changing flow regimes to be accurately captured whilst the experimental set-up is required to withstand each natural frequency generated by the cylinder. Submarines require a speed of approximately two knots as a minimum speed for control and an average speed of around 5 - 10 knots whilst snorkelling (Dawson, 2014). The corresponding flow regimes have been highlighted in yellow in Table 2.1. The significant information here for the numerical modelling is the change in boundary layer flow and separation point. As can be seen, the lower speeds have a laminar boundary layer whilst at the higher Reynolds number, the boundary layer and separation point become turbulent. In terms of designing the experimental set-up, the change in wake profile, as seen in the furthest right column, a sudden generation of turbulent vortex shedding begins at $Re=3.5x10^5$ which suddenly increases the frequency imposed on the cylinder and experimental rig. Therefore, the natural frequency of the rig became a critical feature of the experimental design for two reasons. Firstly, to prevent failure of the rig, and secondly, in order to ensure the rig was structurally rigid in the locations the load cells were positioned.

Table 2.1: Stage of flow around a cylinder (Sumer et al., 1997). The flow regimes of interest to a typical periscope have been highlighted in yellow.

Reynolds Number	**Flow**	
>40	Vortex shedding begins	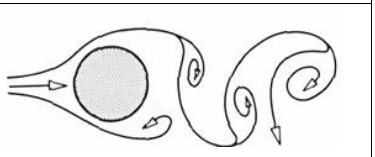
40-200	Vortex shedding is laminar	
200-300	Transition to turbulent vortex shedding	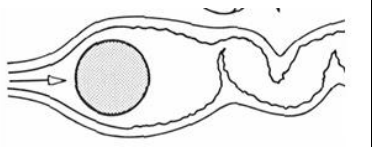
400	Vortices become turbulent	
300 - 3×10^5	Laminar boundary layer separation	
3×10^5 - 3.5×10^5	Transition phase. Laminar boundary layer with turbulent boundary layer separation	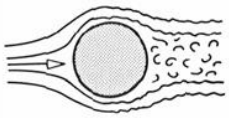
3.5×10^5 - 1.5×10^6	Boundary layer becomes partially turbulent	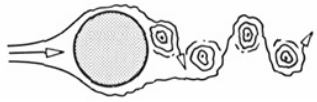
>1.5×10^6	Boundary layer becomes fully turbulent	

2.2 Numerical modelling

There are several different methods which can be used to perform numerical simulations with the most commonly used method derived from the Navier Stokes equations. Therefore, to select the correct numerical model for this project, the main difference along with the potential benefits must be examined. The two most common methods, Reynolds Averaged Navier Stokes (RANS) and Large Eddy Simulation (LES), will be discussed and used for this thesis.

The main difference between the two models mentioned above is the method with which the turbulence is resolved/modelled and thus the accuracy and computational

requirements of the simulations differ. Each of these models are described below to a certain degree with derivation of the Navier Stokes equations which has been well established (Cengel et al., 2010)

2.3 Navier Stoke equations

The Navier Stokes equations are derived from Newton's second law of motion of fluids and are always solved with the continuity equation. The conservation of mass states that the rate of increase of mass within a closed volume must be equal to the mass flow rate into and out of the closed volume. The conservation of mass can be written as:

$$\dot{m}_{in} - \dot{m}_{out} = \frac{\partial}{\partial t} m_{element} \tag{2.1}$$

Whilst the continuity equation can be expressed as:

$$\frac{\partial u}{\partial x} + \frac{\partial v}{\partial y} + \frac{\partial w}{\partial z} = 0 \tag{2.2}$$

The momentum equation is also required for the derivation of the Navier Stokes equations. In Cartesian coordinates for the x-component it can be expressed as:

$$\rho \frac{Du}{Dt} = \rho g_x + \frac{\partial \sigma_{xx}}{\partial x} + \frac{\partial \sigma_{yx}}{\partial y} + \frac{\partial \sigma_{zx}}{\partial z} \tag{2.3}$$

Using the above equations for continuity and momentum, several assumptions can be made such that they can be used in CFD analysis. These assumptions include:

- Fluid flow is Newtonian
- The viscous stress gradients are proportional to the velocity gradients
- Fluid is isotropic or independent of direction

Since the CFD analysis used in this thesis assumes that the fluid is incompressible, the Navier Stokes in vector form becomes:

$$\rho \frac{Dv}{Dt} = -\nabla \rho + \rho \vec{g} + \mu \nabla^2 \cdot \vec{v} \tag{2.4}$$

Therefore, the x-component of the incompressible Navier Stokes equation is:

$$\rho\left(\frac{\partial u}{\partial t}+u\frac{\partial u}{\partial x}+v\frac{\partial u}{\partial y}+w\frac{\partial u}{\partial z}\right)=-\frac{dP}{dx}+\mu\left(\frac{\partial^2 u}{\partial x^2}+\frac{\partial^2 u}{\partial y^2}+\frac{\partial^2 u}{\partial z^2}\right)+\rho g_x \qquad (2.5)$$

2.4 Reynolds Average Navier Stokes (RANS)

Reynolds Average Navier Stokes equations use two additional equations to the NS equations in order to model the fluid flow. To reduce the computational requirements of the simulations, a set of equations is used to model the turbulence and thus allowing a coarser grid which does not need to resolve the turbulent features.

Within the RANS-based turbulence models there are several different models. Two of these include the *k*-epsilon and *k*-omega models. These two models are the most common type of turbulence models currently used which are both two equation models. Two equation models use two extra equations which allows them to account for the effects of turbulent energy. Both the *k*-epsilon and *k*-omega use the turbulent kinetic energy term *k* which determines the energy in the turbulence. The second term for the k-epsilon model is the turbulent dissipation, ε. The second term for the *k*-omega model is the specific dissipation, ω. The second term in both cases determines the scale of the turbulence.

2.4.1 k-epsilon model

This model has been regarded to be useful for free-shear layer (Bardina et al., 1997), with small pressure gradients offering a good compromise between accuracy and robustness. However, due to the limitations in the equations, the *k*-epsilon model is not recommended for:

- Flow which is subject to boundary later separation
- Flows which contain a sudden change in the mean strain rate
- Flows located in rotating fluids
- Flows travelling over curved surfaces

The turbulent kinetic energy is defined as the change in fluctuations in velocity and the turbulent eddy dissipation is the rate at which these velocity fluctuations dissipate. These equations are expressed as:

For the turbulent kinetic energy *k*

$$\frac{\partial}{\partial t}(\rho k) + \frac{\partial}{\partial x_i}(\rho k u_i) = \nabla\left[\left(\mu + \frac{\mu_t}{\sigma_k}\right) + \nabla k\right] + P_k + P_{kb} - \rho\epsilon \qquad (2.6)$$

For the dissipation ε

$$\frac{\partial}{\partial t}(\rho\epsilon) + \nabla(p\epsilon u_i) = \nabla\left[\left(\mu + \frac{\mu_t}{\sigma_\epsilon}\right) + \nabla\epsilon\right] + \frac{\epsilon}{k}(C_{\epsilon 1}(P_k + C_{3\epsilon}P_b) - C_{\epsilon 2}\rho\epsilon) \qquad (2.7)$$

P_k represents the turbulence production due to viscous forces, P_{kb} and $P_{\epsilon b}$ represent the buoyancy forces. OpenFOAM uses the following values as default for the coefficients:

$$C_\mu = 0.09$$

$$\sigma_k = 1.0$$

$$\sigma_\epsilon = 1.30$$

$$C_{\epsilon 1} = 1.44$$

$$C_{\epsilon 2} = 1.92$$

2.4.2 *k*-omega model

Similarly to the k-epsilon model, the k-omega model uses two equations with the main difference that this model assumes that the turbulent viscosity is linked to both the turbulent kinetic energy and the turbulent frequency. Therefore, the turbulent kinetic energy differs slightly from above.

For the turbulent kinetic energy k

$$\frac{\partial}{\partial t}(\rho k) + \nabla(pku_i) = \nabla\left[\left(\mu + \frac{\mu_t}{\sigma_k}\right) + \nabla k\right] + P_k - \beta'\rho k\omega + P_{kb} \qquad (2.8)$$

For the dissipation ω

$$\frac{\partial}{\partial t}(\rho\omega) + \nabla(p\omega u_i) = \nabla\left[\left(\mu + \frac{\mu_t}{\sigma_\omega}\right) + \nabla\right] + \alpha\frac{\omega}{k}\,P_k - \beta\rho\omega^2 + P_{\omega b} \qquad (2.9)$$

As with the k-epsilon model, P_k represents the turbulence production due to viscous forces, P_{kb} and $P_{\omega b}$ represent the buoyancy forces. OpenFOAM uses the following values as default for the coefficients

$$\beta' = 0.09$$

$$\alpha = \frac{5}{9}$$

$$\beta = 0.075$$

$$\sigma_k = 2$$

$$\sigma_\omega = 2$$

However, the standard k-omega model is very rarely used due to the fact that it is extremely sensitive to the inlet free-stream turbulence properties. The most common k-omega model is the shear stress transport (SST) model. This model combines the k-omega equations with the k-epsilon model by applying the k-omega model to the inner parts of the boundary layer and switching to the k-epsilon model in the free-stream. Therefore, the SST formulation is appropriate for simulations with adverse pressure gradients which require both near wall and far field modelling. Hence, the SST model will be used during Chapter 3 in order to compare against LES models discussed below.

2.5 Large eddy simulation (LES)

Large eddy simulation attempts to accurately predict the dynamics of the large eddies whilst also modelling the small, sub-grid scales of motion (Piomelli et al., 2001). It applies the theory that the large eddies are flow dependent on the geometry and the small eddies are isotropic and more universal. The field is effectively separated into a resolved part and a sub-grid part. The large eddies are represented by the resolved part whilst the small scales are represented by the sub-grid part. The effect of the sub-grid part is incorporated into the resolved field through the Sub-Grid Scale (SGS) model.

Since the large scale eddies are resolved accurately, fine grids and small time-steps are required which necessitates large amounts of computational power. The Sub-Grid Scale models for LES simulations appear very similar to RANS simulations in that the smaller eddies are modelled. However, the accuracy with which the eddies that are modelled using LES simulations is far less critical due to their relatively small influence on the total flow when compared to the model eddies using a RANS model.

The method used to differentiate between the large and the small eddies, a filter is applied which derives the locally weighted averages of the flow properties. The essential property of the filtering process is the filter width, Δ, which defines the length-scale. This has the effect that any scales smaller than the filter width fall within the Sub-Grid Scale and are therefore modelled, whilst scales which are large than Δ are resolved.

There are several different filters which can be applied to LES simulations. The three most common filters include the Gaussian filter, top-hat filter, and the sharp Fourier cut-off filter (Verhoeven, 2011). Whilst each of these methods has certain advantages, only the implicit top-hat filter is used with the standard LES model within OpenFOAM, with several choices for the filter width calculations. These calculations include Prandtl delta, the cube root of cell volume delta, maximum of x, y, and z delta, and the smoothing of delta.

Once the small scales are filtered out from the large scale eddies the small scale eddies are modelled. This was first formulated by Smagorinski (1963) and developed by Kolmogorov (1991) which assumed that the small scale eddies were uniform and that the small scale eddies reduced the energy from the large scale eddies through the cascade

process. Therefore, the Smagorinsky model assumed that the small scales dissipated the energy entirely and instantaneously. However, this assumption generated an issue with excessive energy dissipation in laminar flows. This issue can be overcome with the addition of one or more equations which can vary a range of parameters such as the isotropic decay or the sub-grid eddy-viscosity based on near wall distance or cell volume.

Some of the sub-grid scale models in addition to the Smagorinsky model include:

- Van Driest damping function
    - A damping function applied to the sub-grid eddy viscosity which reduces the Smagorinsky constant as a function of wall-normal distance. However, this is generally considered not to be the preferred method as the sub-grid scale ideally should depend on the local flow properties.
- One-equation eddy viscosity models
    - There are several models which use the eddy viscosity approach in which, generally, an equation is added to the eddy-viscosity model of Smagorinsky. An equation can be applied to either the sub-grid scale kinetic energy, viscosity or vorticity. Some examples of these models include the one-equation eddy and the Spalart-Allmaras model. Whilst these models provide a significant improvement over the Smagorinsky model due to independently calculated SGS based on local flow, when the flow is not in equilibrium, there is still a deficiency in that they do not address the difference between the sub-grid scale stress and the rate of strain tensor.
- Mixed models
    - The principal for the majority of mixed models is that the small modelled eddies have an effect on the large resolved eddies and thus they do not assume the sub-grid scale eddies dissipate instantaneously as the previous models do. One such example is the scale-similarity model which essentially uses the interaction between the larger and smaller resolved eddies to extrapolate how the smallest resolved eddies interact with the model SGS eddies. The extrapolation

of the SGS eddies results in an under prediction of the energy dissipation and thus is combined with the eddy-viscosity model to produce the mixed model.

After assessing the benefits and negatives of each LES model, and the high computational requirements of LES simulations, it was decided that one model would be used for this thesis. The chosen model was the one-equation eddy model found in the OpenFOAM package. The three contributing factors to this choice was:

- One-equation eddy models provide an advantage over standard algebraic models (i.e. Smagorinsky) due to the independently calculated SGS velocity scale.
- Although mixed models have certain benefits, the one-equation model was preferred due to the increased complexity of the mixed models (de Villiers, 2006) and the possibility of a loss of accuracy in the results due to mesh sensitivity (Cabot et al., 1999).
- The one-equation model has been shown to perform well against other LES models including the modelling vortex shedding (Fureby et al., 1997; Penttinen, 2011).

The One-equation Turbulent Energy model used within the OpenFOAM package is based on the eddy-viscosity concept with the addition of the sub-grid scale (SGS) to solve the transport equation. In the One-equation Turbulent Energy model, the assumption is made that the SGS turbulent energy is isotropic and can be expressed as (Penttinen, 2011).

$$\frac{\partial}{\partial t}(k) + \frac{\partial}{\partial x_i}(U_i k) - \frac{\partial}{\partial x_i}\left(v_{SGS}\frac{\partial}{\partial x_i}(k)\right) = -BL - \frac{c_e k^{\frac{2}{3}}}{\Delta} \tag{2.10}$$

where:

$$v_{SGS} = C_k k^{\frac{1}{2}} \Delta \tag{2.11}$$

$$\epsilon = \frac{C_\epsilon k^{\frac{3}{2}}}{\Delta} \tag{2.12}$$

and k is the kinetic energy, v is the eddy-viscosity, where the –BL term corresponds to the decay of turbulence from the 'resolved scales to the SGS via the energy cascade' (de Villiers, 2006), ϵ is the turbulent dissipation, C_k=0.094 and C_ϵ=1.048. This equation can be broken down into each term. The first term is the change in turbulent SGS kinetic energy with respect to time. The second term defines the convection and the third term describes the diffusion.

Chapter 3

Predicting Surface Wakes using LES and RANS-SST Analysis

This chapter was presented at the "*2nd SIA Technology Conference*" and published in the Conference Proceedings. The citation for the research article is:

Conway, A. S. T., Ranmuthugala, D., & Binns, J. R. (2013). *Predicting surface wakes using LES and RANS-SST analysis*. Paper presented at the 2nd SIA Technology Conference, Adelaide, Australia

Chapter 4

Experimental Analysis of Surface Piercing Cylinders at High Froude Numbers

This chapter is published in the “Journal of Fluids and Thermal Science”. The citation for the research article is:

Conway, A. S. T., Cathcart, S., Binns, J. R., Ranmuthugala, D., Renilson, M. R., & Anderson, B. (2016). Experimental analysis of surface piercing cylinders at high Froude numbers. *Journal of Fluids and Thermal Science.* [vol. 4 no. 1 pp. 21-37]

Chapter 5

The End Effect of Vertical Axis Surface Piercing Cylinders with and without an End Body

This chapter has been submitted for publication in the “Journal of Fluids and Thermal Science” and at the time of writing is under review.

Abstract

When a vertical axis surface piercing cylinder, such as a submarine's periscope or snorkel, has forward motion it generates a wave plume. In the past, experiments have been conducted in a towing tank to investigate the shape of this plume (Hay, 1947). However, these experiments, and many others (Conway et al., 2016; Metcalf et al., 2006), are generally conducted with a finite cylinder length, without an end body for practical reasons. Although it is well understood that changing the end condition of a surface piercing cylinder will affect both the plume size and drag coefficient, there is very limited information in the public domain quantifying this effect.

This paper reports on an investigation into the plume structure generated by a surface piercing cylinder with different submerged end depths, with and without an end body, using both experimental and numerical analysis.

The first set of mast configurations used a surface piercing cylinder with end depths equal to 2.0 and 10.0 times the diameter of the cylinder, which replicated previous experimental data. The second set of mast configurations used a streamlined body attached to the deep end of the cylinder to investigate the effect of the end geometry on the plume structure.

It was shown for the surface piercing cylinder with no end body, that if the depth of the cylinder end below the free surface was greater than a depth to diameter ratio of 8.0, the size and shape of the wave plume is unaffected by end effect. However, at lower depth to diameter ratios the wave plume is affected by the immersion depth, and is generally smaller than for the cylinder with a deeply submerged end.

It was also shown that adding an end body reduces the depth of immersion of the end required to ensure that the shape of the plume is unaffected by the depth of immersion.

5.1 Introduction

In experimental programmes, accurately replicating a surface piercing appendage that terminates below the surface at a submerged body is extremely difficult due to the end effect at the submerged end. If the submerged end body is not included in the experimental testing (which may not be practical), the test may not replicate the desired conditions. In order to accurately model the flow conditions and the resulting plume structure, it is required to quantify the variations in plume size due to the end effect at various depths and configurations. Thus, this project investigates a range of cylinder configurations including two different immersion depths (Table 5.1) along with the addition of a streamlined end body at both lengths tested.

Whilst no published data could be found in the literature relating to vertical axis cylinders piercing the free surface with streamlined bodies attached at high diameter Froude numbers (Fr > 3), there are limited sets of published experimental data without end bodies (Conway et al., 2016; Hay, 1947; Metcalf et al., 2006; Sumner, 2010) which show that at high diameter Froude numbers, a large plume structure and bow wave is generated.

Mentor (1994) stated that the bow wave height is based on the energy generated by the stagnation pressure and thus Bernoulli's equation which is shown in Equation (5.1).

$$\frac{\eta_b}{D} = \frac{Fr^2}{2} \tag{5.1}$$

where η_b is the bow wave height, *D* is the cylinder diameter, and *Fr* is the diameter Froude number as calculated using Equation (5.2), where *U* is the forward velocity and *g* is the acceleration due to gravity.

$$Fr = \frac{U}{\sqrt{gD}} \tag{5.2}$$

Equation (5.1) can be used to determine the maximum height of the bow wave. However, this applies only to inviscid flow and thus is likely to over predict the bow wave height at high Froude numbers. Most significantly to the plume size and structure, the authors previously suggested (Conway et al., 2016) that the plume structure is generated by two separate flow phenomena. The forward region, is generated by the bow wave

separating from the cylinder, which falls downstream of the cylinder. The second region is generated by the submerged section of the cylinder.

This paper focuses on both an experimental and numerical approach where the experimental data was used to validate the numerical model, which then permitted the end effect to be studied in closer detail for the different configurations. The four configurations investigated are summarised in Table 5.1 where *T'* refers to the non-dimensional cylinder immersion depth ratio *T/D*, with *T* being the immersed depth of the cylinder and *D* the diameter of the cylinder.

Table 5.1: Summary of mast configurations investigated.

Configuration number	*T'=T/D*	End body configuration	Cylinder Diameter (mm)	Cylinder Immersion (mm)
1	2	No	100	200
2	2	Yes	100	200
3	10	No	100	1000
4	10	Yes	100	1000

In order to compare the results between different geometries, the coefficient of drag (C_D) (C_D defined in Equation (5.11)), bow wave height (η_b), plume length (λ) and plume height (η_p) are used as shown in Figure 5.1. The changes in cylinder immersion and the addition of the end body may alter the end effect on the above parameters. Slaouti et al. (1981) investigated the effect of flow around the end of a cylinder at low diameter based Reynolds numbers (60 < Re < 200). They concluded that the end of the cylinder can affect the size of the wake generated, stating that a smaller wake was generated when the free end was close to the surface, compared to a deeply submerged free end.

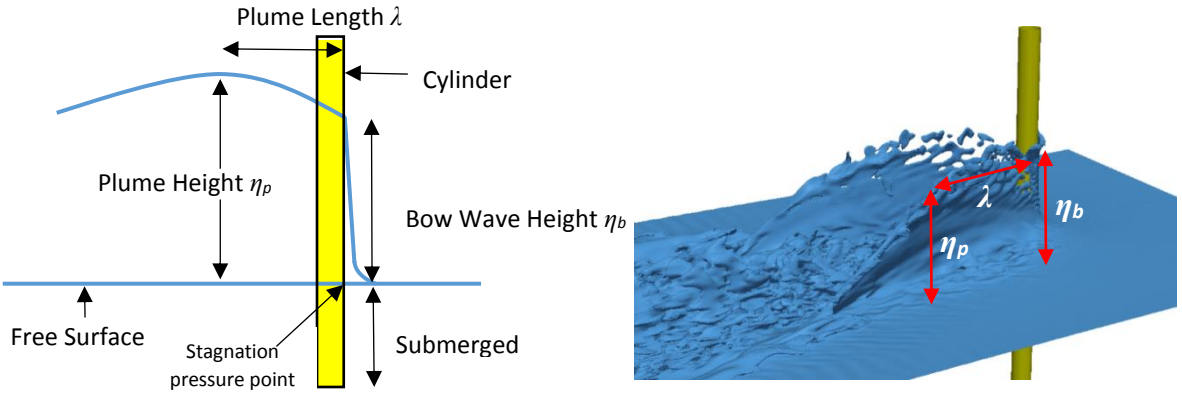

Figure 5.1: Definition of parameters used showing η_b, bow wave height, λ, plume length, and, η_p, plume height.

An application for this research is to model the plume structure generated by submarine masts. As a submarine pierces the free surface with a snorkel or periscope at high diameter Froude numbers (Fr > 3.0), a large bow wave and plume structure can be generated. This may be detectable by radar or visual sighting and can thus compromise the stealth of the submarine. Therefore, understanding and modelling of this plume structure is essential to maintain stealth during such operations.

The typical forward velocity and mast diameter of a submarine at snorkelling speeds correspond to a diameter Froude number to a maximum of around four. Previously published experimental data for surface piercing cylinders is very limited at high Froude numbers with most results limited to a Froude number up to 1.65. Hay (1947) created a large set of experimental data measuring the parameters shown in Figure 1 for cylinders of different submerged depth and diameter at a range of speeds corresponding to diameter Froude numbers between 1.6 and 4.9. Mentor (1994) performed a similar set of experiments, with the addition of pressure measurements below and above the still water surface level. However, these were limited to a Froude number of less than 1.65. Metcalf et al. (2006) performed a set of experiments measuring pressure using a NACA0024 cross section rather than a circular cylinder across a range of cord width based Froude numbers between 0.19 and 0.55.

Similarly for numerical data, there is very limited data published with reference to the wake and plume generated by a bluff body at high Froude numbers. Two examples of numerical investigations at low Froude numbers are found in the research conducted by Kawamura et al. (2002) and Yu et al. (2008). Whilst Kawamura et al. only modelled the wake generated by a cylinder at Froude numbers of 0.2, 0.5 and 0.8, Yu et al. modelled the wake up to a Froude number of 3. However, Yu et al. investigated primarily the wake and bow wave height without mentioning the plume structure. They found poor correlation to the experimental data published by Hay (1947) at Froude numbers greater than 2.

The authors have previously published data (Conway et al., 2016; Conway et al., 2017a) which details the studies conducted both numerically and experimentally to characterise the plume structure generated by surface piercing bluff bodies. The present study extends this work by modifying the experimental test rig to accurately record drag data and quantifying the end-effect both numerically and experimentally.

In addition, there is little available data regarding the oscillations which are present with bluff bodies piercing the free surface under the conditions discussed. These oscillations are understood to be caused by the Bernard-von Karman instability (Hernandez et al., 2000). The present study includes a brief investigation into the frequency of the bow wave oscillations and changes in frequency over the Froude number range.

5.2 Experimental approach

The experiments conducted for this work was carried out in the towing tank located in the Australian Maritime College (AMC). The tank has a length of 100 m, width of 3.55 m, and a depth of 1.5 m, with a carriage capable of towing models at speeds up to 4.6 m/s. This allowed 0.6 m clearance between the end of the cylinder and the bottom of the tank.

In order to ensure the carriage and set-up was capable of carrying out the experiments at the required speeds, six issues were considered. These were: plume size clearance, total drag, vortex shedding, load cells, plume size recording, and end body dimensions. These are discussed below.

5.2.1 Plume clearance

The bow wave height at different Froude numbers published previously by Hay (1947) and the authors (Conway et al., 2016) are presented in Figure 5.2. The upper limit line is based on Bernoulli's equation (Equation 5.1) as given by Mentor (1994). The maximum predicted bow wave height and plume height at Fr = 4 was measured to be 550 mm and 700 mm respectively. Therefore, these values were used to determine the location of the cylinder on the tow tank carriage in order to remove interference of the carriage on the plume.

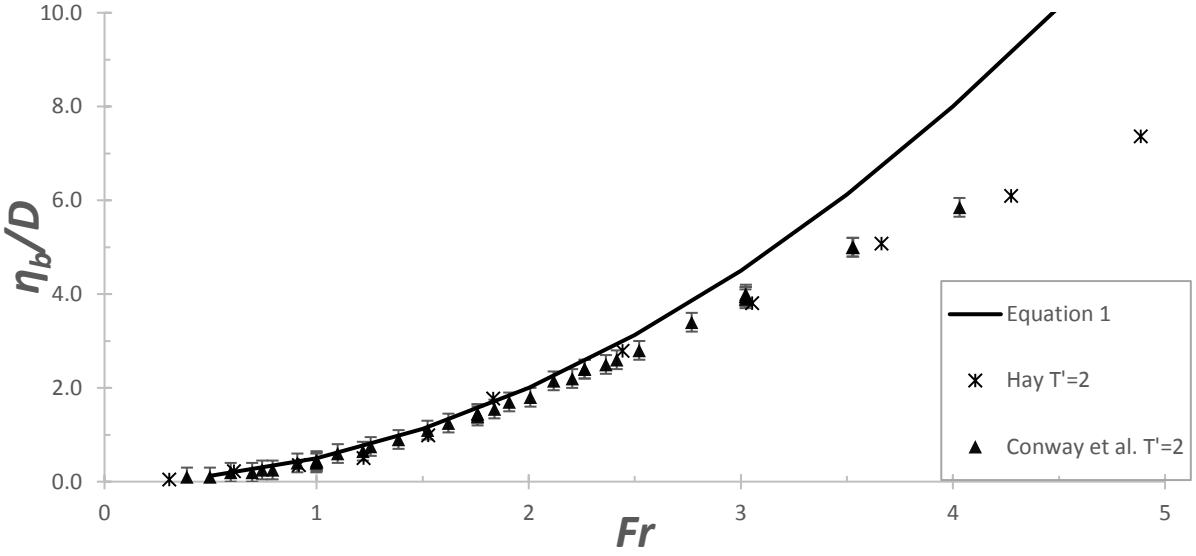

Figure 5.2: Comparison of non-dimensional bow wave height η_b/D from Hay (1947) and Conway et al. (2016) and the theoretical upper limit based on stagnation pressure.

5.2.2 Drag

An important consideration for the rig set-up was that it must withstand the significant loads which are generated in the highest load configuration, which was considered to be the long cylinder with the attached end body (condition 4). A preliminary Computational Fluid Dynamics (CFD) analysis was conducted to determine the approximate loads, followed by a Finite Element Analysis (FEA) to ensure that the rig would not fail and/or the cylinder would not undergo significant deflection. The study concluded that the

cylinder with a wall thickness of 4 mm would withstand the hydrodynamic forces with a maximum deflection of approximately 2 mm over the 1.97 m between the lower bearing and the end of the cylinder.

5.2.3 Load Cells

Due to the transient hydrodynamic forces and the arrangement of the towing tank and its carriage, it was essential that the cylinder mounting and load cell arrangement was designed to accurately measure the drag generated by the cylinder and the end body. Figure 5.3 shows a schematic of the mounting arrangement with the appropriate load cell position relative to the water surface. Figure 5.4 shows the overall and detailed set-up of the load cells used for the experiments. In order to remove vertical forces on both load cells, a horizontal low friction bearing track and pillow block arrangement was used, which is shown in the bottom right photo in Figure 5.4. The horizontal track allowed the total mass plus any change in vertical loading to be transferred through the rig, whilst allowing all reaction forces on the bottom load cell (tension) to be recorded. The bottom load cell was a XTRAN S1W rated to 2 kN. The pillow block bearing provided a pivot location around the bottom load cell connection point to prevent the generation of a load moment. The top load cell was a simple compression point using an AMTI MC3A 250 load cell rated to 1112 N. The load cell was configured with a two face contact to record the resultant force at the top of the cylinder.

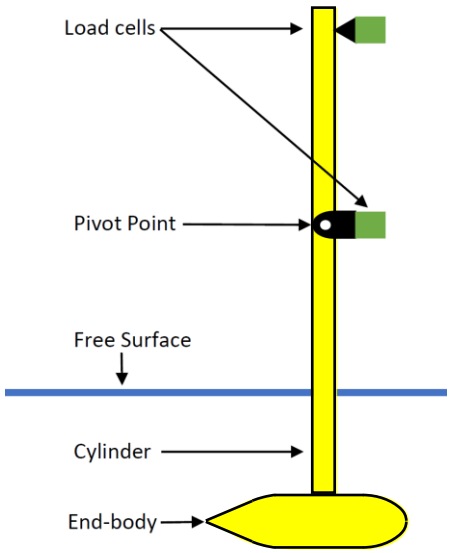

Figure 5.3: Schematic representation of experimental set-up to demonstrate approximate configuration of load cells (not to scale).

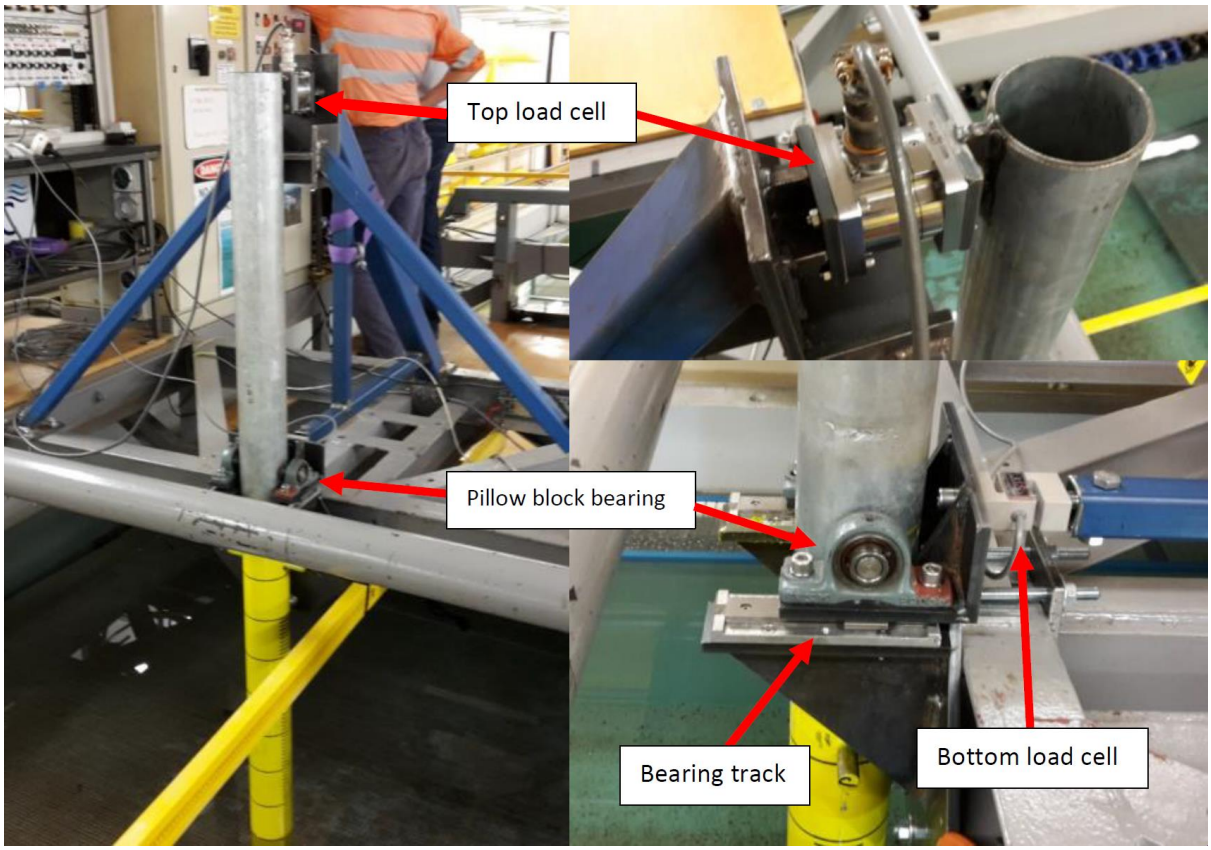

Figure 5.4: Overall experimental set-up (left) and detailed views of the top load cell arrangement (top right) and the bottom load cell, bearing track, and pillow block bearing configuration (bottom right).

5.2.4 Plume size measurements

In order to accurately measure the plume size, bow wave height, and bow wave height oscillations; a combination of still photography, videography, draft marks, and tape measures were used as shown in Figure 5.5. The still photography camera, a Digital Single-Lens Reflex (DSLR) camera, was positioned on the starboard side with the intention of capturing the bow wave height, plume height, and plume length. The video camera, a GoPro camera set to capture at 50 frames/second, was also mounted on the starboard side facing port, tasked to capture the oscillations in the bow wave and plume size. In order to calculate the required dimensions from the cameras, the cylinder was clearly marked with major draft markings on the starboard side in clear view of both cameras to measure the bow wave height, η_b, and plume height, η_p. Additionally, a 3 m tape measure attached to a rigid beam was suspended horizontally lengthwise on the carriage to allow measurement of the plume length, λ.

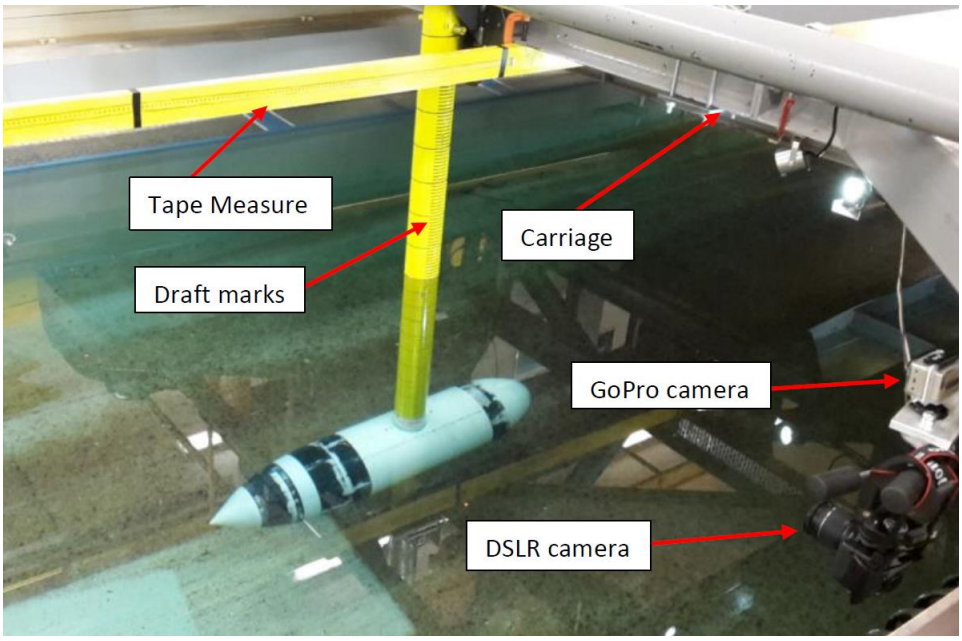

Figure 5.5: Experimental rig set-up showing the tape measure, draft marks, DSLR camera, and GoPro camera.

5.2.5 End body

As a critical part of the experimental design, the end body was designed to reduce the effect of a free end without increasing the potential load on the rig beyond failure. It was estimated that a 250 mm diameter body of revolution was the largest body that could be accommodated with the restrictions imposed by the carriage and towing tank cross section. The end body used was a streamlined body with a total length of 1.2 m, which included a cylindrical mid-section 0.62 m long. Figure 5.6 shows the length and shape of the end body, with Figure 5.5 showing the body attached to the cylinder in the towing tank. The forward and aft sections of the end body were produced using 3-D printing to accurately generate the required profile, while a 250 mm diameter PVC piping was used for the cylindrical parallel mid-body section. In order to reduce vertical loading on the load cells and the experimental rig, the end body was flooded during testing.

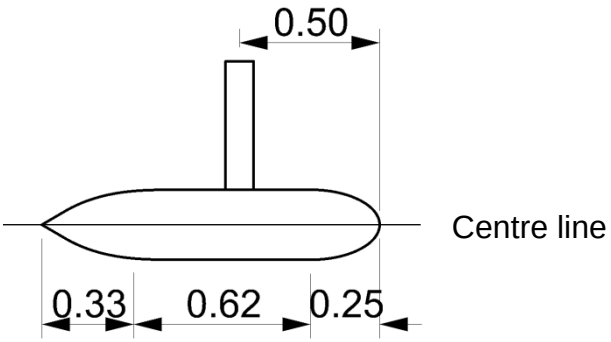

Figure 5.6: Shape and dimensions of the end body used, including the location of cylinder joint.

5.3 Numerical approach

5.3.1 OpenFOAM and governing equations

The authors have previously (Conway et al., 2013) established that the Reynolds Average Navier-Stokes (RANS) models due to inherent turbulence averaging are not capable of modelling the plume structure of a moving surface piecing cylinder. In contrast it was shown that Large Eddy Simulation (LES) models were able to accurately model the plume structure. Therefore, all numerical simulations performed in this study utilised LES models using the open source CFD software OpenFOAM, which includes an inbuilt meshing software. The LES simulations employed in this study utilised the One-Equation Eddy model, which uses the Navier-Stokes equations with the Sub-Grid Scale (SGS) model in order to model the smaller eddies whilst solving the larger eddies (Foundation, 2013; Piomelli et al., 2001). The governing equations used in the simulation models can be expressed for incompressible flow as follows,

$$\rho\left(\frac{dU}{dt} + U \cdot \nabla U\right) = -\nabla p + \mu \nabla^2 U \tag{5.3}$$

$$\nabla \cdot U = 0 \tag{5.4}$$

where, ρ is the fluid density, U is the flow velocity, p is the fluid pressure, μ is the fluid viscosity, t is time, and ∇ is the divergence.

The One-equation Turbulent Energy model was used within OpenFOAM, with the assumption is made that the SGS turbulent energy is isotropic and can be expressed as (Penttinen, 2011);

$$\frac{\partial}{\partial t}(k) + \frac{\partial}{\partial x_i}(U_i k) - \frac{\partial}{\partial x_i}\left(v_{SGS}\frac{\partial}{\partial x_i}(k)\right) = -BL - \frac{c_e k^{\frac{2}{3}}}{\Delta} \tag{5.5}$$

where:

$$v_{SGS} = C_k k^{\frac{1}{2}} \Delta \tag{5.6}$$

and k is the kinetic energy, v is the eddy-viscosity, BL corresponds to the decay of the turbulence, ϵ is the turbulent dissipation, C_k=0.094 and C_ϵ=1.048. Equation (5.6) can be broken down into each term. The first term is the change in turbulent SGS kinetic energy with respect to time. The second term defines the convection and the third term describes the diffusion.

5.3.2 Simulation parameters

As the numerical simulations were conducted to model the experimental set-up, the flow around the mast was considered to be incompressible, turbulent, and two phase (i.e. water and air). The cylinder diameter, cylinder depth, and end body dimensions of the numerical model matched the dimensions of the tow tank experimental setup, while the computational domain (except for its length) replicated the dimensions of the tow tank. The numerical domain and grid remained as similar as possible for the four different configurations given in Table 5.1, whilst being optimised for a Froude number of 4.0 in order to capture the entire plume structure at the largest possible plume size. The difference between each grid was the length of the cylinder along with thickness of the boundary layer in order to maintain the same y^+ value at all tested speeds.

The numerical grid was generated using the OpenFOAM inbuilt meshing software, SnappyHexMesh, which is capable of using hanging nodes and inflation layers. Hanging nodes allows the user to increase the density of cells in specified areas whilst the inflation layer allows the flow within the boundary layer of the cylinder and end body to be solved. The mesh used for the T'=2.0 with the end body simulations is shown in Figure 5.7 showing the cylinder, end body, inflation layer and mesh refinement areas.

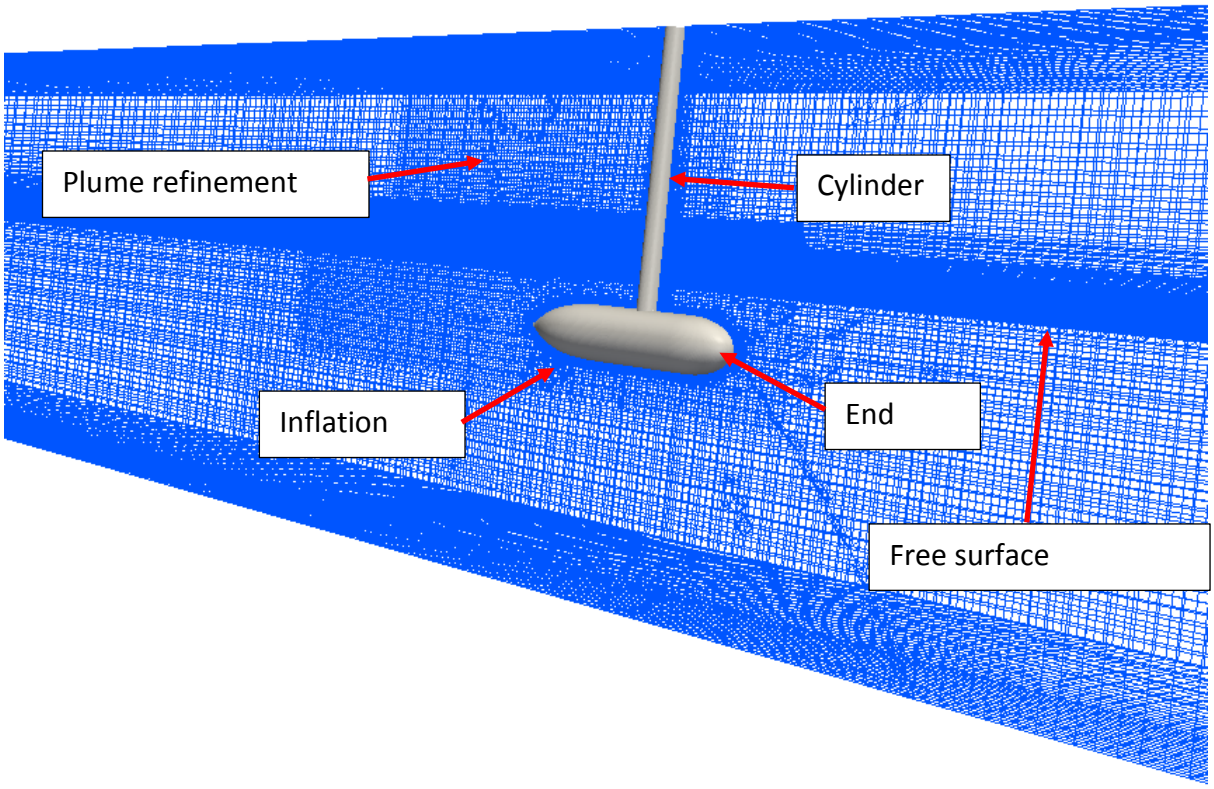

Figure 5.7: Mesh used for numerical simulations showing end body, cylinder refinement areas, and inflation layer for a cylinder immersion depth to diameter ratio of T'=2.

The bottom and side domain dimensions were selected to represent the tow tank used for the experiments and the top of the domain was selected to be able to fully capture the plume profile. In order to reduce the computational effort required, the grid size was minimised with the use of hanging nodes in the areas of interest around the plume structure and along the free surface (Figure 5.7). The refinement level was specified by the number of cells. A single cell was split by, i.e. 2^n, where n is the refinement level. The refinement areas were concentrated to an area 120% larger than the expected plume size with a combination of refinement levels up to four. This method allowed for a fine grid in the required areas around the plume, free surface and cylinder/end body, whilst rapidly decreasing to a course grid outside these areas. For example, the refinement area sizing within the plume region resulted in cells which were approximately 3 x 1.5 x 1.5 mm (xyz axis) in size, whilst in the region just outside the plume, the cells were approximately 90 x 30

x 30 mm. This allowed the computational requirements to be reduced whilst numerically dampening out the turbulent flow as it approached the domain exits and the boundaries, thus increasing the stability of the simulations.

5.3.3 OpenFOAM simulation setup

As OpenFOAM is an open source software, the user has significant control over the simulation through changing settings within the software. This study used OpenFOAM v2.2.1, with several settings selected to suit the required simulations including the linear system solvers, interpolation schemes, and solver settings which are discussed below.

The flow around bluff bodies, such as cylinders, generates several flow instabilities which tend to cause numerical simulations to become unstable and fail. Therefore, the interpolation schemes and solvers selected were based on two main criteria. Firstly, schemes and solvers were chosen in order to increase numerical stability without significantly affecting the accuracy of the results. The second criterion was to reduce the computational requirements.

To solve for the pressure, the Preconditioned Conjugate Gradient (PCG) linear system solver with Geometric-Algebraic Multi-Grid (GAMG) as a pre-conditioner was utilised. This was selected as the pressure was found to be sensitive to the instabilities caused by the flow around the end of the cylinder, whilst the PCG solver increased the stability of the simulation. The GAMG pre-conditioner offers the advantage of generating a quick solution using a course mesh to generate an initial condition for each time step, which reduces the computational effort and increases the stability of the simulation (OpenFOAM-Foundation, 2013). The solver and pre-conditioner used for the velocity field was the default settings used within OpenFOAM given below, as the velocity field appeared to have little effect on the simulations from changes in the velocity solvers. The solver used was the Preconditioned BiConjugate Gradient (PBiCG) solver with the Diagonal Incomplete LU (DILU) as the pre-conditioner. In addition to the solvers, the PIMPLE algorithm was used to couple the equations for momentum and mass conservation. The PIMPLE algorithm is specific for

OpenFOAM and is a combination of the more standard Pressure-Implicit Split Operator (PISO) and Semi-Implicit for Pre-conditioner Equations (SIMPLE) algorithms.

The second criterion was to reduce computational requirements and as such, the OpenFOAM *kqrWallFunction* was applied to the *k* field. The addition of this wall function allows the boundary layer sub-layer grid height to be increased from a y^+ value of one up to approximately 30 (OpenFOAM-Foundation, 2013).

5.3.4 Numerical verification

A grid independence study was conducted to determine if the settings selected were applicable for generating a plume structure. As *T'*=2.0 at *Fr*=4.0 was the most extreme case in this study due to the large plume structure and end effect, the corresponding speed and depth was employed for the grid independence study.

The first stage of the grid independence study involved investigating the effect of the inflation layers within the boundary layers. The boundary inflation layer was analysed by comparing the y^+ value against the bow wave height. The y^+ value is calculated using equation (5.7) as,

$$y^+ = \frac{yu_\tau}{\nu} \tag{5.7}$$

where *y* is the distance to the wall, u_τ is the friction velocity, and *v* is the kinematic viscosity. Figure 5.8 shows the y^+ study results in which the bow wave height is plotted for the y^+ range varying from 160 to 30, (i.e. as the distance from the surface to the first layer is reduced). As seen, the bow wave height begins to plateau at a y^+ value of approximately 45. Therefore, all the simulations were conducted with an inflation layer such that the y^+ value remained approximately around 35.

Furthermore, a grid independence study was conducted to investigate the mesh sensitivity to grid density. This was done by progressively increasing the mesh density, especially around the areas of concern, such as the free surface and plume region, until changes to the plume length and height were relatively insignificant. Figure 5.9 shows the percentage difference in plume length and height in comparison to those obtained for a 14

million cell mesh. It is clearly seen that the mesh achieves grid independence around a mesh density of 8-10 million elements, and hence, a mesh of 10 million elements was used for the numerical simulations.

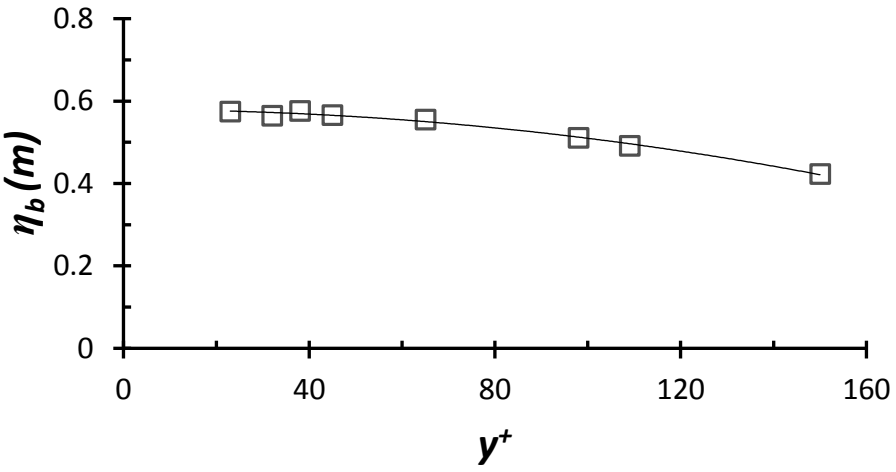

Figure 5.8: Grid independence study based on y^+ and bow wave height (η_b) at Fr=4.0 and T'=2.0 without an end body.

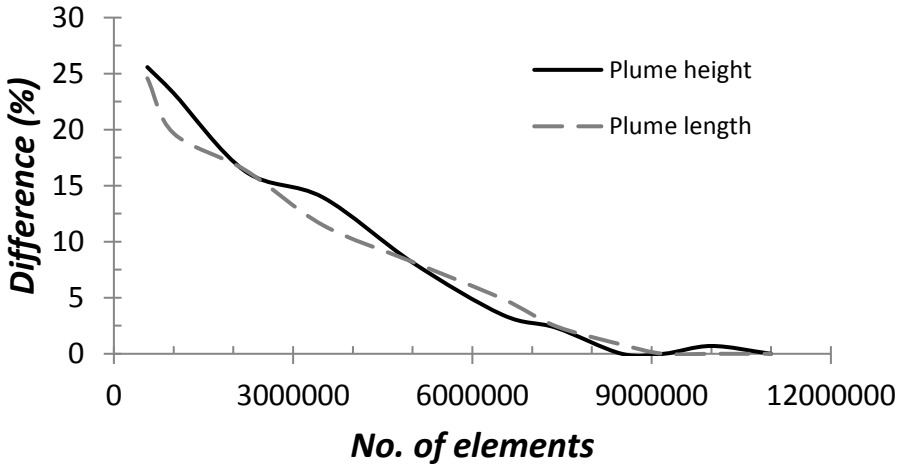

Figure 5.9: Mesh density study using plume height and plume length at Fr=4.0 and T'=2.0 without an end body compared to % difference to a 14 million element mesh.

5.4 Results and discussion

Firstly, the numerical simulation was validated using the experimental results for both the drag and plume dimensions for all conditions, with results from two of the four conditions presented below. The validated numerical code allowed the numerical simulations to be used to investigate the influence of the cylinder immersion depth (*T'*) and end conditions on the plume size and drag coefficient as a function of Froude number.

The data gathered related to the plume size obtained through both the numerical and experimental approaches are also presented in this section. The results have been non-dimenionalised with respect to the Froude number where the non-dimensional bow wave height, η_b', plume height, η_p', and plume length, λ', are defined in Equations (5.8), (5.9), and (5.10) respectively.

$$\eta_b' = \frac{\eta_b}{DFr^2} \tag{5.8}$$

$$\eta_p' = \frac{\eta_p}{DFr^2} \tag{5.9}$$

$$\lambda' = \frac{\lambda}{DFr^2} \tag{5.10}$$

The drag coefficient (C_D) of the cylinder is presented as a function of Froude number based on submerged frontal area of the cylinder only as,

$$C_D = \frac{F}{2\rho U^2 A} \tag{5.11}$$

where, *F* is the drag force on the cylinder, *ρ* is the water density, *U* is the forward velocity of the cylinder, and *A* is the total frontal submerged area of the cylinder. For the numerical cases, the drag encountered by the cylinder was calculated separately from the end body (when the end body was attached) and thus the C_D was calculated only for the cylinder. The C_D was also obtained for the experimental cases when the end body was not attached. However, with the experimental set-up, it was not possible to separate the cylinder drag force and the end body drag force, as they were recorded as a total value, and thus, no C_D is

presented for experimental results with the end body attached (i.e. for configurations two and four in Table 5.1)

5.4.1 Numerical validation

The numerical simulations were compared to the equivalent experimental data with the numerical domain representing the experimental rig and testing conditions. The comparison of the numerical and experimental results for the *T'*=2.0 immersion with and without end body is given in Figure 5.10 to Figure 5.13. At Froude numbers lower than Fr=3.0, the plume size was not fully developed and thus no measurements were taken for the plume length or plume height. Therefore, the data in Figure 5.11 and Figure 5.12 are only for Froude numbers above 3.0.

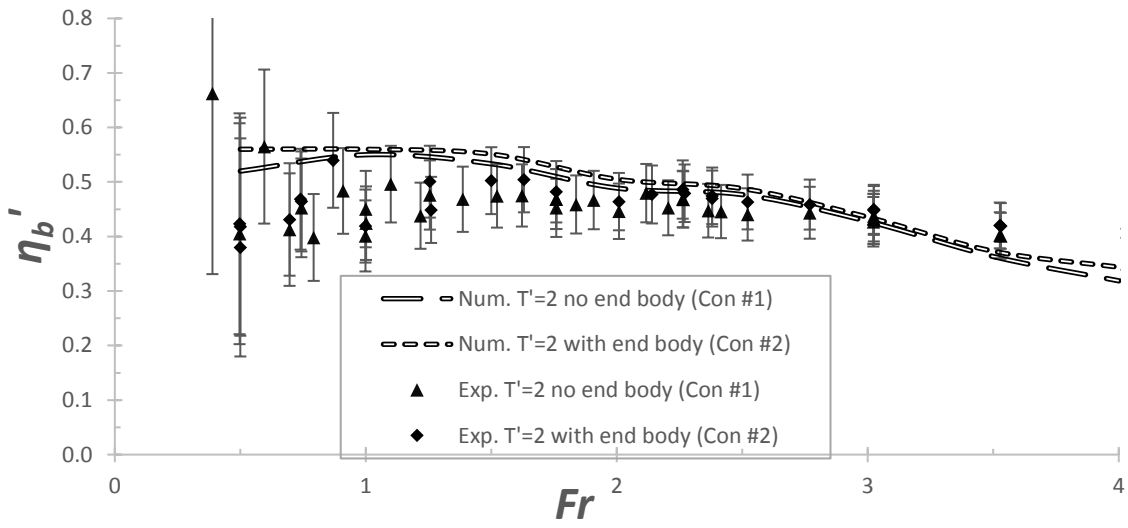

Figure 5.10: Comparison of non-dimensional bow wave height, η_b', as functions of Froude number, *Fr*, using experimental and numerical results for *T'=2.0* immersion, with and without an end body.

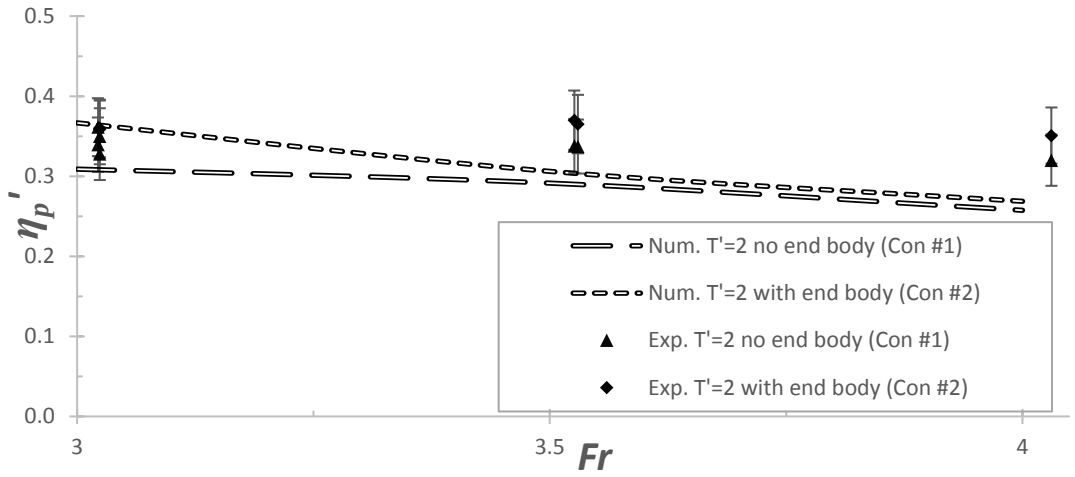

Figure 5.11: Comparison of non-dimensional plume height, η_p', variation with respect to Froude number, *Fr*, using experimental and numerical results for *T'*=2.0 immersion, with and without an end body.

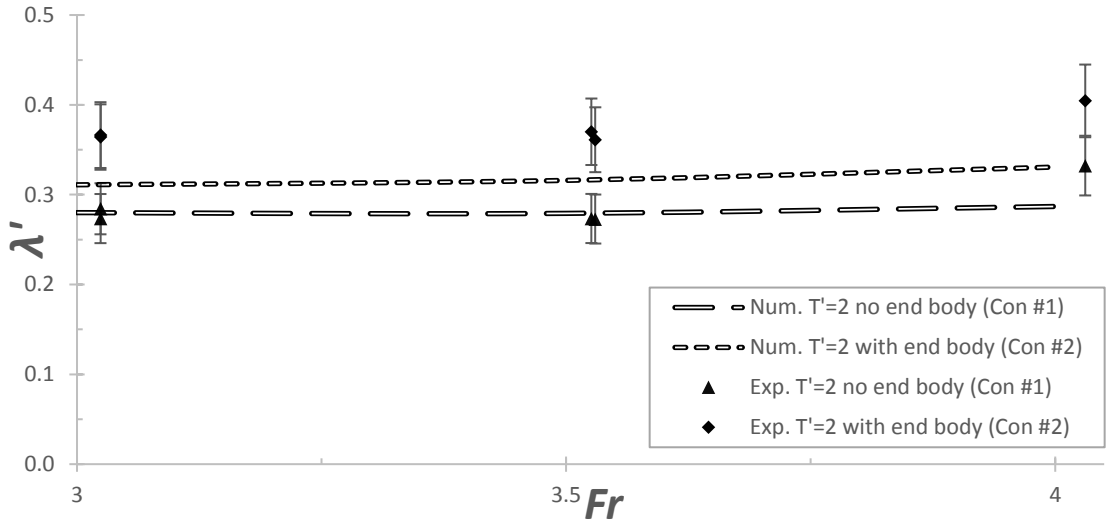

Figure 5.12: Comparison of non-dimensional plume length, λ', variation with respect to Froude number, *Fr*, using experimental and numerical results for *T'*=2.0 immersion, with and without an end body.

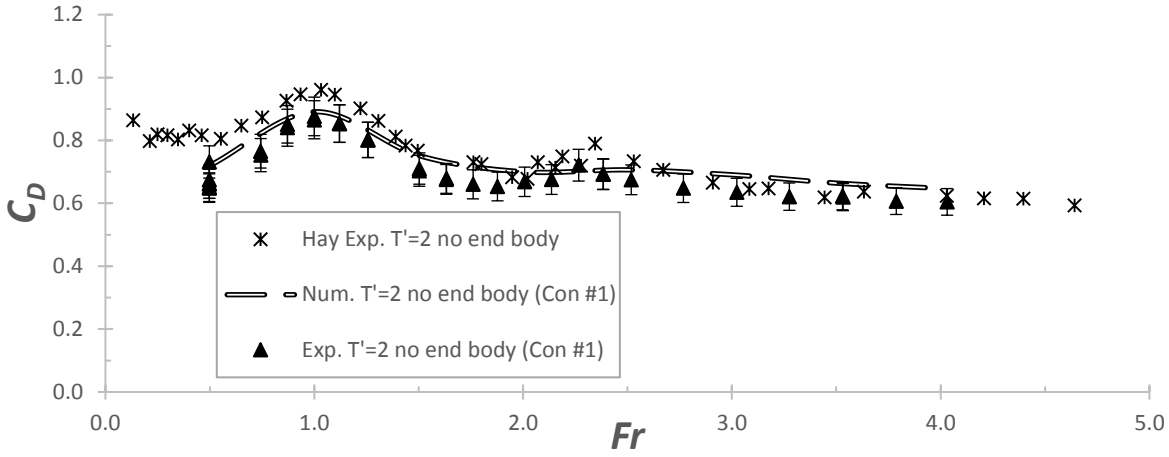

Figure 5.13: Comparison of drag coefficient, C_d, variation with respect to Froude number, *Fr*, using experimental and numerical results for the 200 mm depth, without an end body.

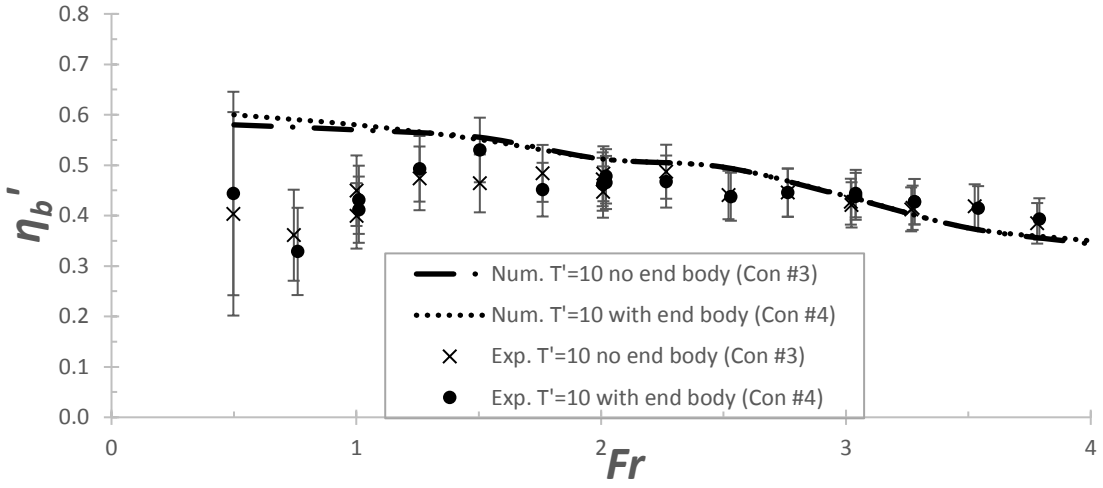

Figure 5.14: Comparison of non-dimensional bow wave height, η_b', as functions of Froude number, *Fr*, using experimental and numerical results for *T'*=10.0 immersion, with and without an end body.

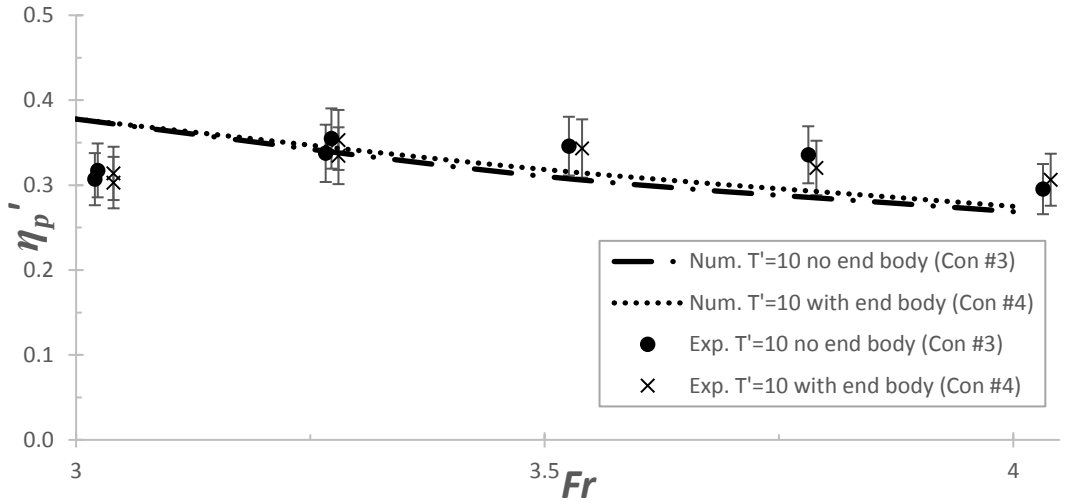

Figure 5.15: Comparison of non-dimensional plume height, η_p', variation with respect to Froude number, *Fr*, using experimental and numerical results for *T'*=10.0 immersion, with and without an end body.

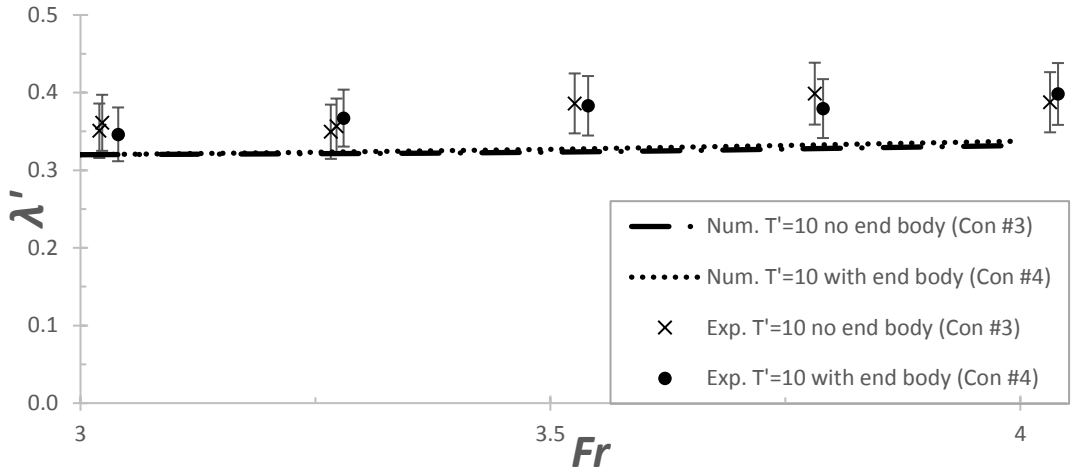

Figure 5.16: Comparison of non-dimensional plume length, λ', variation with respect to Froude number, *Fr*, using experimental and numerical results for *T'*=10.0 immersion, with and without an end body.

Figure 5.10 shows the bow wave height generated by each set-up as a function of the Froude number. At the lower Froude numbers (Fr<1.0) for both cases, there is considerable scatter in the measured non-dimensional bow wave height due to the small bow waves generated. The difficulty in accurately measuring the bow wave height can be seen by the large uncertainty bars which appears exaggerated due to the non-dimensional representation. At higher Froude numbers (Fr>1.5) the numerical predictions agree reasonably well with the measurements. Although there is an under prediction of the bow

wave height, the numerical predictions capture the reduction in non-dimensional bow wave height as a function of Froude number for both configurations tested, i.e. the cylinder with and without an end body. This indicates that whilst the numerical simulation tends to underestimate the bow wave height at Froude numbers greater than 3.0, it is capable of capturing the changes in the bow wave height as a result of different cylinder end configurations.

The plume length, as shown in Figure 5.12, shows a strong correlation between the experimental and numerical data for both mast configurations with a small yet consistent under predication when compared to experimental data. The plume height, Figure 5.11, shows a similar correlation between the numerical predictions and the experimental measurements as was observed for the bow wave height (Figure 5.10). That is, whilst the numerical simulation under predicts the plume length (Figure 5.11) when compared to the experimental measurements, the constant plume height difference between both mast configurations can be seen in both sets of data.

In addition to the plume size and bow wave height, the drag coefficient was used to validate the numerical simulations as presented in Figure 5.13. As mentioned earlier, the drag coefficient could only be recorded for the cylinder without the end body condition experimentally. As can be seen the numerical predictions agree well with both Hay's (1947) and the present experimental measurements.

Similarly, the validation for the T'=10.0 immersion condition is given in Figure 5.14 to Figure 5.16. Whilst the bow wave height (Figure 5.14) under predicts at higher Froude values, which could be a results of either stagnation pressure under prediction or over dissipation of the energy in the turbulent flow, there is a strong correlation between the experimental and numerical results at each Froude number, i.e. the change in end effect is being accurately modelled using LES. The difference in bow wave height, with and without an end body, is minimal for both experimental and numerical results. The plume height (Figure 5.15) shows little variation between the two end configurations. The predicted plume length (Figure 5.16) is slightly under predicted when compared to the experimental data, however, it accurately models the consistent plume length between the two end configurations.

5.4.2 End effect

The effect of the immersed end of a surface piercing cylinder on the plume developed as it moved forward was investigated using the validated numerical simulation model. The results for the four configurations described in Table 5.1 are presented in Figure 5.17 to Figure 5.20.

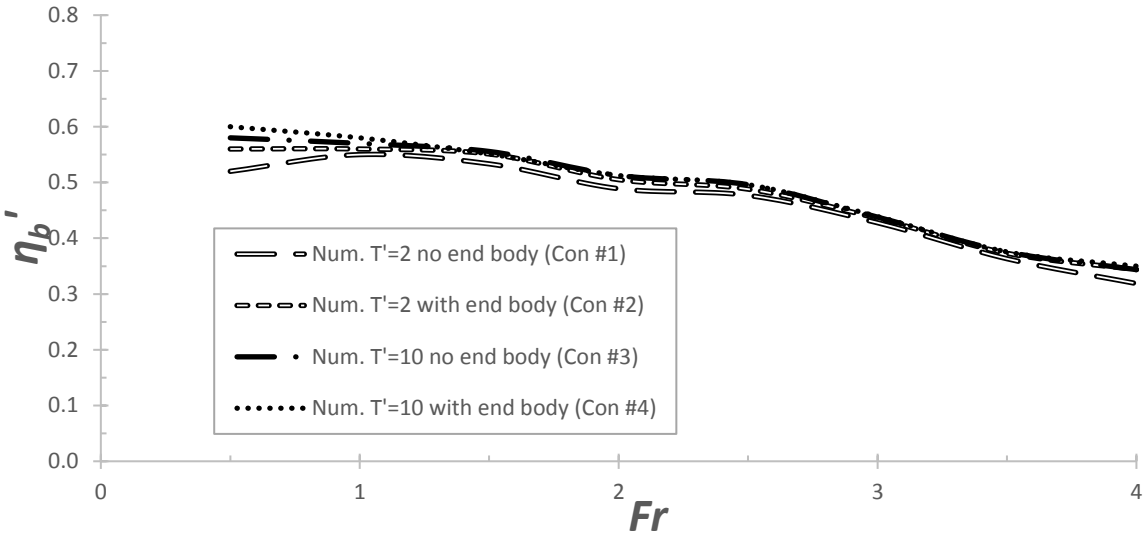

Figure 5.17: Numerical simulation of non-dimensional bow wave height, η_b', as a function of Froude number, *Fr*, with different end configurations.

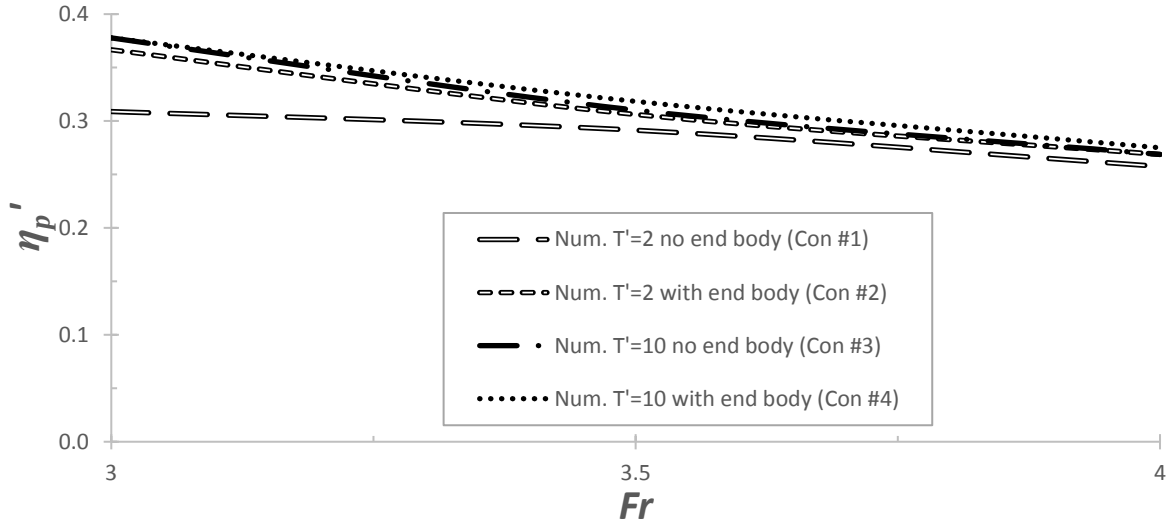

Figure 5.18: Numerical simulation of non-dimensional plume height, η_p', as a function of Froude number, *Fr*, with different end configurations.

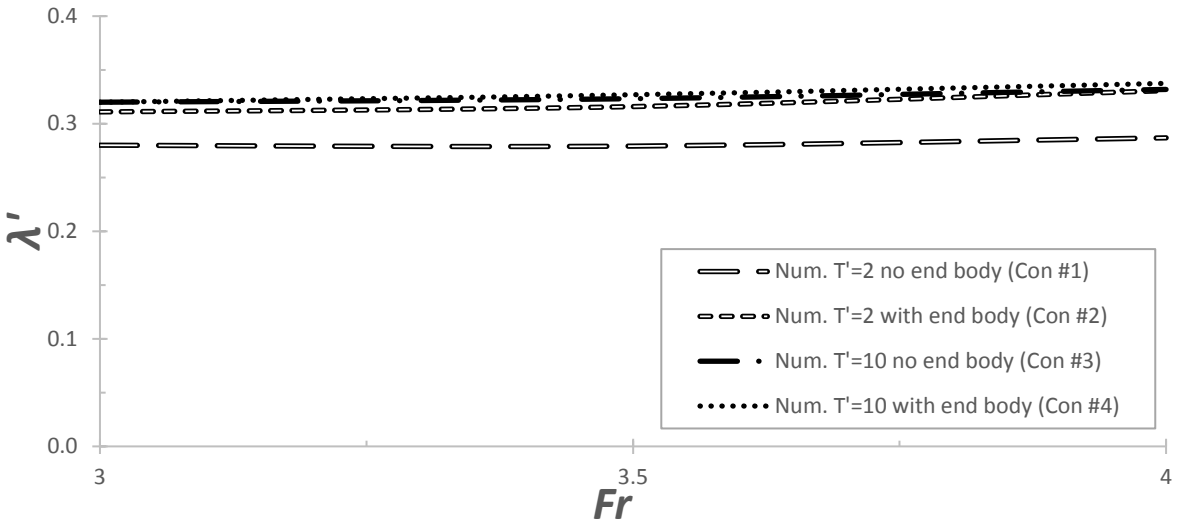

Figure 5.19: Numerical simulation of non-dimensional plume length, λ', as a function of Froude number, *Fr*, with different end configurations.

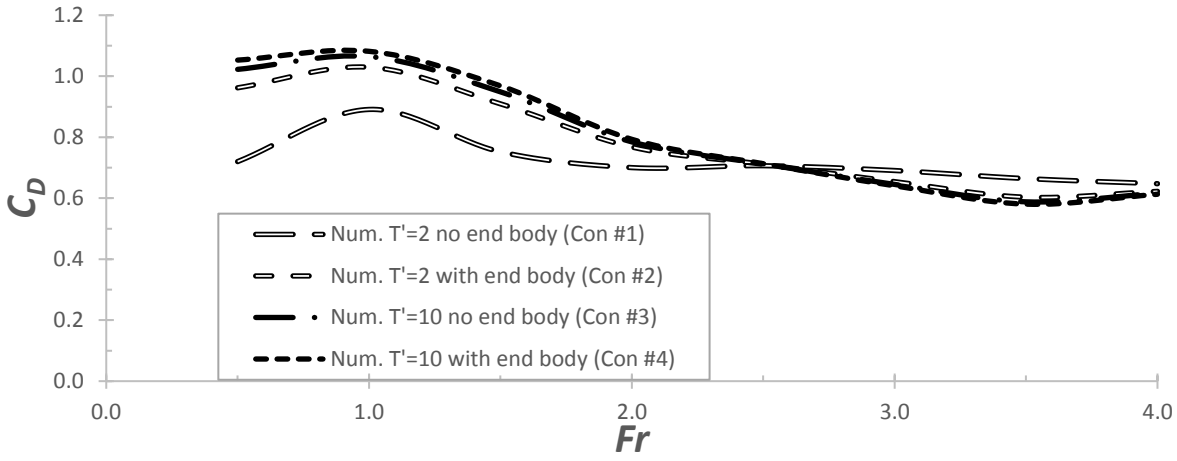

Figure 5.20: Numerical simulation of drag coefficient, C_D, as a function of Froude number, *Fr*, with different end configurations.

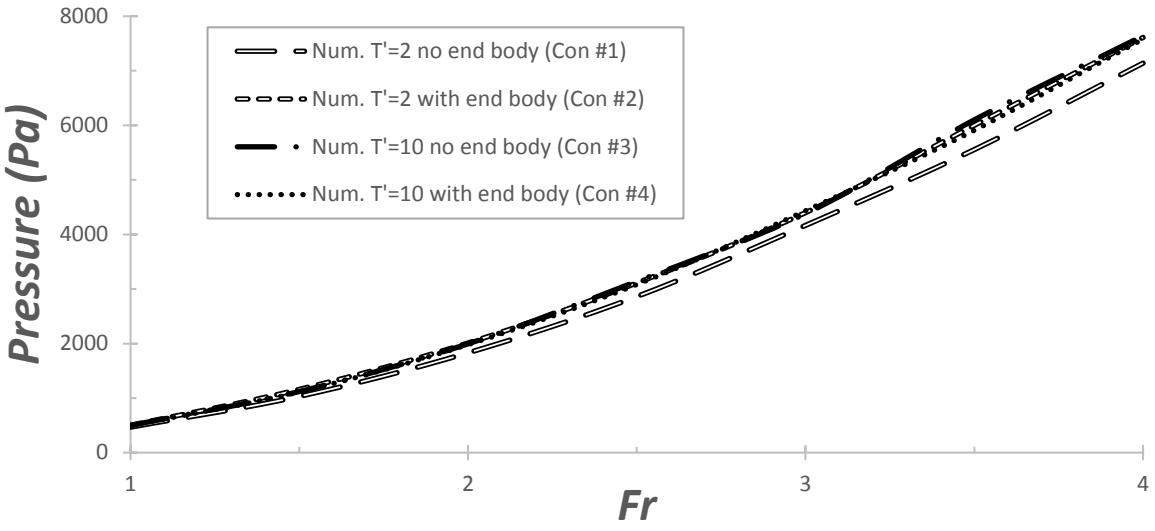

Figure 5.21: Numerical simulation of stagnation pressure on cylinder at surface level (see Figure 5.1) as a function of Froude number, Fr, with different end configurations.

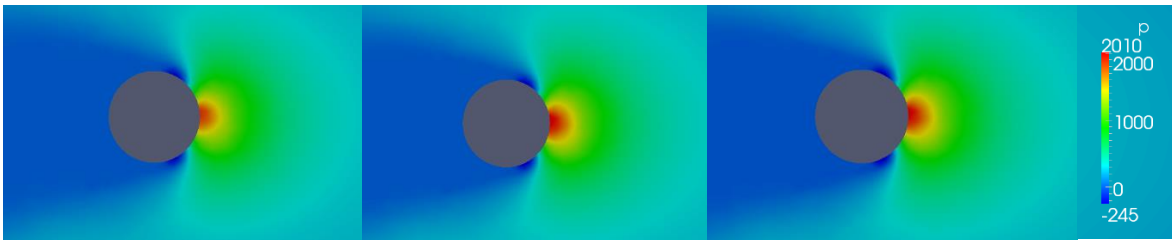

Figure 5.22: Difference in stagnation pressure at Fr=2 for T'=2 without end body (left), T'=2 with endbody (middle), and T'=10.0 without end body which is a contributing factor to change in bow wave height and plume size.

It is seen from Figure 5.17 that the bow wave height for the *T'*=2.0 immersion with no end body is smaller than that for both the *T'*=10.0 (with and without the end body) and *T'*=2.0 with an end body. The most distinct difference between the *T'*=2.0 without an end body being approximately 6% below the three other configurations. As mentioned in the Introduction, the bow wave height is influenced by the stagnation pressure at the front of the cylinder and thus changes in the stagnation pressure will result in changes in the bow wave height and hence plume dimensions. The results indicate that by the addition of an end body and/or increasing the submerged depth, the pressure lost around the bottom end of the cylinder is significantly reduced, which in turn increases the plume dimensions and hence represents the conditions of an infinitely long cylinder. The change in stagnation pressure can also be seen in Figure 5.21 and Figure 5.22, which show the stagnation

pressure at surface (see Figure 5.1). The percentage decrease in the stagnation pressure between T'=2 without an endbody (configuration 1) and T'=2 with an endbody and T'=10 with and without an endbody (configurations 2, 3, and 4) corresponds to the change in bow wave height discussed in Figure 5.17.

The plume height (Figure 5.18) showed little variation between the four different configurations. The main difference in plume height was found for T'=2.0 without an end body at Fr=3.0, which resulted in a slightly lower plume height in comparison to the other three configurations. The difference in plume height was much less than that recorded for the bow wave height and minimal over the Froude number range 3.5 to 4.0. This suggests that the end condition of the cylinder has a much smaller impact on the plume height when compared to bow wave height.

Figure 5.19 shows that the plume length for the cases T'=2.0 with an end body and T'=10.0 with and without the end body are extremely similar. Additionally, the results show approximately an 8% decrease in plume length for T'=2.0 with no end body. This, in combination with the bow wave height, indicates that there is a significant difference in plume size generated by a cylinder operating with an 'open end' close to the free surface when compared to a cylinder with either sufficient immersion depth or with an end body. An explanation for this difference can be seen in Figure 5.22 with an increase in stagnation pressure from T'=2.0 without an end body to T'=2.0 with an end body and T'=10.0 without an end body. This increase in stagnation pressure can directly increase the bow wave height and plume size.

The results for the drag coefficient as a function of Froude number are given in Figure 5.20. The drag coefficient was obtained using Equation (5.11). For the cases involving an end body, the drag forces were separated and only the drag on the cylinder was used for the drag coefficient. As can be seen, the drag coefficient for the T'=2.0 immersion with no end body shows a distinct difference to the results from the other three configurations. As discussed previously by the authors in Conway et al. (2017a), the C_D curve profile for the T'=10.0 immersion depth cylinder better matches the published drag profile of a cylinder (Sumer et al., 1997). This indicates that the drag created by the immersed free end of the cylinder for T'=10 does not significantly alter the drag characteristics of the cylinder.

In order to determine the minimum value of *T'* to avoid the cylinder end effects, several cylinder immersion lengths were investigated using the same numerical model at a Froude number of 4.0 ranging between *T'*=2.0 up to *T'*=10.0. The results for each of the measured plume dimensions as a function of *T'* are presented in Figure 5.23. Similar to the results discussed above, the bow wave height and the plume length vary with the immersion depth to diameter ratio (*T'*). A plateau at approximately *T'*=8.0 suggests that any further increases in the cylinder immersion depth would not have an effect on the plume dimensions.

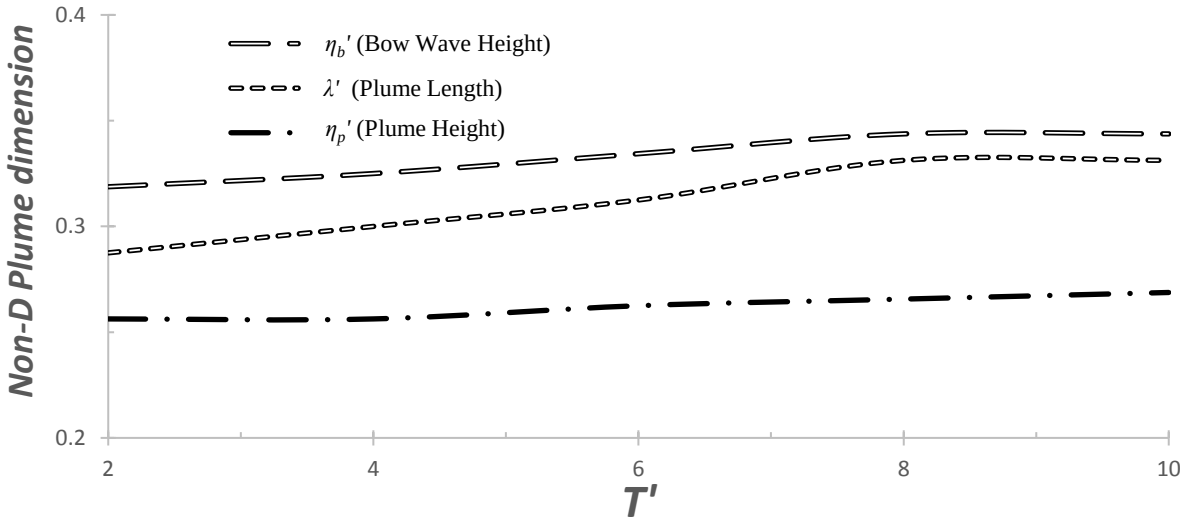

Figure 5.23: Non-dimensional plume parameters generated by cylinder with immersion depths to diameter ratio (*T'*) ranging from 2.0 to 10.0 at *Fr*=4.0.

5.4.3 Bow wave oscillations

The bow wave oscillations were recorded using the video camera positioned on the starboard side of the cylinder during the tow tank experiments (Figure 5.5). In order to measure the oscillations the video was viewed in 1/10th real time speed with each maximum and minimum bow wave height recorded in the time domain. The oscillations in the bow wave height occurred when the bow wave height reached a maximum value, at which point the bow wave fell away in all directions (including forwards) and the 'shedding' of the bow wave height created a clear and definite oscillation which was recorded as seen in Figure 5.24. The frequency of the recorded oscillations of the bow wave height showed no

correlation to the Froude number with a consistent frequency across all Froude numbers tested. Figure 5.25 shows the bow wave height generated by T'=10 without an end body. The data is presented as a percentage change in the bow wave height from the average recorded bow wave height. Over the recorded 10 second period, the number of peaks were recorded and the non-dimensional frequency, as calculated using $f'=Df^2/g$, was calculated to be $f'=4.1*10^{-3}$.

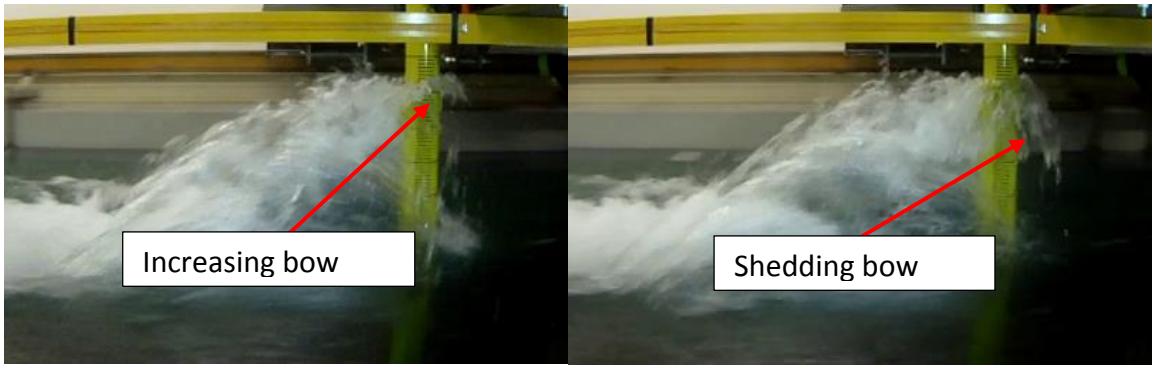

Figure 5.24: T'=10.0 immersion with no end body showing the 'shedding' of the bow wave height. Left image displaying the bow wave height increasing before shedding begins, right image capturing the shedding of the bow wave.

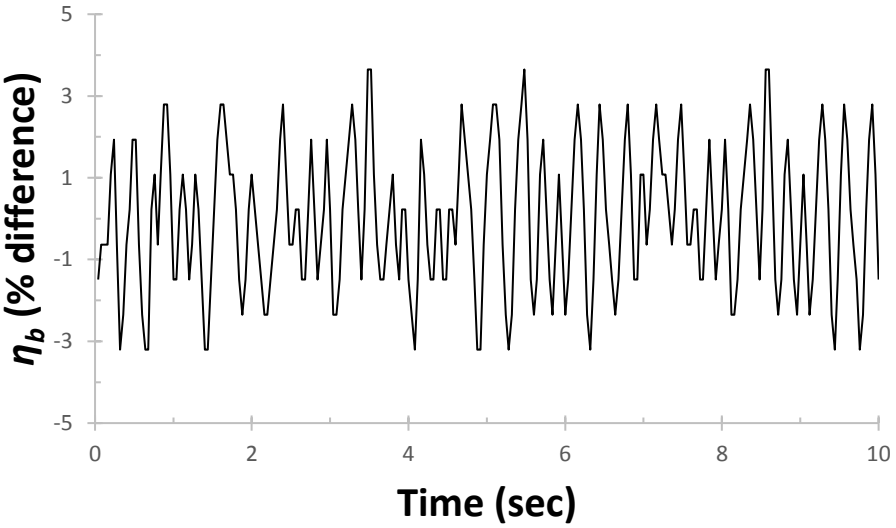

Figure 5.25: Bow wave height (η_b) oscillations at Fr=3.5 as a function of time. Difference in bow wave height calculated as percentage change from average bow wave height.

5.5 Concluding remarks

The experimental data generated during this study was used to validate the CFD-LES numerical simulation models for two cylinder immersion depths, both with and without an end body. Whilst the plume height was slightly under predicted by the numerical technique, which could be a result of a combination of under prediction of the stagnation pressure and over dissipation of energy in the turbulent flow at high Froude numbers, the bow wave height and plume length, and drag coefficient showed reasonable correlation. Most importantly, the numerical simulations accurately modelled the difference in plume structure for the different end conditions, thus allowing the numerical simulation technique to be used to quantify the effect of the end condition on the plume size and drag.

The numerical modelling of each configuration shows that the bow wave height, plume length, and drag coefficient are influenced by end effect. The addition of an end body for the T'=2.0 cases resulted in a 6-8% increase in the plume size. The increased plume size was very similar to the plume generated by extending the cylinder depth to T'=10.0 with no significant difference between the T'=10.0 with or without the end body. Thus, it is concluded that whilst insufficient cylinder depth can significantly affect the plume structure and drag results at low immersion ratios, the addition of an end body can remove the reduction in plume size caused by the free end effect at immersion depths as little as T'=2.0. A short cylinder with an end body has two significant benefits over a long cylinder without an end body. Firstly, the total drag of a short cylinder with end body is considerably less than a long cylinder. This allows a simpler and smaller test rig. Secondly, there are occasions when a long cylinder cannot be used due to experimental restrictions such as tank depth.

The stagnation pressure results suggest the reduction in plume size is due to a reduction in stagnation pressure. The addition of the end body resulted in approximately equal stagnation pressure as recorded for the T'=10.0 immersion depth.

In addition to the end body, the immersion depth was analysed to determine the required T' value in order to reduce the impact of end effect on the plume size. It was shown that at a Froude number of 4.0, the required cylinder immersion ratio to stabilise the end effect of a surface piercing cylinder with no end body attached is approximately T'=8.0.

Chapter 6

The Effect of Geometry on the Surface Waves Generated by Vertical Surface Piercing Cylinders with a Horizontal Velocity

This chapter is published in the “Journal of Engineering for the Maritime Environment”. The citation for the research article is:

Conway, A. S. T., Ranmuthugala, D., Binns, J. R., & Renilson, M. R. (2017). The effect of geometry on the surface waves generated by vertical surface piercing cylinders with a horizontal velocity. *Journal of Engineering for the Maritime Environment*.

Abstract

Bluff bodies advancing through a free surface at high Froude numbers create intricate flow patterns worth further investigation. An example of such flows include a submarine operating near the free surface which generally will have one or more masts piercing the free surface. These have the potential to produce large wakes at the surface. This paper describes the numerical analysis used to investigate possible design modifications to reduce the wake profile of a singular cylindrical mast piercing the free surface. The Large Eddy Simulation (LES) model carried out in OpenFOAM CFD software was validated against experimental data obtained by the authors using tow tank experiments.

The modifications included the use of a double mast system based on the cylindrical mast and truncated NACA0012 sections. All configurations were performed with a mast cross-sectional area corresponding to a typical submarine snorkel across speeds ranging from two to eight knots. The plume size and mast drag were recorded and the results show that a 30% reduction in wake profile can be obtained using a double mast system at speeds around eight knots, whilst at the lower speeds the benefit is not as significant.

6.1 Introduction

Conventional submarines have the operational requirement to approach and pierce the free surface with vertical appendages such as periscopes and snorkelling masts. Traditionally, these appendages have been bluff bodies such as a circular cylinder, which at typical submarine snorkeling speeds (< 5 m/s) generates unsteady flow along with a high and steep bow wave. Typically the bow wave separates from the appendage to develop a significant plume, detectable by radar or visual sighting. Therefore, it is necessary for the designers to develop systems that produce low wake plumes.

From published experimental data (Hay, 1947; Metcalf et al., 2006; Sumner, 2010), it is seen that at Froude numbers (Equation 6.1) greater than 3.0 the bow wave runs up the forward side of the cylinder and generates a large plume structure.

$$Fr = \frac{U}{\sqrt{gD}} \tag{6.1}$$

The results from recent experiments (Conway et al., 2016) showed that the plume is formed from two separate flow phenomena generated by the circular cylinder at high Froude numbers. Sumner (2010) suggests that the maximum possible height of the bow wave run up is based on the stagnation pressure and thus obeys Bernoulli's Equation (6.2),

$$\frac{\eta_b}{D} = \frac{Fr^2}{2} \tag{6.2}$$

where η_b is the bow wave height, *D* is the cylinder diameter, and *Fr* is the Froude number based on diameter. However, as the above equation is only valid for inviscid flow, it is more likely to apply at low Froude numbers and overestimate the bow wave height for viscous flow due to viscous losses. Therefore, this should be considered as an upper limit of the bow wave height.

The current work focuses on possible modifications to the vertical appendages both in shape and configuration in order to reduce the plume profile. Submarines, in general, have several cylindrical shaped masts at the free surface with each mast having a different purpose. Figure 6.1 shows the mast configuration of the *Astute* submarine with all masts extended. During submarine operations, only the required masts will be used resulting in often a single mast piercing the free surface.

Figure 6.1: Mast configuration on Astute class submarine. Taken from reference (Group, 2011).

A numerical approach using the open source Computational Fluid Dynamics (CFD) package OpenFOAM was used to replicate the wake recorded during the experimental investigation conducted at the Australian Maritime College (Conway et al., 2016). The simulations used Large Eddy Simulation (LES) with the One Eddy Equation turbulence model at speeds ranging between Fr=1.0 to 4.0, i.e. the typical speed range for a conventional submarine operating close to the free surface. Using the CFD simulations, five main parameters were investigated to determine the effect of altering the mast geometry and configuration. These include the bow wave height, maximum plume height, and plume length shown in Figure 6.2, as well as the individual and combined drag components of the appendages.

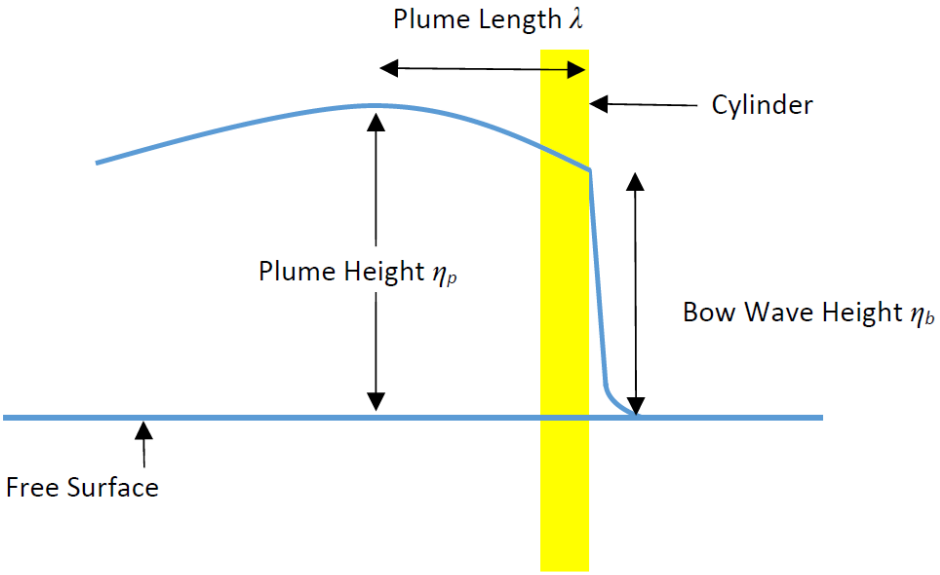

Figure 6.2: Definition of parameters used by Hay (1947).

The first set of simulations involved replicating experimental data in order to validate the numerical model. This consisted of a 0.1 m diameter cylinder with two different lengths: the first with the lower end 0.2 m below the free surface; and the second with the lower end 1.0 m below the free surface These two configurations had the submerged end of the cylinder free, creating instabilities at the boundary due to sudden changes in pressure.

The numerical code used throughout this paper was validated by comparison to the experimental data published by Hay (1947) and data collected by the authors (Conway et al., 2016). The data sets included the bow wave height, maximum plume height, and plume length. The validated code was used to investigate several alterations in the mast configurations of infinite length. This included configurations utilising three different circular cylinder diameters and two different NACA sections with equal total waterplane area. The combined waterplane area was maintained as this was considered a requirement for operational reasons. The first altered configuration consisted of two masts of diameter 0.0708 m, located 0.5 m apart along the direction of flow, i.e. located fore-and-aft. The second configuration increased the size of the forward mast to a diameter of 0.08 m whilst the aft mast was decreased to 0.06 m. The final configuration with the cylindrical masts was the reverse of the second configuration, i.e. the forward and aft masts diameters were 0.06

and 0.08 m respectively. Further investigations were conducted on a 1/3 truncated NACA0012 section (aft 1/3 of the foil section removed) with the same cross sectional area as the single 0.1 m diameter cylinder. The dimensions can be seen numerically in Table 6.1 and graphically in Figure 6.3.

Table 6.1: Mast geometry configurations used for numerical analysis.

	Ref #	Width (m)		Waterplane Area (m^2)		
Mast Geometry		Mast 1	Mast 2	Mast 1	Mast 2	Total
Single Cylinder	1	0.100	n/a	0.00785	n/a	0.00785
Double Cylinder (equal)	2	0.0708	0.0708	0.00394	0.00394	0.00787
Double Cylinder (small forward)	3	0.060	0.080	0.00283	0.00503	0.00785
Double Cylinder (large forward)	4	0.080	0.060	0.00503	0.00283	0.00785
Single NACA0012	5	0.041	n/a	0.00785	n/a	0.00785
Double NACA0012 (equal)	6	0.029	0.029	0.00393	0.00393	0.00786

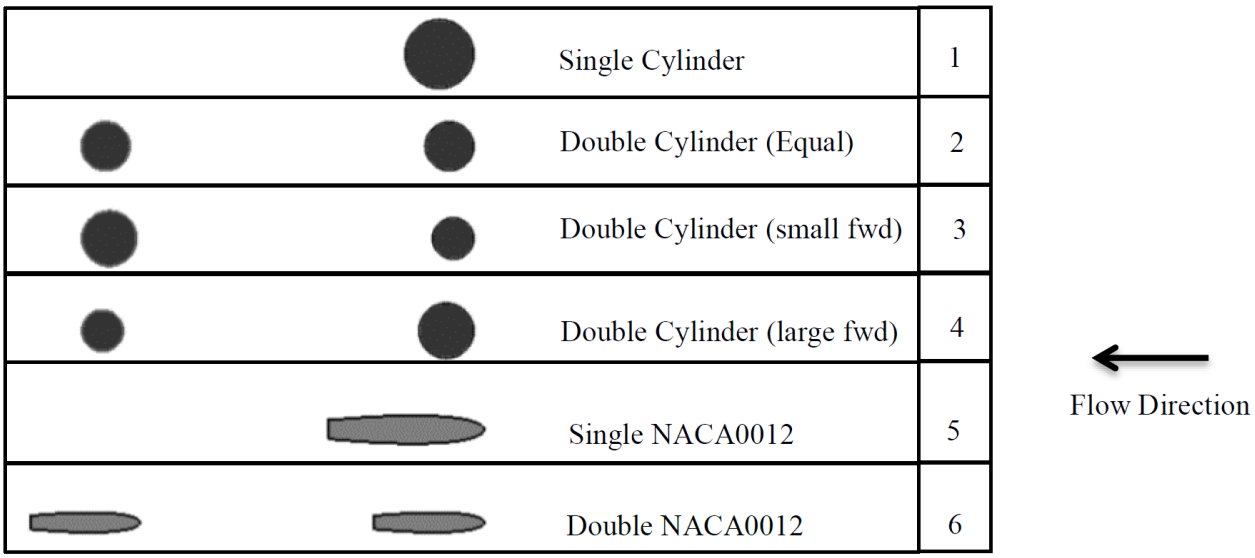

Figure 6.3: Visual representation of mast geometry configurations used for numerical analysis with constant total waterplane area.

Experimental data published by Sumner (2010) involving two cylinders with no free surface show a large area aft of the forward cylinder referred to as the wake interference region. The configuration used in this paper places the aft mast within this region, which would suggest that the aft mast is subjected to disturbed flow and thus will experience a changed plume structure.

6.2 Governing equations

The LES model used in this study was the OpenFOAM One-equation Eddy (oneEqEddy) model, which uses the Navier-Stokes equations utilising the Sub-Grid Scale (SGS) model to solve for the large eddies whilst modelling the smaller eddies (OpenFOAM-Foundation, 2013; Piomelli et al., 2001). The field is separated into a resolved part that represents the large eddies and a sub-grid part that represents the small scale eddies. The fundamental Navier-Stokes equations are in the incompressible form and can be expressed as,

$$\rho\left(\frac{dU}{dt} + U \cdot \nabla U\right) = -\nabla p + \mu \nabla^2 U \tag{6.3}$$

$$\nabla \cdot U = 0 \tag{6.4}$$

where ρ is the fluid density, U is the flow velocity, p is the fluid pressure, μ is the fluid viscosity, t is time, and ∇ is the divergence operator.

The One-equation Turbulent Energy model used within the OpenFOAM package is based on the eddy-viscosity concept with the addition of the sub-grid scale (SGS) to solve the transport equation. In the One-equation Turbulent Energy model, the assumption is made that the SGS turbulent energy is isotropic and can be expressed as (Penttinen, 2011);

$$\frac{\partial}{\partial t}(k) + \frac{\partial}{\partial x_i}(U_i k) - \frac{\partial}{\partial x_i}\left((v + v_{Eff}\frac{\partial}{\partial x_i}(k)\right) = -BL - \frac{c_e k^{\frac{2}{3}}}{\Delta} \tag{6.5}$$

where:

$$v_{SGS} = C_k k^{\frac{1}{2}} \Delta \tag{6.6}$$

$$\epsilon = \frac{C_\epsilon k^{\frac{3}{2}}}{\Delta} \tag{6.7}$$

and k is the kinetic energy, v is the eddy-viscosity, BL corresponds to the decay of the turbulence, ϵ is the turbulent dissipation, C_k=0.094 and C_ϵ=1.048. The left hand side of Equation (6.5) can be broken down into each term. The first term is the change in turbulent

SGS kinetic energy with respect to time. The second term defines the convection and the third term describes the diffusion.

6.3 Simulation Parameters

The flow around the masts was considered to be incompressible, turbulent, and two phase (air and water). The single cylinder mast was non-dimensionalised with respect to the maximum width of the mast (diameter) to perform validation with respect to published experimental data using both Froude number (Equation 6.1), and Reynolds number, $Re = \rho UD/\mu$. However, due to different diameter masts between each configuration, the results of the different mast configurations were compared directly based on an effective diameter using the total waterplane area (A_w). Thus, the effective diameter (D) used to calculate the respective Froude number and Reynolds number was calculated as shown in Equation (6.8).

$$D = \sqrt{\frac{4A_w}{\pi}} \tag{6.8}$$

Although the configurations with a smaller frontal area produce smaller plume structures, using a conventional non-dimensional method, such as frontal area, results in a larger value. This could be interpreted incorrectly as the larger forward cylinders generated smaller plumes. The use of effective diameter ensures that all configurations are non-dimensionalised in a method that provides data accurately, without confusion.

The simulations used a consistent numerical domain and grid with minor changes to adjust for varying mast geometries. The grid was optimised for a Froude number of 4.0 to ensure the entire plume structure was captured along with wake resolution and boundary effects. The difference between each grid for the different mast geometries was at the mast surfaces in order to maintain a similar y^+ value of between 30 and 40. y^+ is a non-dimensional value used to define how close the first mesh cell is to the surface of the mast. The value of y^+ is calculated using Equation (6.9).

$$y^+ = \frac{yu_\tau}{\nu} \tag{6.9}$$

where *y* is the distance to the wall, u_τ is the friction velocity, and υ is the kinematic viscosity. The meshing application used was the inbuilt OpenFOAM meshing software snappyHexMesh due to the ability to use hanging nodes. Hanging nodes are treated in a similar method to multigrid algorithms, where the corresponding data is interpolated when increasing the mesh resolution (going from a coarser to a finer grid level) and inversely restricted when stepping up again through the use of the ansatz functions (Neckel, 2009).

The domain dimensions were sized to fully capture the plume profile with sufficient area around the plume to allow for diffusion of the turbulence before reaching the boundaries. Using hanging nodes, the mesh was refined in areas of interest around the plume structure and along the free-surface. The refinement level was specified by the number of times a cell was split by 2^n, where *n* is the refinement level. A combination of refinement levels of 2, 3 and 4 were utilised at different locations within the domain. The refinement areas were concentrated to areas 120% larger than the expected plume size with a rapid decrease in grid resolution towards the domain boundaries in order to numerically dampen the wake before it makes contact with the boundaries in order to reduce wave reflections from the boundary and thus increase the stability of the simulation and reduce the simulation time and effort.

6.4 OpenFOAM setup

OpenFOAM provides the user significant control over the simulations in terms of directly changing the settings within the software, changing equations or parameters (Yun, 2014), and inserting user written scripts. This includes the ability to select the linear system solvers, interpolation schemes, and the solver settings. This is done through pre-selecting the chosen solvers/settings in the corresponding scripts which are called on during the simulation at the required times.

Due to the inherent instabilities and turbulence created by a bluff body at high Froude numbers, the interpolation schemes and solvers were selected on two main criteria,

with the primary criterion aimed at improving simulation stability without a reduction in accuracy, whilst the secondary criterion was to reduce computational requirements.

The Preconditioned Conjugate Gradient (PCG) linear system solver with Geometric-Algebraic Multi-Grid (GAMG) as a pre-conditioner was used for solving the pressure, as the pressure was found to be extremely sensitive to instabilities while the PCG solver increased the stability of the simulations. A GAMG pre-conditioner was applied to decrease to computational effort required by generating a quick solution using a course mesh to generate an initial condition for each time step (Foundation, 2013). The velocity was solved using the OpenFOAM's default set-up Preconditioned BiConjugate Gradient (PBiCG) solver with Diagonal Incomplete LU (DILU) as the pre-conditioner, as the simulations appeared to have little effect from changes in the velocity solvers.

Due to the use of a LES model, there are typically no wall functions applied. However, to reduce computational requirements, the *kqRWallFunction* was applied to the *k* field. This wall function allows for an increase in the boundary sub-layer grid height from a y^+ of 1 up to 30-40 as recommended by the OpenFOAM manual (OpenFOAM-Foundation, 2013) with a y^+ study conducted in the next section to ensure that the recommended y^+ is applicable for this study.

A combination of the Pressure-Implicit Split-Operator (PISO) and Semi-Implicit for Pre-conditioner Equations (SIMPLE) algorithms referred to as PIMPLE was used for all simulations. The difference between the two algorithms is that SIMPLE can only make one correction whereas PISO requires more than one correction. The PIMPLE algorithm has more similarities with the PISO algorithm, with the addition of outer correction loops and under-relaxation of the variables between the outer iterations.

6.5 Numerical verification and validation

In order to validate the numerical code used in this study the results were compared with published experimental data by Wickramasinghe et al. (1997) cited by Yu et al. (2008), Hay (1947), and Conway et al. (2016). The experimental data by Wickramansinghe was very

limited and only consisted of the bow wave height over the Froude number range from 0.8 to 3.0. Hay published an extensive range of experimental data ranging in Froude numbers up to 4.9, measuring the plume profile dimensions as shown in Figure 6.2. Conway et al. (2016) published data for both short and long cylinders up to a Froude number of 4.0. The parameters used to validate the LES simulation model used in this study were the bow wave height, η_b, plume height, η_p, and plume length, λ as defined in Figure 6.2. The results were compared between the experimental and numerical results with respect to diameter Froude number.

A grid independence study was conducted at a Froude number of 4.0 using the LES model and the solvers mentioned in Section *2.2 OpenFOAM setup*. The main areas of interest included the effect of the inflation layers within the boundary layers as well as the density and aspect ratio of the elements required in the plume region (Figure 6.4). The influence of the boundary inflation layer was analysed by comparing the bow wave height, η_b variation with respect to the calculated y^+ (Equation 6.9).

As shown in Figure 6.5 for the results from the y^+ study, a plateau of the bow wave height was achieved at a y^+ of between 30 and 40, and thus all simulations were completed with a boundary inflation layer such that the y^+ value was maintained around 35. Furthermore, the mesh density in the plume region was analysed and the plume height and plume length were compared. Figure 6.6 shows relative mesh insensitivity when compared to a 14 million cell mesh at a mesh size of 8-10 million elements, and therefore, a mesh of approximately 10 million elements was used. Since there was a distinct plateau indicating grid independence, it was determined that the ratio of modelled to resolved turbulent kinetic energy was not required in order to determine the suitability of the mesh.

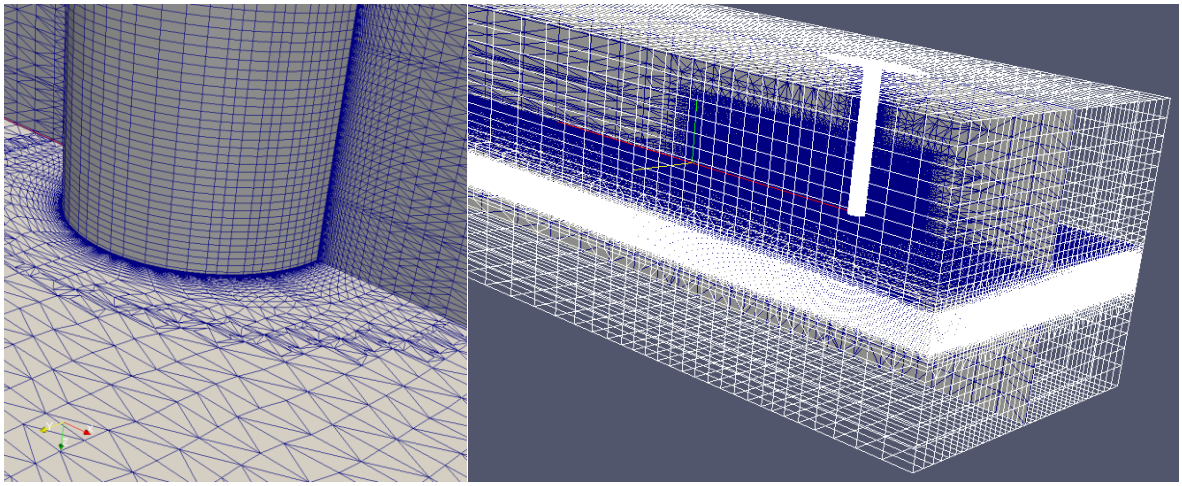

Figure 6.4: Numerical domain showing inflation layer (left) and refinement areas (right).

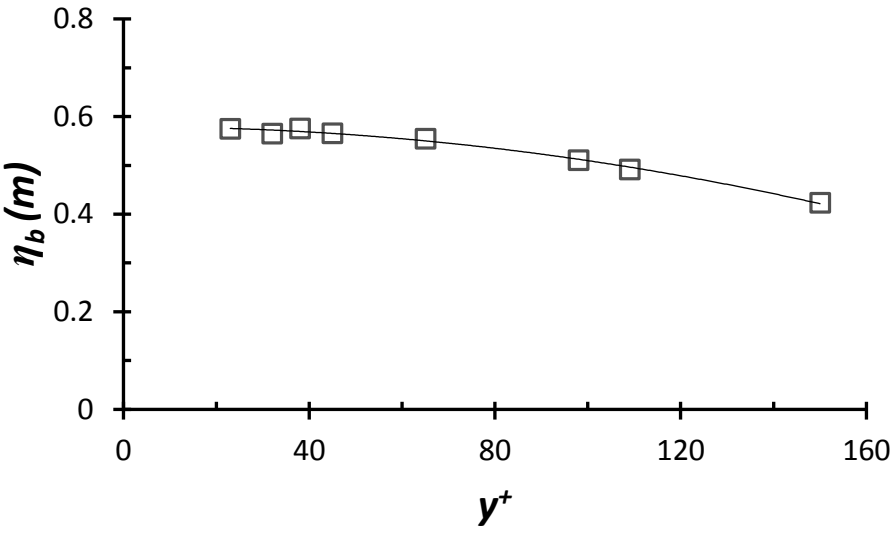

Figure 6.5: Grid independence study based on y^+ and bow wave height (m). Squares represent predicted data points, with line of best fit plotted.

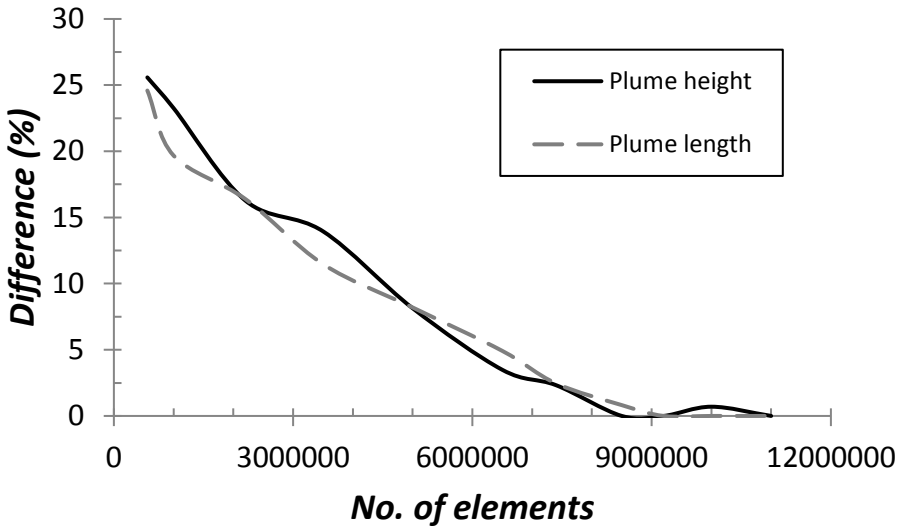

Figure 6.6: Mesh density study using plume height and plume length plotted as percentage difference in the results when compared to a 14 million element mesh, plotted against mesh size (number of elements).

6.6 Validation

The data presented in the figures below have been non-dimensionalised with respect to the Froude number where the non-dimensionalised bow wave height:

$$\eta_b' = \frac{\eta_b}{DFr^2} \tag{6.10}$$

similarly for plume height and plume length:

$$\eta_p' = \frac{\eta_p}{DFr^2} \tag{6.11}$$

$$\lambda' = \frac{\lambda}{DFr^2} \tag{6.12}$$

Figures 6.7 to 6.9 show the data obtained from the LES simulations compared to the experimental data published by Yu et al. (2008), Hay (1947), and Conway et al. (2016).

Figure 6.7 is the experimental data for the bow wave height (η_b') as a function of *Fr*. This shows that the bow wave height from the LES simulations up to a Froude number of 2.5

was within the error bars obtained from the experimental data. At higher Froude numbers the bow wave height (η_b') was underestimated. At Fr = 4.0 η_b' was underestimated by approximately 5% for both the short and long cylinders. The upper limit line was obtained from Bernoulli's equation based on the stagnation pressure (Equation 5.1). There is a critical transition in the flow regime at a Froude number of approximately 3.25 which results in a theoretical drop in drag coefficient. The flow regimes experienced by a cylinder at the simulated Froude numbers, as published by Sumer et al. (1997), are sub-critical , critical, and super-critical flow regimes. Sub-critical flow includes a laminar boundary layer and laminar separation points. Critical flow is the transition stage when the boundary layer is laminar but the boundary layer separation points becomes turbulent. At a higher flow velocity the flow becomes sub-critical resulting in the boundary layer becoming turbulent.

Whilst there is a small increase in bow wave height coefficient at Fr=3.25 seen in the experimental data, which could be a result of the changed flow regime resulting in more energy in the bow wave rather than vortex shedding (drag), the change is within the experimental error and thus more investigation is required in this area.

The experimental data for plume height (η_p') and plume length (λ') published is shown in Figures 6.8 and 6.9 with the numerical results. It can be seen that the plume length predictions from the experimental results and the numerical data have a good correlation for both cylinders depths. The plume height has a greater variation between the three sets of data with a closer correlation to the experimental data collected in previous investigations. Both the numerical and experimental results indicate there is a definite difference in the plume profile between the two different length cylinders.

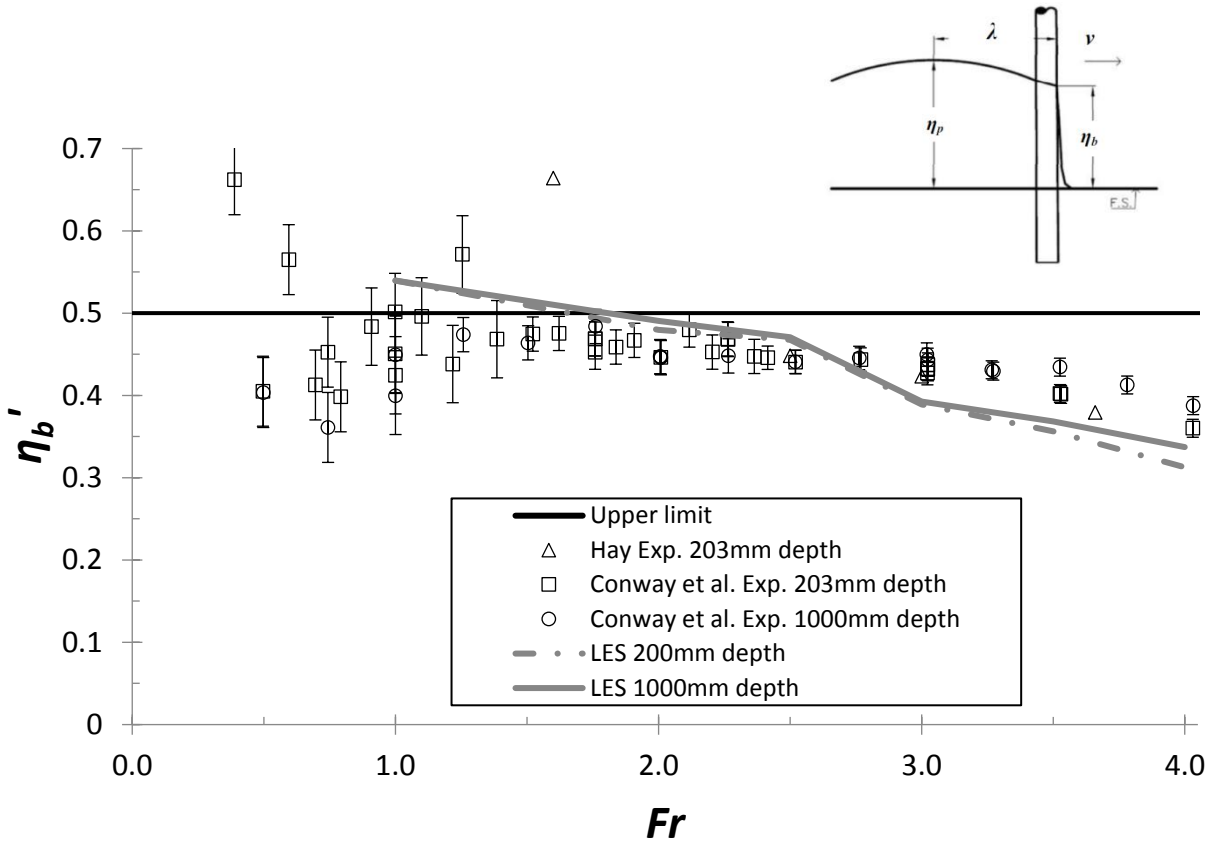

Figure 6.7: Comparison of bow wave height, η_b', variation with respect to Froude number, *Fr*, experimental data from Hay (1947), Conway et al. (2016), and numerical data (LES).

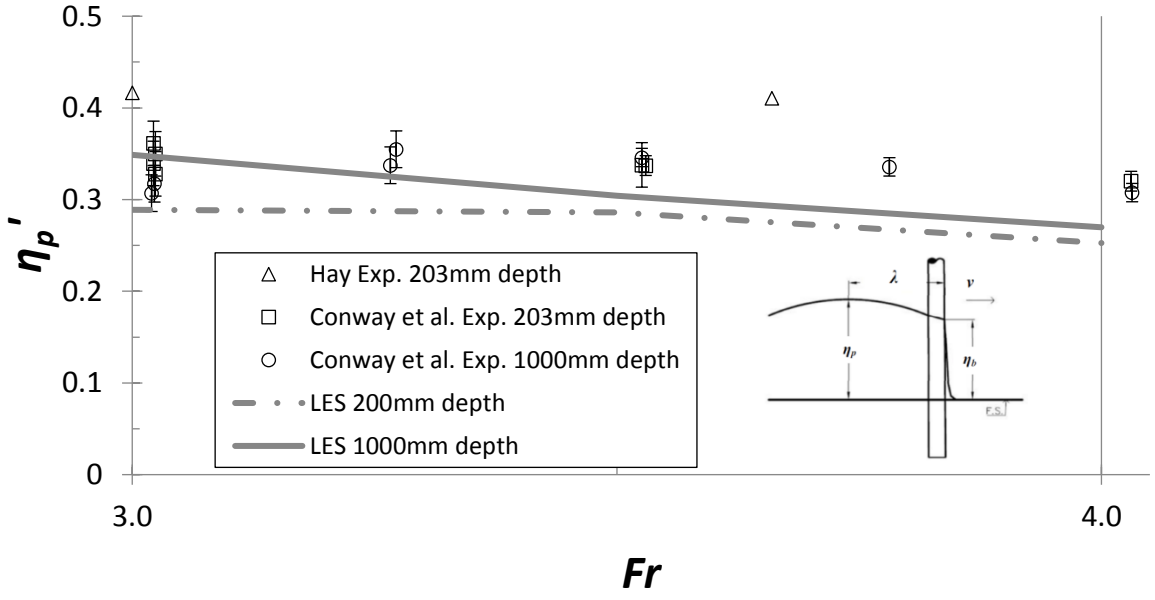

Figure 6.8: Comparison of plume height, η_p', variation with respect to Froude number, *Fr*, data from Hay (1947), Conway et al. (2016) and numerical data (LES).

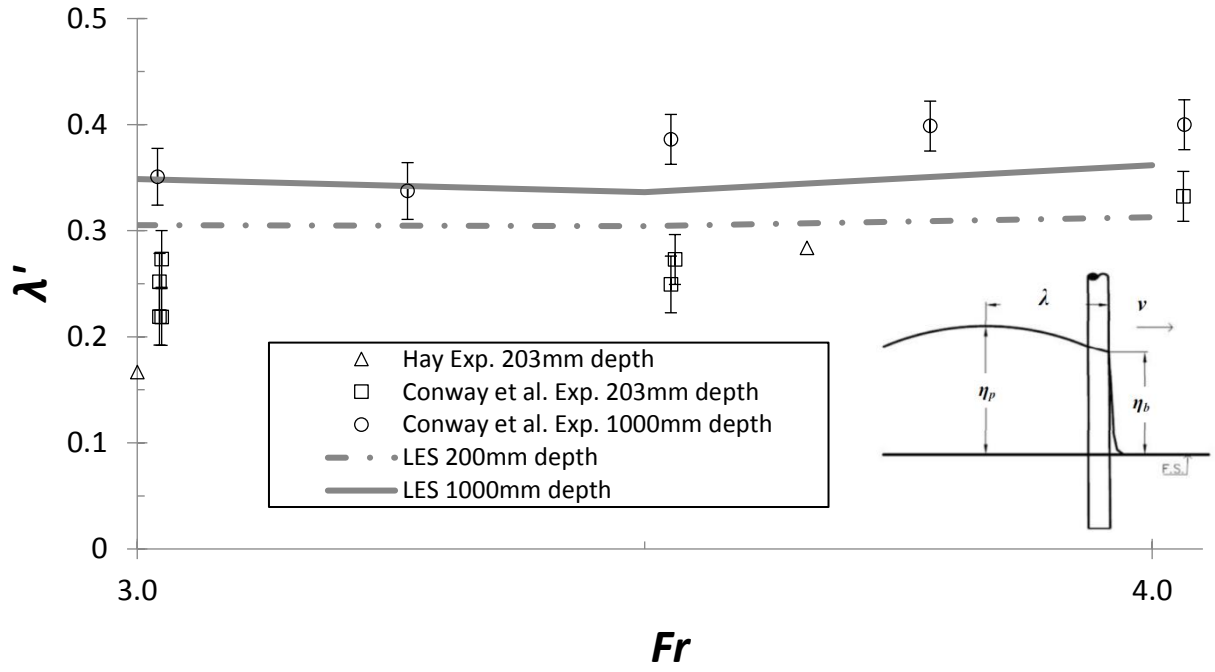

Figure 6.9: Comparison of plume length, λ', variation with respect to Froude number, data from Hay (1947), Conway et al. (2016) and numerical data (LES).

The drag coefficient for the cylinder was also compared against the data published by Hay (1947), Conway et al. (2016) and Cathcart (2014) as shown in Figure 6.10. The drag coefficient was calculated using the cross sectional area:

$$C_D = \frac{F}{\frac{1}{2}\rho U^2 A} \tag{6.13}$$

where F is the drag force, ρ is the water density, U the flow velocity and A is the cross sectional area as calculated using:

$$A = Diameter \times Height \tag{6.14}$$

At a Froude number of 1.0 there is an increase in the drag coefficient in both the experimental and numerical data which is likely caused by a change in wave pattern dependent on Froude number. Furthermore, the experimental and numerical data follow a similar trend throughout the range of Froude numbers with the exception of a small increase in the experimental data at Fr = 2.25. A significant drop in the measured drag coefficient can be seen for the long cylinder at a Froude number of 3.25. This drop occurs at

the transition in flow regime from a sub-critical to critical and quickly into super-critical flow regime (Sumer et al., 1997; Tritton, 1988). Due to the fact that the dip is not present in the short cylinder cases this suggests that the end effect has a larger influence on the drag of the cylinder than the change in flow regime around the cylinder. The severity of the drop in drag for the long cylinder has not been captured by the numerical predictions. The cross over in drag coefficient (that is the fact that the long cylinder has a higher drag coefficient at Fr < 2.5 and a lower drag coefficient at Fr > 2.5) has been predicted well by the numerical simulations following the same trend as seen in the experimental data.

Overall, between the drag and plume measurements, both the short and long cylinder simulations followed the same trends as the measurements. Therefore, the parameters and numerical set-up used for this paper are applicable to study the effect of mast geometry on plume profile.

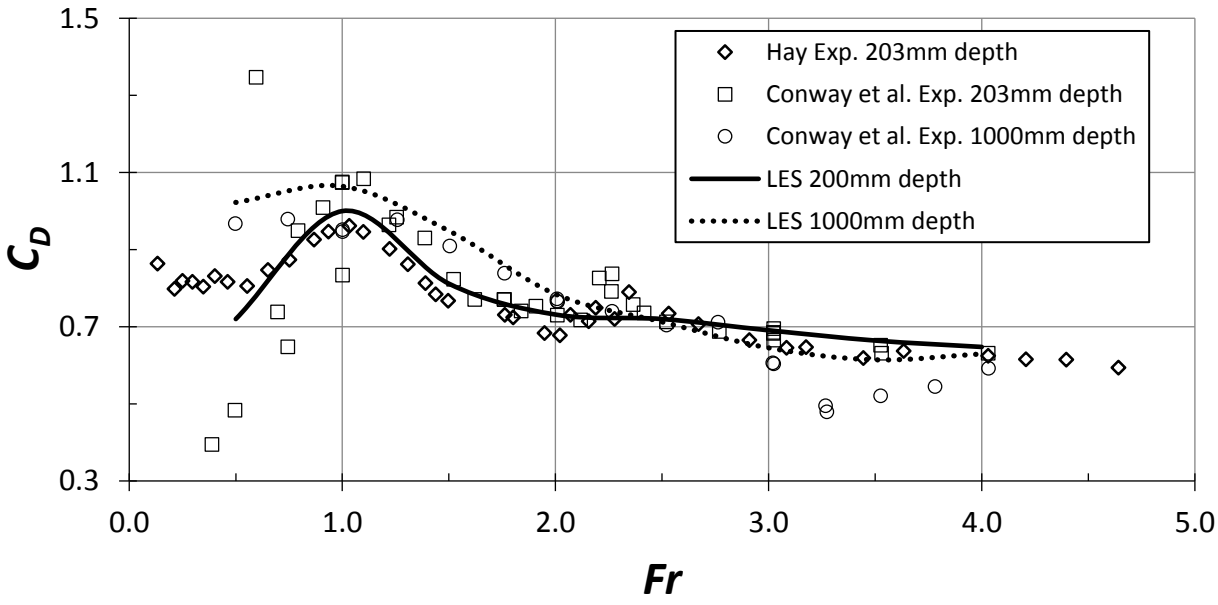

Figure 6.10: Comparison of drag coefficient as a function of Froude number, data from Hay (1947), Conway et al. (2013) and numerical data (LES).

6.7 Numerical investigation

6.7.1 Geometry

This study performed a numerical analysis on several different mast set-ups and geometries. All mast configurations were extended to the bottom of the numerical domain to increase numerical stability and better reflect a mast connected to a submerged body. In addition, this study has included two masts configurations, and the addition of a NACA section. All results have been compared to the single cylinder having a diameter of 0.1 m. The water plane area of each set-up was constant to the 0.1 m diameter cylinder. Table 6.1 shows the dimensions of each configuration used in the simulations and Figure 6.3

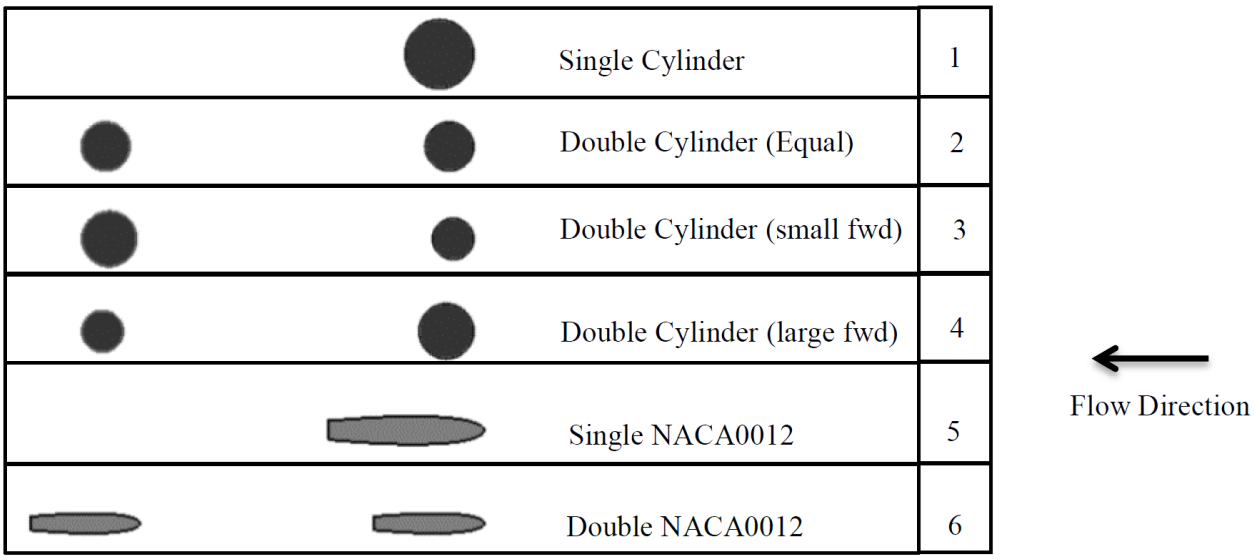

displays the mast geometries graphically. Due to the fact that these simulations are to compare different mast geometries under the same conditions, all results have been non-dimensionalised using an effective diameter based on the total area of the masts in order to calculate the diameter Froude number. The effective diameter was calculated by rearranging the equation for the area of a circle and shown in Equation (6.8).

6.7.2 Reynolds Number investigation

As a result of varying the diameter of the masts, the diameter based Reynolds number ranged between approximately 2.4×10^5 to 4×10^5 at Fr = 4.0. As mentioned earlier, there is a change in flow regime from sub-critical to super critical flow at a Reynolds number

around $3.2x10^5$, which was shown above to affect the drag of a deep cylinder. Therefore, to ensure any changes observed are due to a smaller mast and not a change in flow regime, an investigation into bow wave height, plume length, and plume height was compared to Reynolds number was conducted with constant speed and cylinder diameter (0.1 m) with a resulting Froude number of 4.0. This was achieved by altering the viscosity within the numerical simulations whilst maintaining all other variables constant, with a resulting Reynolds number range from $1x10^4$ up to $4x10^5$ as shown in Figure 6.11. Between the Reynolds numbers $1.5x10^5$ and $4x10^5$ there is no significant change in the bow wave height and therefore, no changes in the operating range of Reynolds numbers for the configurations tested. It should also be noted that there is a small decrease in the non-dimensional bow wave height at lower Reynolds numbers (Re<$1x10^4$) as the flow approaches another change in flow regime. Therefore, although the Re/Fr correlation varies with each mast configuration at each Froude number, this has shown that any changes in the plume size is not a result of varying Re/Fr, but a result in change in geometry.

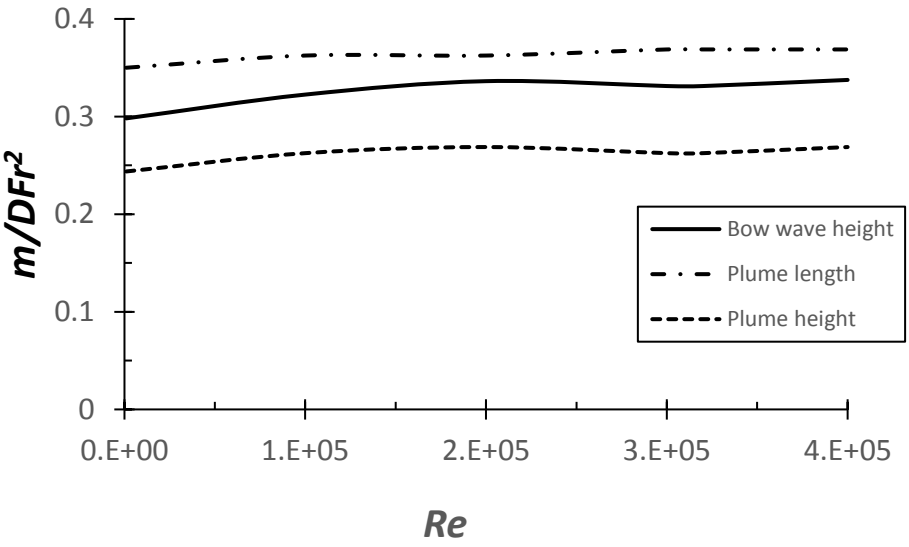

Figure 6.11: Non-Dimensional bow wave height, plume length, and plume height as a function of Reynolds number at a constant Froude number of 4.0. *m* represents the bow wave height, plume height or plume length in metres.

6.8 Results and discussion

6.8.1 Wake on circular cylinder configurations

The plume profile for several mast configurations was modelled at a range of Froude numbers from 1.0 to 4.0 at 0.5 intervals. These results were analysed to determine η_b, η_p, and λ in each configuration. The drag force on each mast was also compared to further understand the effect of the wake generated by the forward mast on the aft mast.

The resulting plume visualisations for the single and double mast configurations are shown in Figure 6.12 – Figure 6.14. For the tested mast configurations, it was found that aft mast wake was completely 'hidden' by the wake generated by the forward mast, including the cases when the forward mast was much smaller than the aft mast. This was due to the significant wake region the forward cylinder created greatly reducing the wake produced from the aft mast. This also suggests that moving the aft mast forward may have minimal effect on the overall plume size generated. As a result, further work could be undertaken to determine the critical size of the forward mast in order to generate the smallest wake possible whilst still 'hiding' the wake generated by the aft mast. This would help determine the best ratio of forward mast diameter to aft mast diameter along with the optimum separation between the two masts.

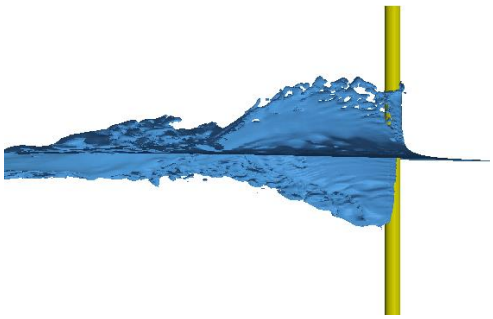

Figure 6.12: Plume profile generated by single mast configuration at Fr=4.0.

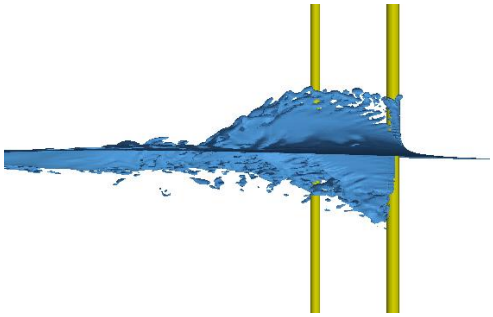

Figure 6.13: Plume profile generated by double mast (large forward) configuration at Fr=4.0.

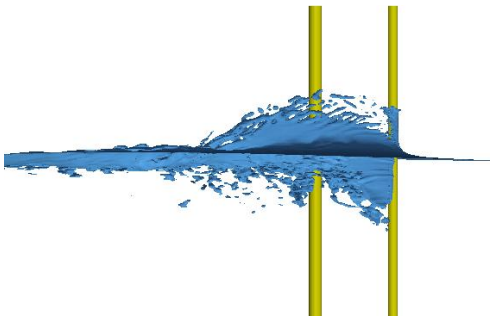

Figure 6.14: Plume profile generated by double mast (small forward) configuration at Fr=4.0.

Due to the small plume structure generated by configurations 5 and 6, only the results from the cylindrical masts are presented in the following section. Similarly, at Froude numbers less than 3.0, data for η_p and λ was not collected at the lower speeds due to lack of fully developed plume structures. Figure 6.15 shows the size of the bow wave heights generated by the forward mast for cylindrical mast sections. At lower speeds it can be seen that the difference between the various mast configurations is minimal, however, at Fr=4.0 the bow wave height generated by the double (small forward) configuration is approximately 30% smaller than the bow wave generated by the single mast configuration. It was also noted that the aft cylinder did not generate a bow wave similar to the forward cylinder suggesting a significant reduction in stagnation pressure.

The plume height and plume length generated by each cylindrical mast configuration are shown in Figure 6.16 and Figure 6.17. Whilst the plume length and plume height data followed the same trend as the bow wave height, there was only an 18% average reduction between the largest and smallest plume height and length predicted at a Froude number of 4.0.

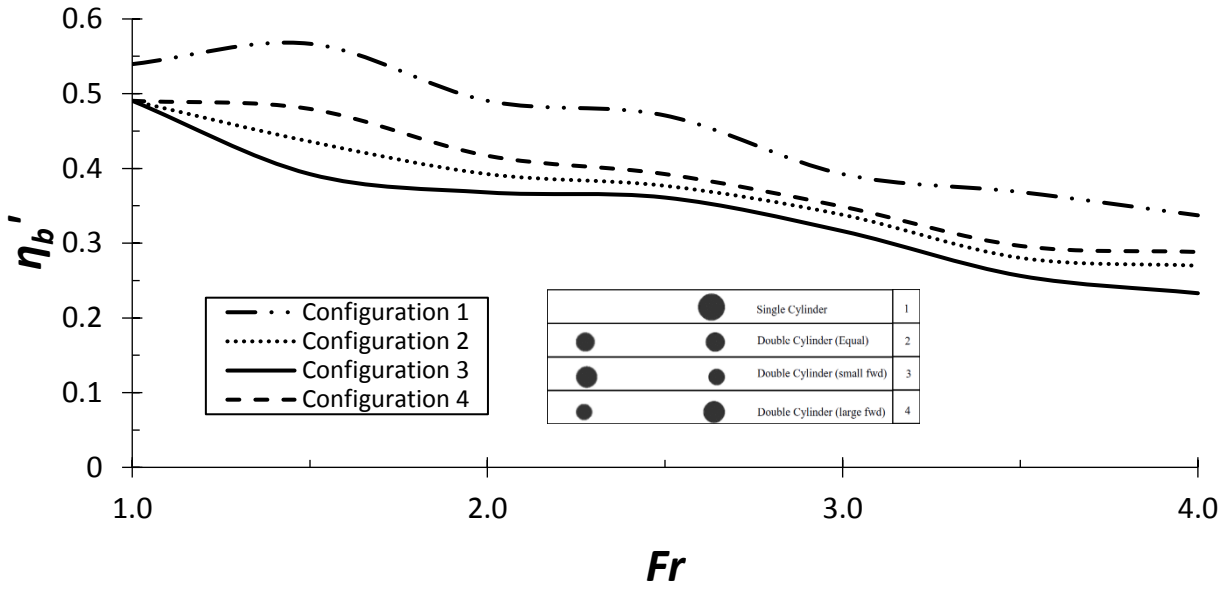

Figure 6.15: Non-dimensional bow wave height, η_b', generated by the forward mast (cylindrical cross-section) as a function of Froude number.

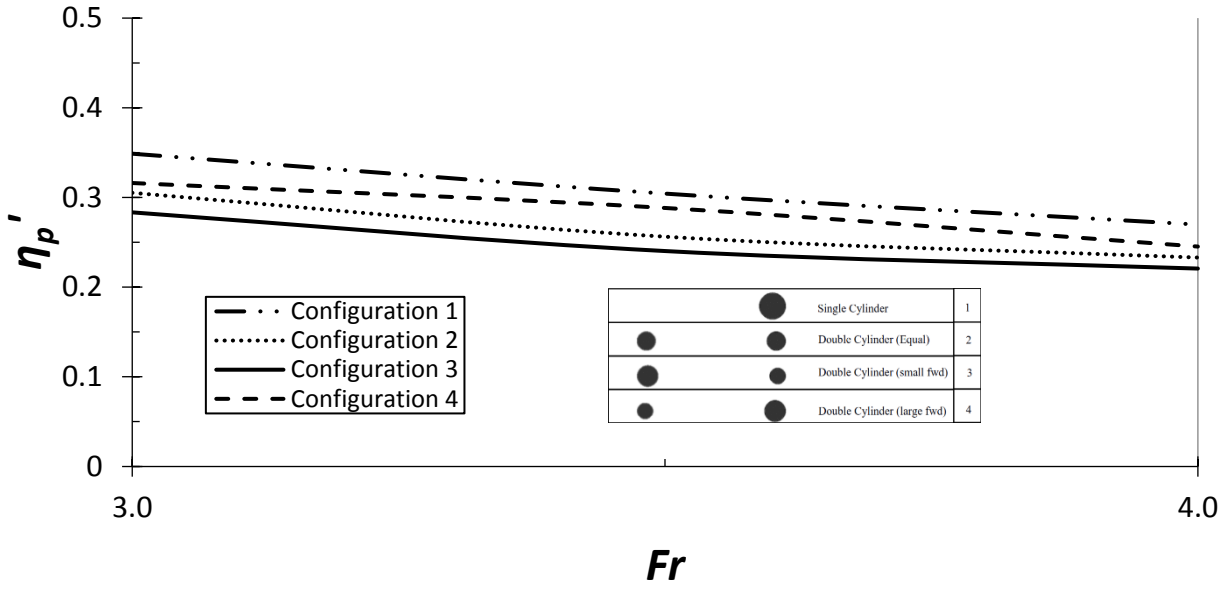

Figure 6.16: Non-dimensional plume height, η_p', generated by the forward mast (cylindrical cross-section) as a function of Froude number.

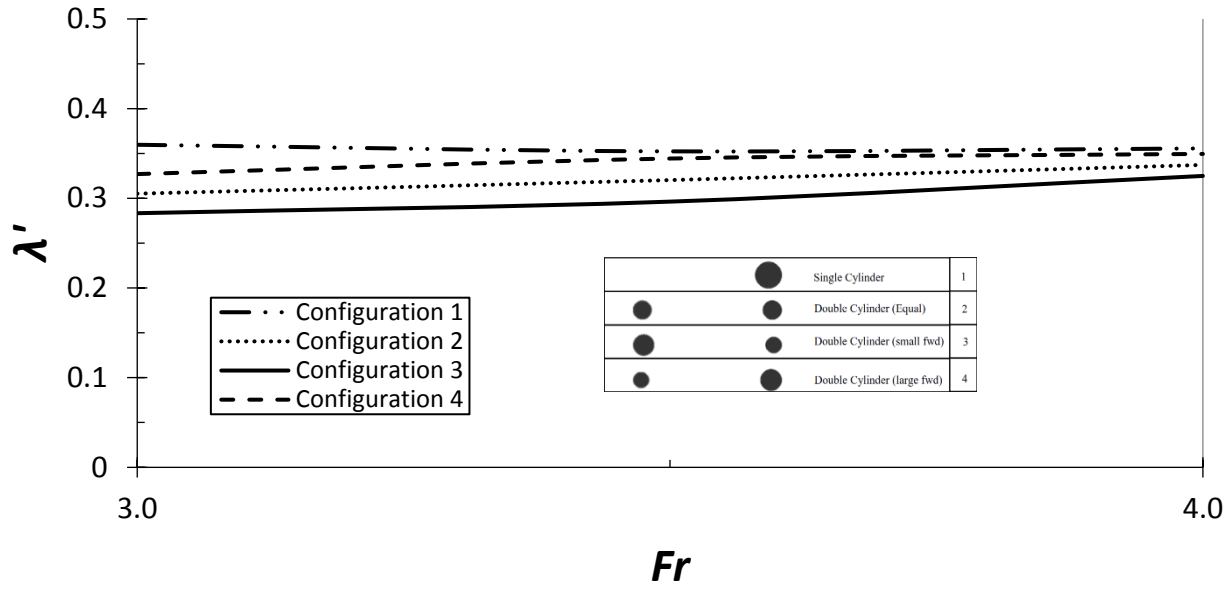

Figure 6.17: Non-dimensional plume length, *λ'*, generated by the forward mast (cylindrical cross-section) as a function of Froude number.

6.8.2 Drag on double mast configurations

The wake interference region is critical to reducing the plume generated by the aft cylinder and assists in explaining the reason that the aft cylinder generates a significantly reduced plume. Figure 6.18 shows an increase in the total drag encountered by the forward cylinder when travelling at Fr = 2.0 (Figure 6.19 shows the decrease for the aft mast). This could indicate a transition in the wake profile or flow regime around the cylinder. Sumer (1997) stated a transition into the subcritical flow regime at Reynolds numbers corresponding to the Froude numbers between 2.0 and 3.0. Additionally a much larger drag force is generated on the forward cylinder than the aft cylinder, with a maximum of approximately 78% greater for configuration four (double cylinder with larger mast forward). Additionally, the total drag on the cylindrical mast configurations is presented in Figure 6.20 which shows that the total drag is slightly increased with the use of a double mast configuration. Furthermore, there is little changes in the total drag between the double mast configurations.

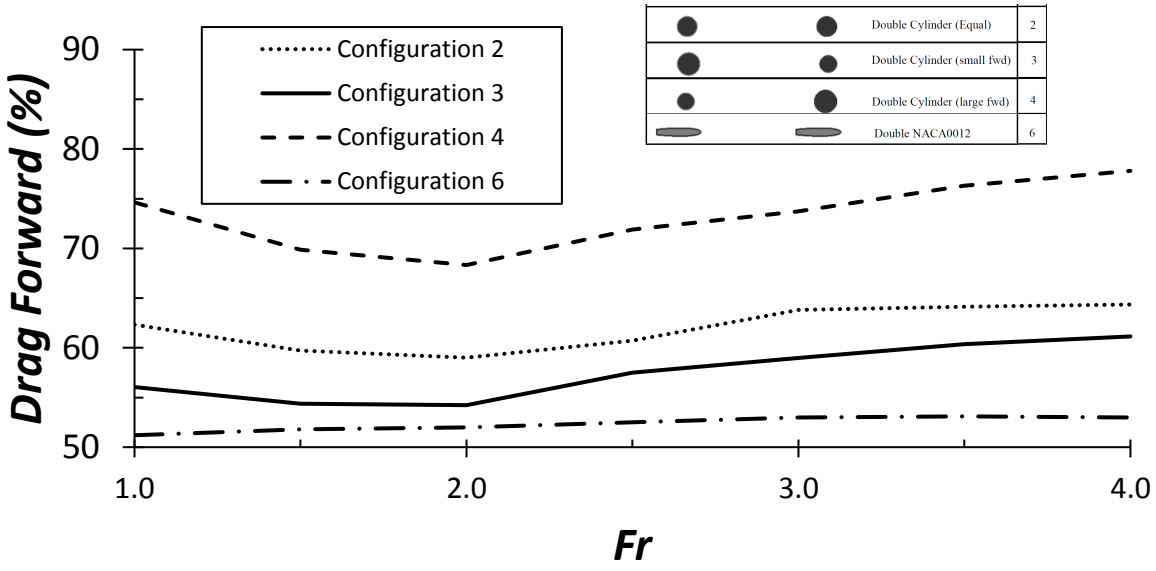

Figure 6.18: Percentage of total combined drag from both cylinders on the forward mast for the double mast configuration.

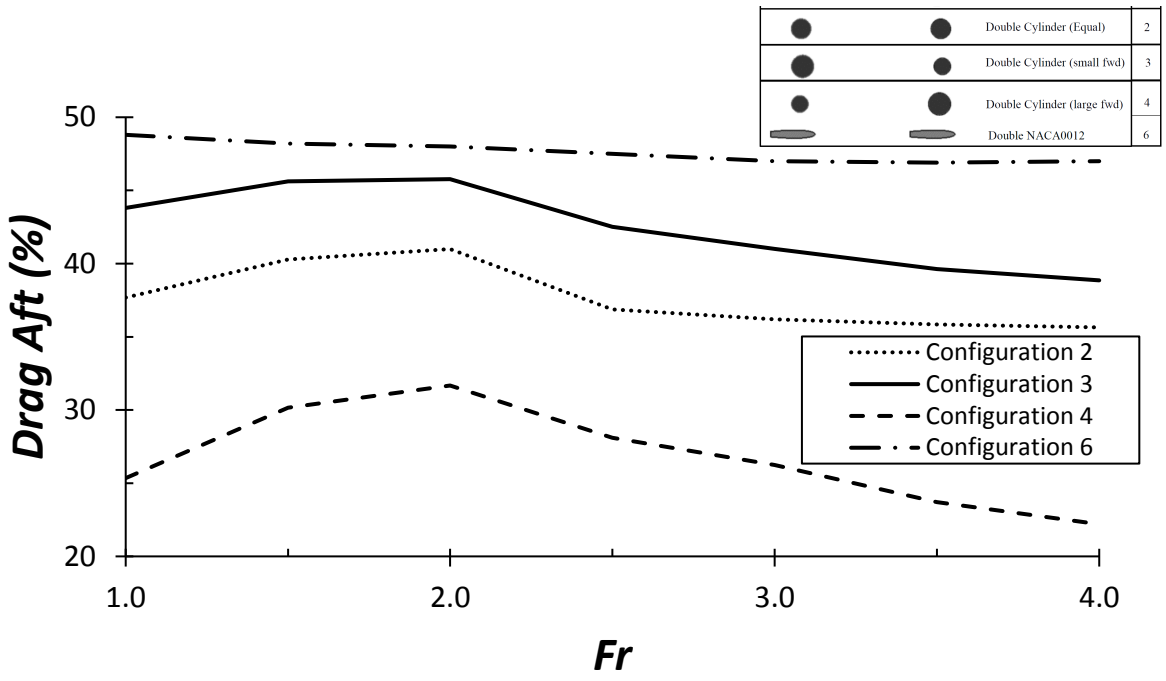

Figure 6.19: Percentage of total combined drag from both cylinders on the aft mast for the double mast configuration.

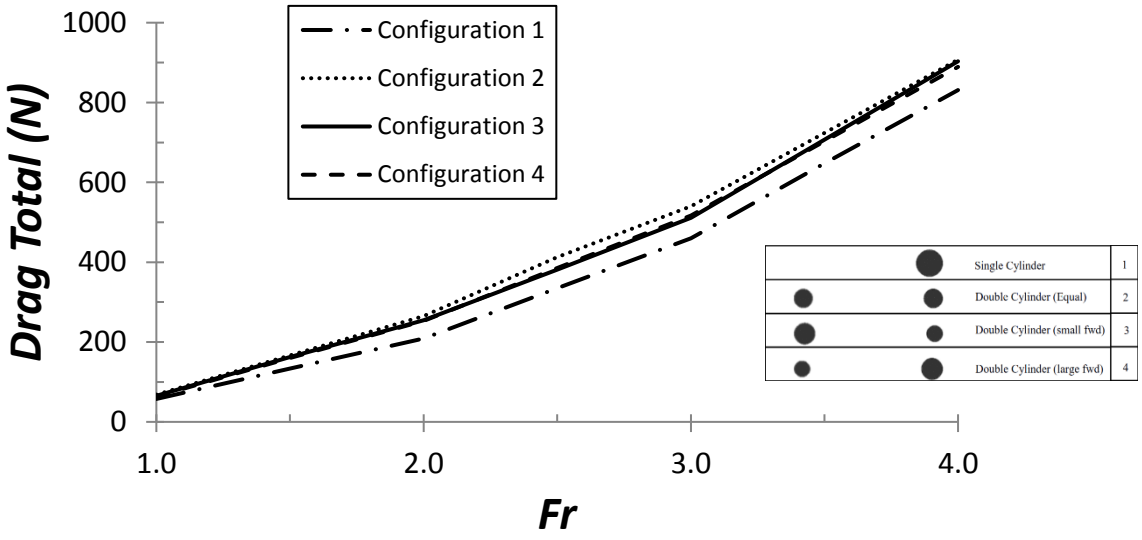

Figure 6.20: Total drag on the cylindrical masts at Froude numbers 1.0 to 4.0

6.8.3 Wake on streamlined cylinder configurations

Further simulations were conducted using truncated NACA0012 sections to analyse the possible benefits of using a streamlined body rather than a bluff body. The NACA0012 and single mast configuration were compared using the bow wave height, whilst the plume length and height (η_p and λ) were not analysed due to the relatively small plume profile generated by the NACA section mast.

Figure 6.21 shows the non-dimensional bow wave height plotted as a function of Fr for the single cylinder (configuration one) and the NACA sections (configurations five and six) whilst Figure 6.22 shows the plume generated by a single NACA section mast which both indicate a significant reduction in the plume profile. It can also be seen in Figure 6.21 that the difference between the plume generated by the single and double NACA0012 sections is minimal when compared to the reduction in plume size between the cylindrical and NACA masts. At Fr=4.0, the double NACA0012 section offers approximately 80% reduction in the bow wave height, whilst the single NACA0012 section offers a 75% reduction.

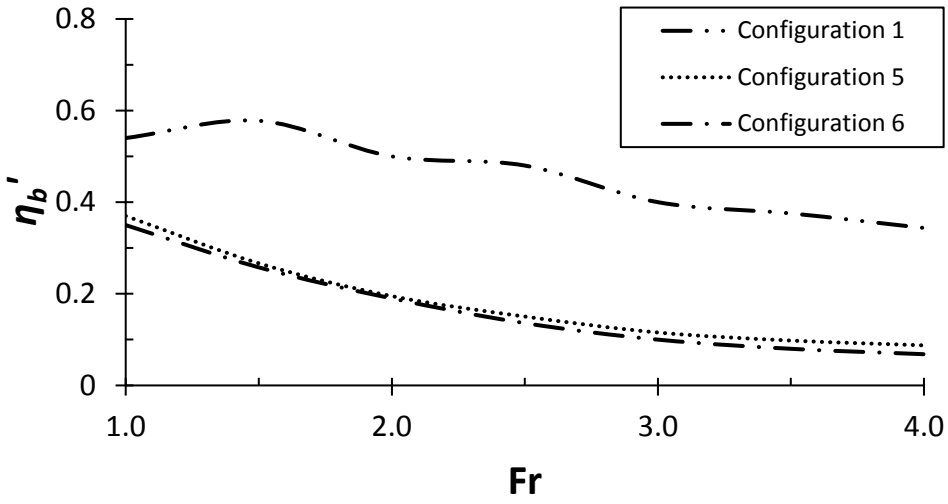

Figure 6.21: Non-dimensional bow wave height, η_b', for NACA0012 and cylindrical mast configurations as functions of Froude number.

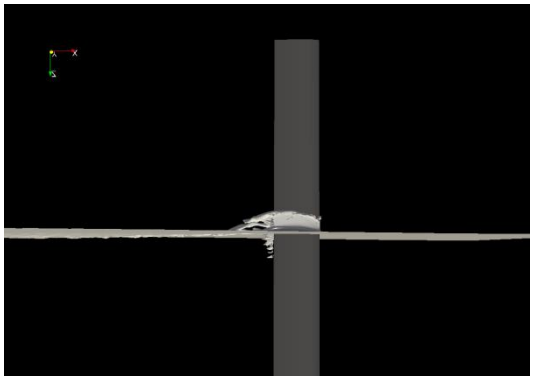

Figure 6.22: Plume profile generated by NACA0012 mast configuration at Fr=4.0.

6.8.4 Pressure distribution for cylinder and streamlined configurations

As mentioned in the previous section, the streamlined configurations offered a significant reduction of the bow wave height. The reasons for such a significant reduction can be explained by both stagnation pressure and frontal area. Figure 6.23 shows a plan view of the two mast geometries with the same water plane area. It is clear from this image that the frontal area is reduced significantly by utilising the NACA section. This difference can also be seen numerically in Table 6.1, which shows the width of the NACA0012 section is less than half the width (diameter) of the cylinder (0.1 m compared to 0.041 m for the NACA0012 mast). In addition to the frontal area, the pressure distribution obtained at a depth of 0.8 m to ensure no interference from the free surface shown in Figure 6.24

indicates a lower stagnation pressure and a reduced pressure gradient when compared to the pressure plot from the cylinder.

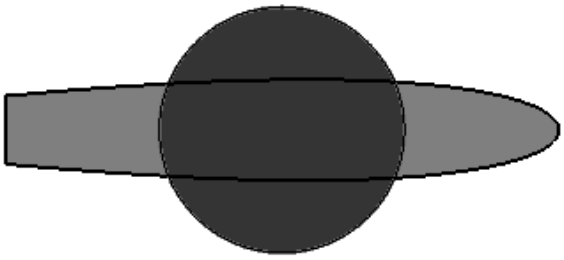

Figure 6.23: Shape comparison between cylinder and NACA0012 mast sections.

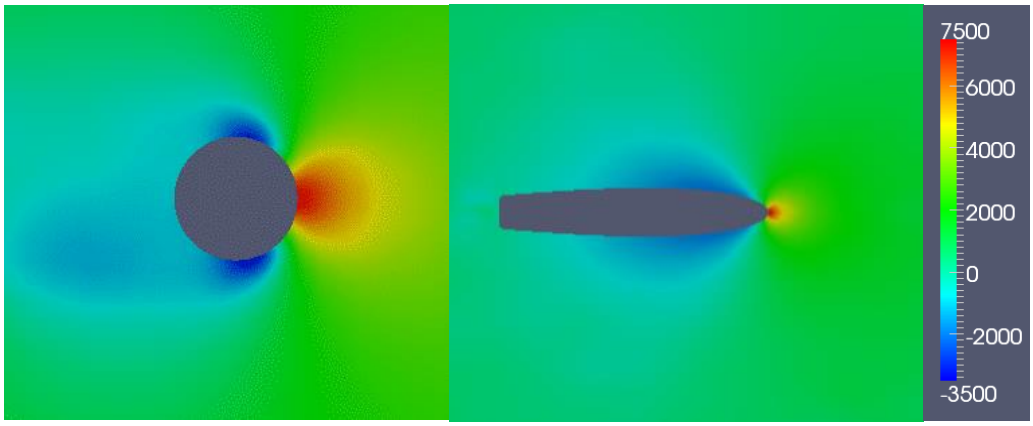

Figure 6.24: Pressure distribution (in pascal) around cylinder mast configuration (left) and NACA0012 mast configuration (right).

The pressure distribution shown above (Figure 6.25) can also be used to explain the large difference in percentage drag encountered on each mast between the double cylindrical mast and double NACA0012 configurations as seen in Figure 6.18 and 6.19. The drag generated by the forward cylindrical mast significantly impacts the aft mast whilst the NACA0012 section mast has a significantly reduced effect on the drag encountered by the aft mast.

6.9 Concluding remarks

Bluff bodies are required to pierce the free surface and travel at speed in ocean environments. Such motion can create significant plumes, drag and vibration. The plume profile generated by a series of mast configurations was numerically analysed using LES simulations and validated against experimental tow tank data conducted at the Australian Maritime College. Data for the bow wave height, plume length, plume height and drag was collected and analysed to assess the potential benefits from a double mast configuration and NACA0012 masts compared to a conventional single cylindrical mast.

It was shown that the plume structure generated by a cylinder can be accurately modelled numerically with a difference of 5% at Fr=3.5 for the bow wave height with smaller variations between the results at lower speeds. Furthermore, there was a correlation found in the drag data with an exception at Fr=3.25 where the numerical results did not capture the same lower drag coefficient (C_D) as the experimental data at Fr=3.25. It was also noted that both the numerical and experimental data showed a change in flow regime at Fr=2.25 as the C_D for the 1000 mm cylinder decreased below the C_D of the 200 mm cylinder. Additionally, the experimental results showed a dip in the C_D value at Fr=3.25 for the 1000 mm cylinder.

It was found that using a double cylindrical mast configuration can reduce the bow wave height by approximately 30% and the plume height by 18% when compared to a single mast geometry with the same total water plane area at high Froude numbers. Additionally, it was found that even a smaller forward mast has the ability to reduce the wake generated by a larger aft mast sufficiently such that the wake from the forward mast covers that from the larger aft mast.

The double mast geometry also generates a bow wave when compared to the truncated NACA0012 geometries. The streamlined NACA masts showed a huge reduction in bow wave height and hence would be a logical improvement over cylindrical masts. The changes in the bow wave height between the different mast geometries can partially be explained by the change in frontal area of the masts for the same waterplane area. Although the NACA sections showed a large benefit in these simulations, mast structures are often operating in current and waves and thus, due to the large chord length when compared to a

cylinder, could produce a larger wake if there was a significant cross-flow as the NACA section masts are not axial.

Future work could involve studying the effect of the ratio of the forward mast to aft mast diameter to determine at what ratio a smaller forward mast no longer has the benefit of reducing the plume size. If the forward masts was found to be extremely small, it could be possible to implement the small forward mast as a dummy mast. This would also involve assessing the effect of the distance between the two masts to determine the minimum and maximum effective gaps. Additionally, the possible disadvantages of implanting a streamlined body due to current and waves, a study could be conducted to determine the possible increase in plume structure of a streamlined body at varying angles of attack.

Chapter 7

Examination of Numerical Results and Mesh Requirements

7.1 Introduction

Throughout this thesis, publications in refereed journals and conference proceedings were utilised to present the majority of results. However, some aspect of the numerical modelling and results were omitted from these chapters as they did not fit within the publications. This chapter presents the omitted information and data to complete the discussion on the modelling, results, and the associated analysis, and thereby address the overall objectives of the thesis rather than only the objectives of the individual publications.

The areas discussed in this Chapter are:

1. Under prediction of the bow wave height and plume size
2. Mesh requirements

The first significant aspect not discussed in the previous chapters is the reason for under prediction of the bow wave height and plume size. As mentioned in Chapters 3-6, the flow around a surface piercing cylinder can generate a large wake and bow wave when travelling at high Froude numbers. This chapter examines the flow fields and data generated by the numerical investigation to understand the cause for the differences in results between the numerical predictions and experimental measurements at higher Froude numbers.

The flow around a deeply submerged cylinder, without the presence of the free surface, is well studied for a wide range of Reynolds numbers explaining the flow regime surrounding the cylinder, including the transition from laminar to turbulent flow (Kawamura et al., 1986; Loc et al., 1985; Schäfer et al., 1996; Son et al., 1969). However, as discussed in the previous chapters, the flow around a circular cylinder piercing the free surface has not been studied as extensively and hence, limited data is available in the public domain with the most applicable experimental data presented in Chapters 3-6. Numerical investigations are extremely limited at Froude numbers greater than 1, Kawamura et al. (2002) being one example modelling the flow around a surface piercing cylinder up to Fr=0.8. Yu et al. (2008) used Large Eddy Simulation to model the bow wave height generated up to a Froude number of 3.0, however, significantly under predicted the wake at Froude numbers greater than 2.0.

Chapters 3 and 5 presented a selection of numerical simulations carried out in this project showing that Large Eddy Simulation (LES) can accurately model the bow wave and plume structure generated by a surface piercing cylinder up to a Froude number of 4.0. The predictions using this numerical technique were compared with the experimental data presented in Chapter 3. It was shown that the bow wave height was under predicted by approximately 8% at Fr=4.0 when compared to the experimental data presented in Chapter 4.

A significant contributing factor to the size of the bow wave height is the stagnation pressure, both shown in Figure 7.1, with the maximum possible height based on Bernoulli's equation due to the energy generated from the stagnation pressure as described in Equation 4.3 (Mentor, 1994). This applies to inviscid flow and thus has been shown to over predict the bow wave height when compared to experimental and numerical results, as shown in Chapter 3 at Froude numbers greater than 2.0. Therefore, by calculating the stagnation pressure through a simplified version of Bernoulli's principle, a comparison between the predictions obtained using Computational Fluid Dynamics (CFD) stagnation pressure and the theoretically calculated stagnation pressure can be obtained.

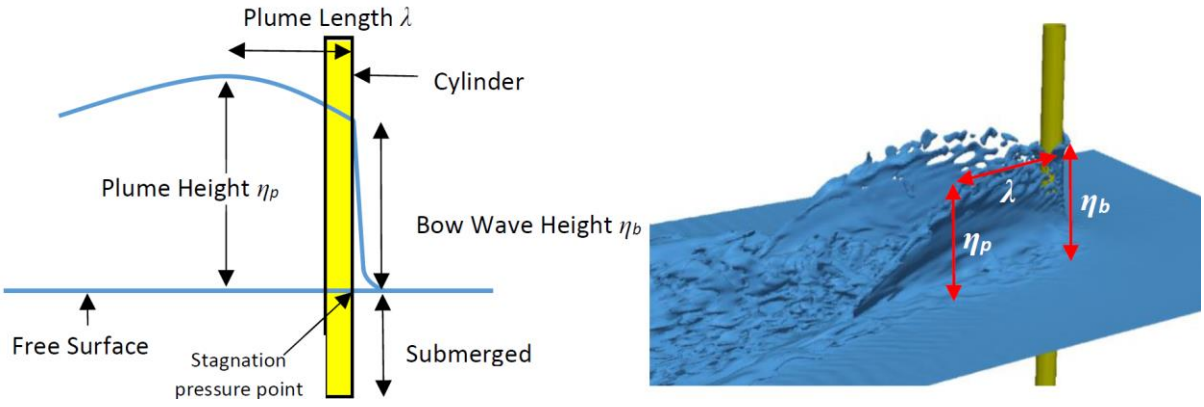

Figure 7.1: Definition of parameters used showing η_b, bow wave height, λ, plume length, and, η_p, plume height and location of stagnation point identified.

The second aspect discussed in this chapter is the mesh requirement which is not discussed in detail within the published papers. Specifically, the required aspect ratio (the ratio between the x-axis length and the y-axis length of a cell) in different regions of the

mesh to maximise the quality of the plume structure and the free surface. This was analysed by closely examining the free surface in three primary locations, which included the free surface and the plume structure.

7.2 Stagnation pressure

To evaluate the stagnation pressure predicted by the numerical simulations, it is first required to obtain the theoretical stagnation pressure. The method to calculate the expected stagnation pressure is using Bernoulli's equation. To use Bernoulli's equation, the assumptions are made that the flow is steady, incompressible and along a streamline is inviscid flow. Bernoulli's equation, once rearranged, can be expressed as,

$$P + \rho\frac{U^2}{2} + \rho g z = constant \tag{7.1}$$

where P is pressure, ρ is the fluid density, U is the fluid velocity, g is gravity, and z is the depth.

The first term, P, is the static pressure which does not incorporate dynamic effects. The second term, $\rho\frac{U^2}{2}$, is the dynamic pressure and represents the pressure as a result of the fluid being brought to a stop isentropically (i.e, no energy is lost). The final term, $\rho g z$, represents the hydrostatic pressure which is the pressure due to the weight of the fluid above the point of reference. Since stagnation pressure is the sum of static and dynamic pressures, and the static pressure is zero due to the depth being equal to zero (i.e. on the free surface), thus reducing equation (7.1) to give the stagnation pressure at any given speed as,

$$P_{stag} = \rho\frac{U^2}{2} \tag{7.2}$$

The calculated stagnation pressure can then be used to compare against the stagnation pressure predicted by the numerical simulations. The difference in stagnation pressure, predicted using CFD compared to calculated using equation (7.2), can then be compared to the ratio between numerical bow wave height and experimental bow wave

height. It should be noted that this could also be a Reynolds number investigation into flow around a cylinder, however, for the purpose of this investigation and the application to submarine masts, the Froude number was used as the independent variable. As simulations and experiments were conducted at full scale, the Reynolds number did not require scaling.

The numerical results produced by the LES model (Chapters 5 and 6) compared to the experimental results presented in Chapter 4 and 6 and the theoretical bow wave height based on Bernoulli's equation (Equation 4.3) are presented in Figure 7.2. As observed, Equation (4.3) significantly over predicts the bow wave height at higher Froude numbers (i.e. *Fr*>2). Furthermore an under prediction of the bow wave height can be seen in the LES predictions for Froude numbers greater than 3 with approximately 8% and 5% under prediction at Fr=4.0 and Fr=3.5 respectively. To better understand the reason for the under prediction of the bow wave height, the stagnation pressure is examined.

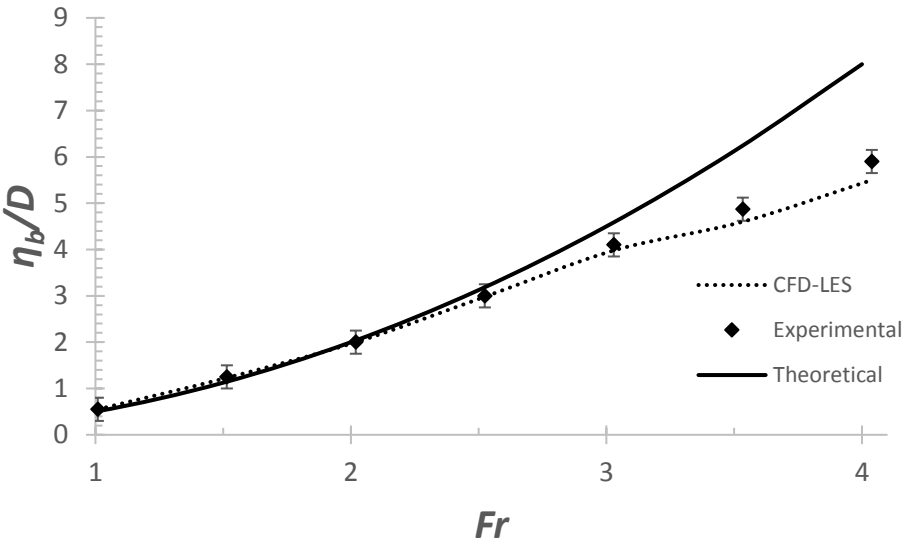

Figure 7.2: Bow wave height produced by surface piercing cylinder. Comparison between numerical (CFD-LES), experimental, and theoretical values based on Bernoulli equation.

The stagnation pressure obtained in the LES simulations was examined at the free surface by using the flow visualisation within the post processing software ParaView. These results were then compared to the theoretical stagnation pressures as calculated using Equation (7.2). An example of the pressure distribution around a circular cylinder at a

Froude number of 4.0 is shown in Figure 7.3 and Figure 7.4. Figure 7.3 shows a numerical prediction for a stagnation pressure of approximately 7600 N/m^2 while Figure 7.4 plots the non-dimensional pressure along the centre line of the domain forward of the cylinder at the free surface height. The non-dimensional pressure is calculated using equation (7.3). The comparison of this value across the Froude number range investigated against the theoretical stagnation pressure calculated by Equation (7.2) is shown in Figure 7.5. The calculated theoretical stagnation pressures are approximately 5% and 3.5% greater than the LES predicted stagnation pressures at *Fr*=4.0 at *Fr*=3.5 respectively. It is also noted that the difference in stagnation pressure at Froude numbers less than 3.5 is insignificant. As seen in Figure 7.2 and Figure 7.5, there is a strong correlation between the under prediction of bow wave height and the stagnation pressure.

$$P' = \frac{P}{2\rho U^2} \tag{7.3}$$

This under prediction in both the bow wave height and stagnation pressure indicates that energy is being dissipated within the numerical simulations at the Froude values analysed. Critically, this is the region in which the boundary layer is changing from sub-critical to critical flow as shown in Chapter 2 Table 2.1 (Sumer et al., 1997). Therefore, a potential loss of energy could be a result of incorrectly predicting the region in which turbulent flow begins within the boundary layer. As the volume of turbulent flow is greater at higher free stream velocities, there is an increase in the amount of energy dissipation occurring due to the dissipation rate calculated through the turbulence models (Sagol et al., 2012).

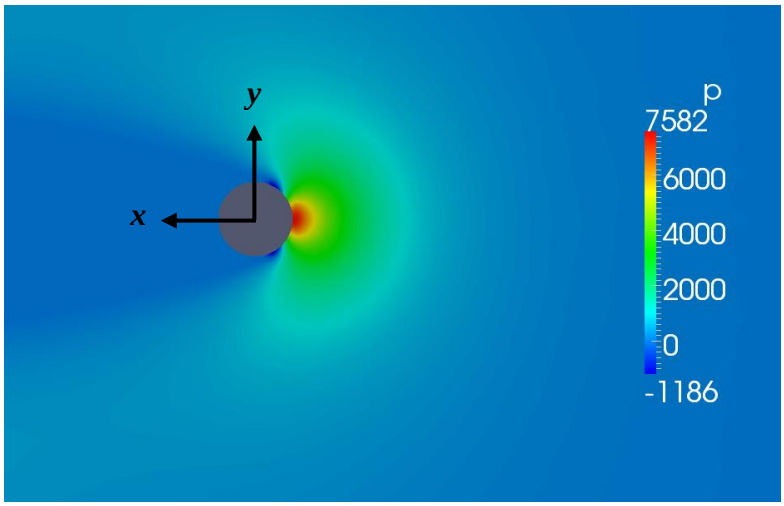

Figure 7.3: Pressure distribution on circular cylinder at the free surface level at Fr=4.0.

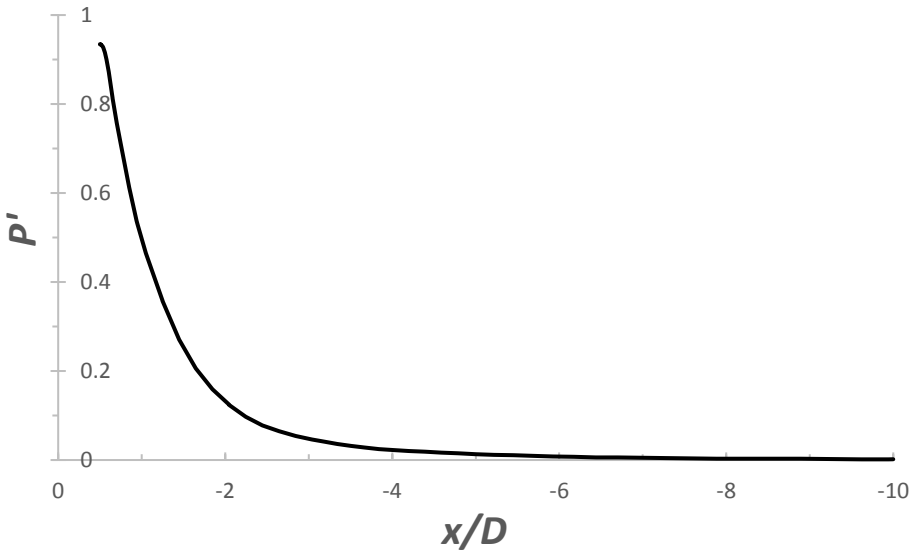

Figure 7.4: Non-dimensional pressure plot along y=0 and z=0 between x=0 and x=-1, i.e. pressure inline and forward of the cylinder.

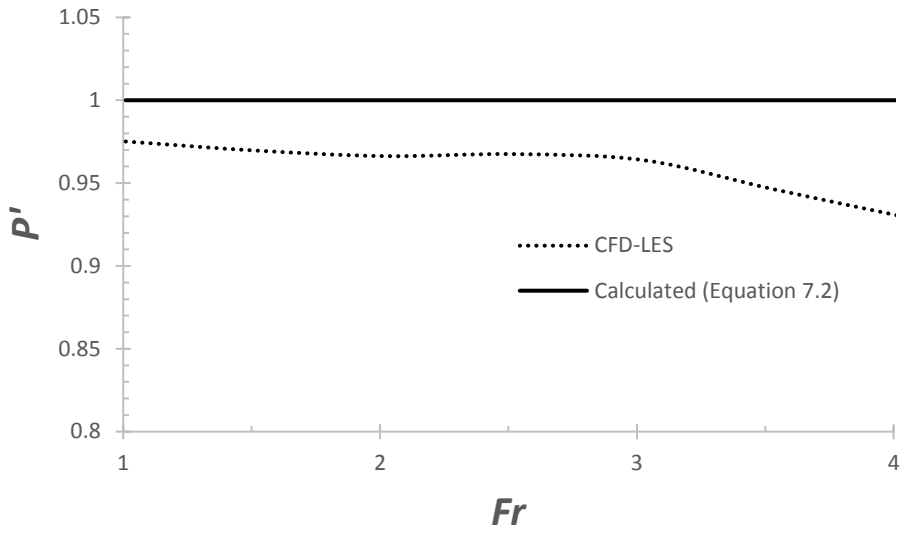

Figure 7.5: Comparison of non-dimensional stagnation pressure (P') between CFD-LES simulation predictions and Bernoulli's equation based calculations (Equation 7.2).

In addition to examining the stagnation pressure, the velocity of the water travelling in a vertical direction on the forward side of the cylinder can be recorded during the numerical simulations and examined. The vertical velocity (U_z) of the bow wave across the Froude number range was used to calculate the ratio of vertical speed to free stream velocity, i.e. the amount of horizontal velocity that has been converted to vertical velocity, as shown in Figure 7.6. The vertical velocity appears to be a function of Froude number with the exception of Fr<1.0. A possible reason for this could be due to less energy loss due to laminar flow. This linear trend can be clearly seen in Figure 7.6 where there is a constant ratio between the vertical and horizontal velocities around a ratio of 0.75 beyond Fr>1.0, which indicates that approximately 75% of the forward velocity of the cylinder in converted into vertical bow wave velocity. The latter at a Froude number of 4 is shown in Figure 7.7.

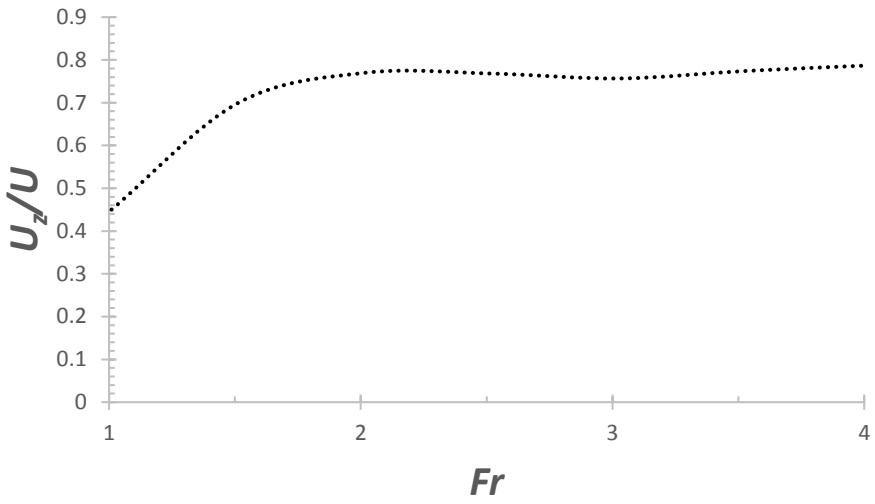

Figure 7.6: Ratio of vertical velocity (U_z) on the leading edge of the surface piercing cylinder compared to the velocity (U) of the free stream plotted as a function of Froude number.

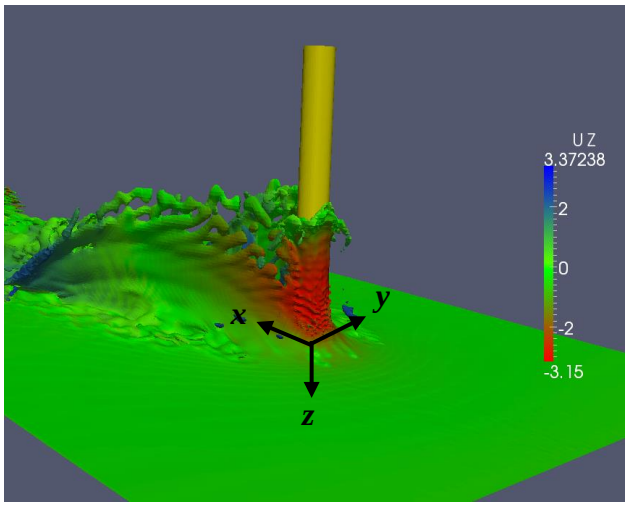

Figure 7.7: Numerical (CFD-LES) simulation of a cylinder piercing the free surface at Fr=4.0 showing the vertical velocity (U_z) of the bow wave. Note: Positive z-axis is down.

7.3 Mesh requirements

The mesh verification and validation was completed in the previous chapters (Chapter 3, 5 and 6). The discussion included the mesh density, refinement areas and y^+ requirements to capture the three parameters (bow wave height, plume length, and plume height) of the plume structure. The cell aspect ratio which significantly affected the spray and free surface quality were included in the development stages of the verification process, however not discussed due to publication requirements as mentioned in the Introduction (Section 7.1). Therefore, this section will cover the requirements for mesh cell aspect ratio within the refinement zones.

As the primary area of interest for this work was investigating the spray generated by the mast, the spray in the plume region was examined for detail in addition to overall size of the plume structure. Figure 7.8 shows two images of the plume structure with the same mesh density and numerical model as seen from behind the cylinder looking forward but focusing on the port side (left side) and thereby allowing for a closer examination of the spray, noting that both sides of the spray provided the same results. The only difference between the two simulations is the aspect ratio of the cells in the plume region.
Figure 7.8 (a) shows a mesh aspect ratio of one, i.e. cells were perfect cubes, whilst Figure 7.8 (b) shows the results using an aspect ratio of ¼. This clearly shows a 'stretching' of the spray in the y-axis when using an aspect ratio of ¼. Similarly, a stretching of the spray in the x-axis was noticed when aspect ratios greater than one were used. Therefore, to avoid distortions in the plume structure due to cell sizing region when compared to experimental spray, it was critical to use an aspect ratio of one in the plume. This is thought to be the case due to the post processing of the water and air volume fraction displaying the average across the cells, therefore, the water droplets will naturally take a similar shape to the cells in that region.

However, a uniform mesh aspect ratio could not be used throughout the numerical domain. As seen in Figure 7.9, if an aspect ratio of one is applied throughout the domain, a 'rippling' effect is noticed on the free surface. Therefore, whilst an aspect ratio of one was required for the plume region, an aspect ratio between two and three was required along the free surface to generate a smooth free surface obtained in Figure 7.7.

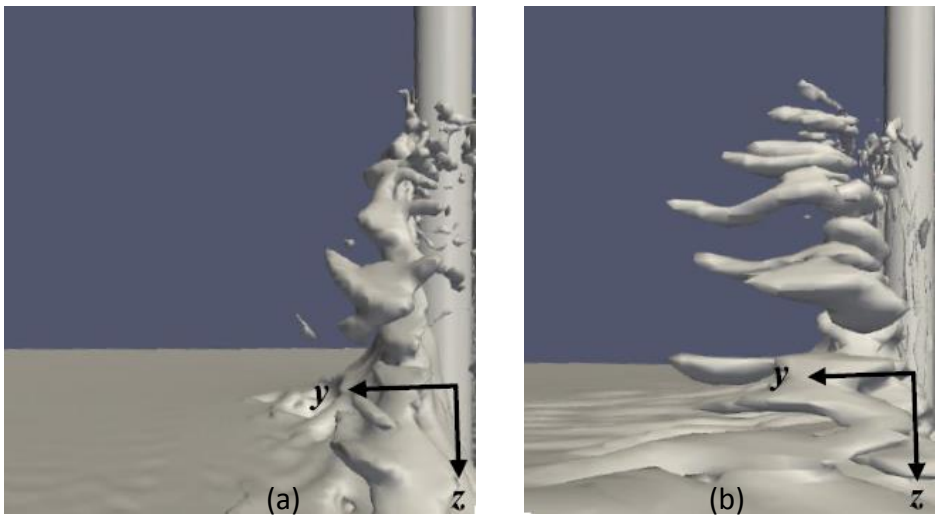

Figure 7.8: Close examination of the spray from the aft of the cylinder looking forward from the numerical prediction with a mesh cell aspect ratio of (a) one and (b) ¼.

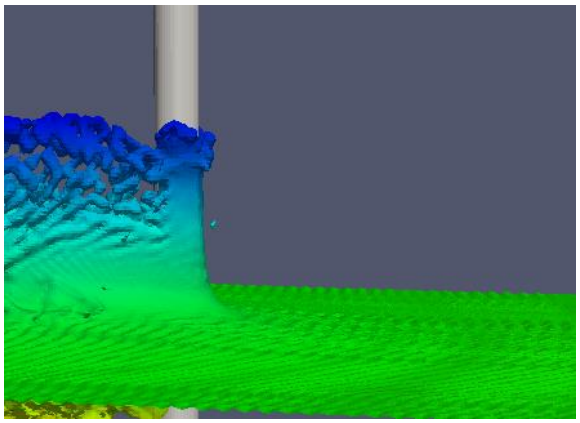

Figure 7.9: View of free surface 'ripples' caused by mesh aspect ratio one throughout the numerical domain at Fr=4.0. Colour represents elevation.

7.4 Concluding remarks

The flow around a surface piercing cylinder has been examined by focusing on the reasons behind the predictions of the bow wave height using the fact that the numerical simulations were lower than results measured experimentally using an LES model.

Whilst a very strong correlation was found between the numerical and experimental results in the bow wave height at Froude numbers lower than 3.0, an under prediction of the bow wave height was seen between Fr=3.0 and Fr=4.0 when comparing the numerical predictions to the experimental results. As mentioned by Mentor (1994), the stagnation pressure has a significant impact on the bow wave height and thus, the stagnation pressure was analysed to understand potential reasons for the under prediction of the bow wave height. The comparison between the LES predicted and theoretical stagnation pressure showed a similar correlation to the comparison between the LES prediction and the experimental measurement of the bow wave height. This strongly suggests that the under predictions noticed in the numerically predicted bow wave height compared to measured experimental data at high Froude numbers is a result of incorrectly modelling the stagnation pressure within the numerical simulations.

The velocity of flow in the vertical direction (U_z) of the bow wave was also studied allowing a correlation to be found between the forward velocity (x-axis) of the cylinder and U_z. Whilst at lower Froude numbers (Fr<1.0), the correlation between U_z and Froude number varied, at Froude numbers greater than 1.0, a linear correlation was found in which approximately 75% of the forward velocity of the cylinder was converted into vertical velocity (U_z) thus enabling the vertical component of the bow wave velocity to be predicted, based on forward velocity of the cylinder.

The mesh cell aspect ratio was also found to be critical in accurately modelling the plume structure and free surface. As a result of examining the spray with the plume structure and free surface, it was noted that an aspect ratio between two and three was required for the free surface, while an aspect ratio close to one was required within the region of the plume structure.

Chapter 8

Summary, Conclusions and Future Work

8.1 Summary

This project investigated the plume generated by a submarine mast whilst underway. This chapter provides an evaluation of the results and findings, as well as the contributions to the research field whilst addressing the aim of this thesis. The latter was to answer the research question: "*Can the plume structure generated by a submarine appendage piercing the free surface operating at snorkeling/periscope speeds be numerically accurately modelled with respect to the plume shape*?"

Successfully addressing the research question involved an incremental approach. The first stage involved a review of literature on both numerical and experimental methods and results on surface piercing bluff bodies. It was found that whilst there had been experimental research published, each set of data had limitations, such as cylinder immersion or low Froude numbers. Similarly for numerical simulations, there was a lack of published data investigating bluff bodies at the required Froude numbers to accurately replicate the conditions under which submarines operate with an extended periscope or snorkel. As the wake generated by the snorkel/periscope can result in the detection of the submarine, it is critical to understand and accurately model the plume structure.

Therefore, the focus of this thesis was to be able to predict the size of the plume, and to investigate geometries that could reduce the size of the plume. As part of this work, it was necessary to generate both numerical and experimental results for surface piercing bluff bodies, both of which had limited published data in the public domain. Following the literature review, CFD modelling techniques were assessed to determine the possibility of CFD to generate the plume structure and also which numerical technique was better suited for this purpose. As the experimental data was limited, a revised set of experimental data was generated, incorporating two cylinder lengths. Utilising the experimental data gathered, further numerical studies were conducted to validate the numerical code and analyse potential variations in mast geometry that would result in a reduction in plume size. However, further understanding of the flow around the cylinder, in particular the submerged end, was required to quantify the differences between experimental and real-world applications. Therefore, an additional set of experiments were conducted, including those with an end body, to reduce the effects generated by the submerged end of the

cylinder. This led to further in-depth numerical studies to quantify changes in the plume size due to end effects.

8.2 Concluding remarks

The research conducted in this thesis has generated the following conclusions:

8.2.1 Establishing an appropriate CFD model

Due to the unstable and complex flow generated by a bluff body, selecting an appropriate CFD model was critical. Various CFD models were tested with an extensive comparison conducted between URANS and LES models. Through using the same mesh, solvers and preconditioners for both simulations, the numerical models could be compared. A significant difference in the results were shown in certain areas, and it was concluded that the LES was the required numerical model. The primary reason for LES being selected over URANS was because the plume structure (i.e. the plume length and plume height) was not captured by the URANS model. Although the exact reason why the plume structure was not captured by URANS is not fully understood, it appears likely that the averaging of the flow cannot capture the instantaneous unsteady characteristics. LES was able to generate the entire plume profile, although the computational requirements, and hence simulation time, significantly increased. However, this was an acceptable increase in computational resources since modelling of the plume structure was essential.

8.2.1.1 LES model

One of the most critical aspects of an LES simulation is selecting the sub-grid model and thus a number of models were tested ultimately leading to the selection of the one-equation eddy model within the OpenFOAM package for the following reasons. Firstly, the one-equation eddy model calculates the SGS velocity scale independently, which is an

advantage over standard algebraic models. Secondly, whilst mixed models can potentially provide further benefits in calculating the SGS velocity scale, the increased complexity could lead to instabilities and inaccuracies in the results due to mesh sensitivity. Finally, published data suggests that the one-equation model performs well modelling vortex shedding.

8.2.2 Experimental results

Two sets of experiments were conducted in order to validate the CFD predictions. Additionally, completing the experiments in conjunction with numerical simulations assisted in the design of the experimental rig and increased confidence in the experimental data. The first set of experiments was used to generate experimental data to validate the numerical code and understand the flow physics. The information and knowledge thus gained were used to refine and design the second set of experiments, thus increasing the breadth and quality of the existing published data and enabling further validation of the numerical simulations.

The experimental and validation process using the first set of experimental data resulted in the following two key findings:

- The investigation focused on two different immersions depths, one which replicated published data at an immersion depth equal to twice the diameter (T'=2) and the other at a much greater immersion depth of ten times the diameter (T'=10). This was performed to assess whether an immersion variation from T'=2 to T'=10 significantly affected the final measurement of the plume geometry. A change in plume geometry at these immersion depths indicated a change between the existing experimental data and real world data. At the deeper immersion depth, the plume size was approximately 8% larger in comparison to that with the shorter immersion depth. This showed that end effects resulted in a significant reduction in plume size, therefore, further research was required to establish methods in which experiments could be conducted to remove end effects.

- When the plume flow characteristics were studied using the recorded video, it was discovered that the plume structure, which was previously published as a solid structure, is generated by two separate flow regimes. The forward half of the plume structure is generated by the bow wave, whilst the aft section of the plume is generated from the submerged end of the cylinder.

Whilst the second set of experiments provided essential data for CFD validation, the modifications carried out in light of the findings from the first experiment, and the numerical study provided the following two additional findings:

- The average frequency of oscillation of the bow wave height did not vary for the range of Froude numbers and immersion depths tested.
- The addition of a body at the submerged end of the cylinder generated similar plume dimensions as the cylinder with T'=10 immersion. This showed that a suitable end body, such as the one used in the second experiment, can be used in experiments to remove the experimental limitations.

8.2.3 Numerical results

Using the established LES numerical model, the results from the experimental data were used to validate numerical results and further increase the information with regard to the plume generated by surface piercing cylinders. This was completed in several stages.

8.2.3.1 Single mast validation

The numerical code was validated for the same configuration as that used in the first experiment, with both immersion depths used for validation purposes. With changes in the mesh aspect ratio, mesh density and small changes to solvers and pre-conditioners, the plume accuracy was improved to provide good correlation between experimental and numerical data. However, a small under prediction of the bow wave height and plume height was recorded for the higher Froude numbers (Fr>3.0). Analysis of the numerical and

experimental data provided a probable cause for this under prediction due to a strong correlation between the under prediction of both the bow wave height and stagnation pressure, discussed later in section 8.2.3.4. Further validation was conducted using the drag data from the second experiment, which provided a further point for confidence in the numerical validation with a strong correlation across the Froude number range tested.

8.2.3.2 Double mast configuration

The validated CFD model allowed for numerical simulations of different geometries to be tested with the potential to reduce the wake generated by the mast. These consisted of numerically modelling three configurations of double cylindrical masts and two configurations of single and double NACA0012 cross sectional masts. In addition to the forward mast generating a significant wake region that reduced the drag on the aft mast, the plume structure generated by the forward mast covered the reduced plume and wake generated by the aft mast. This was found to be the case for all cylindrical mast configurations including when the forward mast was considerably smaller in diameter than the aft mast. The reduction in plume profile from each double mast configuration was directly related to the reduction in mast diameter of the forward mast compared to the single mast. This finding suggests that either splitting the mast into two masts, or adding a 'dummy' mast forward of the mast could reduce the overall plume size. Additionally, the NACA0012 sections provided a reduction of 75% in bow wave height when compared to the single cylindrical mast.

8.2.3.3 End effect validation and findings

As mentioned in the experimental results section, a major finding from this research involved the effect on the plume structure due to the addition of a body to the submerged end of the cylinder. Although this was noticed in the experimental data, it was essential that the numerical simulation accurately predicted the differences in plume structure due to different submerged end conditions. Although there was an under prediction in the plume

size predicted by the CFD model, the numerical prediction accurately modelled the same increase of approximately 8% with the addition of an end body to the T'=2 depth, as was recorded with the experimental data. Additionally, there was no significant difference in bow wave height or plume size between T'=2.0 with end body and T'=10.0 with and without the end body. Using the validated numerical code, an analysis was performed to assess the immersion depth required to remove the end effect on the plume structure. Using the data presented on the bow wave height and plume dimensions generated by a cylinder with different immersion depths ranging from T'=2.0 up to T'=10.0, it was identified that the critical immersion depth ratio required to remove an effect at a Froude number of 4.0 is T'=8.0.

8.2.3.4 Stagnation pressure and bow wave

There was a strong correlation between the under prediction of the bow wave height and the under prediction of the stagnation pressure. This indicated that the reason for the under prediction of the bow wave height at certain Froude numbers was due to an over dissipation of energy within the boundary layer around the mast. It was also shown that the vertical velocity (U_z) of the bow wave height correlates directly with the free stream velocity (U) above a Froude number of 1.0. The ratio of vertical speed to the forward speed (i.e. the vertical velocity divided by the free stream velocity, U_z/U) was shown to be 0.75, which allows the vertical velocity component of the bow wave height to be predicted based on the forward velocity of the submarine. It was also shown that a mesh aspect ratio of one is required within the plume region to ensure an accurate modelling of the plume spray.

8.3 Implications of this research

Both numerical and experimental approaches were carried out in this project to investigate the flow characteristics and plume structure generated by a submarine mast piercing the free surface. An in-depth understanding of conditions that affected the plume structure allowed an accurate real world modelling of the plume structure. This was

achieved without compromises associated with experimental or numerical limitations that were present in published data prior to this project.

The results presented in this thesis provide a detailed insight into the plume structure generated by a submarine mast and thus can be used as a guide to reduce the plume signature through design and/or operational conditions whilst the submarine is piercing the free surface with either a periscope or a snorkel.

The experimental work that was carried out is of significant value as there was extremely limited data published in the public domain previously. Additionally, there were no available publications found for experiments at the required Froude numbers and with the required immersion depth or end body configuration. Therefore, the data generated from the experiments in this thesis have allowed for the validation of the CFD models used in the study.

The CFD research completed during this thesis has displayed the capabilities of the CFD models to accurately predict the plume structure. The CFD simulations have investigated the required models, solvers, sub-grid scale, y^+ value, mesh density and mesh aspect ratios to accurately model the plume within the OpenFOAM software. The validated model has allowed for varying mast configurations to be investigated, which were not practically possible at the time of experimental testing.

The combination of numerical and experimental work has increased the data quality, allowed the development of a numerical technique which can be used to predict the plume size and shape generated by a periscope or snorkel piercing the free surface in realistic operational conditions, and provided a much greater understanding of the flow characteristics of a bluff body piercing the free surface. This numerical code can be used to:

- predict the plume size generated by submarines operating pericopes or snorkels;
- provide information to operators with regard to the size of the plume generated as a function of the submarine's forward speed;
- estimate the speed of submarines based on its plume size; and
- design periscopes/snorkels shape and configuration to reduce the size of the plume generated, and hence reduce signature.

Through both numerical and experimental investigations, the understanding of the plume structure generated by submarine masts and surface piercing cylinders was significantly improved. This included identifying requirements, such as end effect and mesh requirements, which can affect the results of experimental and numerical studies. Therefore, the knowledge gained from the research presented in this thesis can be of significant value to submarine mast design and operational procedures.

8.4 Future Work

The findings of this thesis could lead to several further investigations which would increase the understanding of the flow regime around surface piercing masts and decrease the plume structure generated by a submarine mast.

As shown in Chapter 5, streamlined bodies and double mast configurations can offer a significant advantage over conventional cylinders. Thus, the numerical investigation can be extended to cover streamlined body masts and mast fairings, to further reduce the plume structure and understand the limitations of using streamlined bodies instead of bluff bodies. However, additional experimental data would be required to validate the non-cylindrical mast sections. The loads calculated in this project during the experimental and numerical analysis can be used to develop experimental set-ups to validate the double mast configurations, thus increasing the certainty of the numerical predictions.

Furthermore, the knowledge obtained through the CFD predations can be applied to other high Froude number situations, such as vertical rudder struts or foils, to optimise and increase performance of vessels with surface piercing configurations, such as hydrofoilers.

In addition to studying different mast configurations, analysis on the transition point of laminar to turbulent flow on bluff bodies at the respective Froude numbers has the potential to improve the accuracy of the plume structure and bow wave height.

Finally, an investigation into the performance of different numerical models could decrease the simulation time or increase the accuracy of the results. In particular, the URANS models discussed in Chapter 3 to determine the reasons for the limitations in capturing the full plume structure could be examined more accurately.

References

Avital, E. J., Yu, G. X., & Williams, J. (2009). Computation of the Flow and near Sound Fields of a Free Surface Piercing Cylinder. *Journal of Computational Acoustics, 17*(4), 365-382. Retrieved from <Go to ISI>://000274462200003

Bardina, J. E., Huang, P. G., & Coackley, T. J. (1997). Turbulence Modeling Validation, Testing, and Development. *NASA Technical Memorandum 110446*.

Boysan, H. F., Choudhury, D., & Engelman, M. S. (2009). Commercial CFD in the Service of Industry: The First 25 Years. In E. H. Hirschel & E. Krause (Eds.), *100 Volumes of 'Notes on Numerical Fluid Mechanics': 40 Years of Numerical Fluid Mechanics and Aerodynamics in Retrospect* (pp. 451-461). Berlin, Heidelberg: Springer Berlin Heidelberg.

Cabot, W., Jimenez, J., & Baggett, J. S. (1999). *On wakes and near-wall behavior in coarse large-eddy simulation of channel flow with wall models and second-order finite-difference methods*. Retrieved from

Cathcart, S. (2014). *Experimental and numerical analysis of flow around semi-submerged circular cylinders.* Universtiy of Tasmania, Australian Maritime College.

Cengel, Y., & Cimbala, J. (2010). *Fluid Mechanics: Fundamentals and applications, Second Edition*. New York: McGraw Hill.

Chaplin, J. R., & Teigen, P. (2003). Steady flow past a vertical surface-piercing circular cylinder. *Journal of Fluids and Structures, 18*(3–4), 271-285. doi:http://dx.doi.org/10.1016/j.jfluidstructs.2003.07.009

Conway, A. S. T., Cathcart, S., Binns, J. R., Ranmuthugala, D., Renilson, M. R., & Anderson, B. (2016). Experimental analysis of surface piercing cylinders at high Froude numbers. *Journal of Fluids and Thermal Science*.

Conway, A. S. T., Ranmuthugala, D., & Binns, J. R. (2013). *Predicting surface wakes using LES and RANS-SST analysis*. Paper presented at the 2nd SIA Technology Conference, Adelaide, Australia.

Conway, A. S. T., Ranmuthugala, D., Binns, J. R., & Renilson, M. R. (2017a). The effect of geometry on the surface waves generated by vertical surface piercing cylinders with a horizontal velocity. *Journal of Engineering for the Maritime Environment*.

Conway, A. S. T., Ranmuthugala, D., Binns, J. R., Renilson, M. R., & Anderson, B. (2017b). The end effect of vertical axis surface piercing cylinders with and without an end body. *(Submitted) Journal of Fluids and Thermal Science*.

DailyMail, R. (2012). Condemned to a watery grave: Dramatic moment U.S. Navy ship is sunk by torpedo from Australian submarine during target practice. *Daily Mail*.

Dawson, E. (2014). *An Investigation into the Effects of Submergence Depth, Speed and Hull Length-to-Diameter Ratio on the Near Surface Operation of Conventional Submarines* (Master of Philosophy), University of Tasmania.

de Villiers, E. (2006). *The Potential of Large Eddy Simluation for the Modeling of Wall Bounded Flows.* Imperical College of Science, Technology and Medicine.

Foundation, O. (2013). User Guide (Vol. 2.2.0): OpenFOAM Foundation.

Fureby, C., Gosman, A. D., Tabor, G., Weller, H. G., Sandham, N., & Wolfstein, M. (1997). Large eddy simulation of turbulent channel flows. *Turbulent shear flows, 11*.

Group, T. M. (2011). HMS Astute, the Royal Navy nuclear submarine is powered with a nuclear reactor the size of a dustbin.

Hay, A. D. (1947). *Flow about semi-submerged cylinders of finite length*. Retrieved from Princeton University:

Hernandez, R. H., Baudet, C., & Fauve, S. (2000). Controlling the B´enard-von K´arm´an instability in the wake of a cylinder by driving the pressure at the front stagnation point. *The European Physical Journal B, 14*, 773-781.

Hsieh, T. (1964). Resistance of cylindrical piers in open channel flow. *Journal of the Hydraulics Division, 90*, 161-173.

ITTC. (2014). *ITTC - Recommended Procedures: Guide to the Expression of Uncertainty in Experimental Hydrodynamics.* Paper presented at the International Towing Tank Conference.

Kawamura, T., Mayer, S., Garapon, A., & Sørensen, L. (2002). Large eddy simulation of a flow past a free surface piercing circular cylinder. *Journal of Fluids Engineering, Transactions of the ASME, 124*(1), 91-101. doi:10.1115/1.1431545

Kawamura, T., Takami, H., & Kuwahara, K. (1986). Computation of high Reynolds number flow around a circular cylinder with surface roughness. *Fluid Dynamics Research, 1*(2), 145-162. doi:http://dx.doi.org/10.1016/0169-5983(86)90014-6

Kolmogorov, A. N. (1991). The Local Structure of Turbulence in Incompressible Viscous Fluid for Very Large Reynolds Numbers. *Proceedings: Mathematical and Physical Sciences, 434*(1890), 9-13. Retrieved from http://www.jstor.org/stable/51980

Lang, A. W., & Gharib, M. (2000). Experimental study of the wake behind a surface-piercing cylinder for a clean and contaminated free surface. *Journal of Fluid Mechanics, 402*, 109-136. Retrieved from <Go to ISI>://000085161800005

Loc, T. P., & Bouard, R. (1985). Numerical solution of the early stage of the unsteady viscous flow around a circular cylinder: a comparison with experimental visualization and measurements. *Journal of Fluid Mechanics, 160*, 93-117. doi:10.1017/S0022112085003408

Menter, F. R., & Egorov, Y. (2010). The Scale-Adaptive Simulation Method for Unsteady Turbulent Flow Predictions. Part 1: Theory and Model Description. *Flow, Turbulence and Combustion, 85*(1), 113-138. doi:10.1007/s10494-010-9264-5

Mentor, F. R. (1994). Two-Equation Eddy-Viscosity Turbulence Models for Engineering Applications. *AIAA Journal, 32*(8), 1598-1605.

Metcalf, B., Longo, J., Ghosh, S., & Stern, F. (2006). Unsteady free-surface wave-induced boundary-layer separation for a surface-piercing NACA 0024 foil: Towing tank experiments. *Journal of Fluids and Structures, 22*(1), 77-98. doi:http://dx.doi.org/10.1016/j.jfluidstructs.2005.09.004

Neckel, T. (2009). *The PDE Framework Peano: An Environment for Efficient Flow Simulations.* Technischen Universit at Munchen.

OpenFOAM-Foundation. (2013). User Guide (Vol. 2.2.0): OpenFOAM Foundation.

Penttinen, O. (2011). A pimpleFoam tutorial for channel flow, with respect to different LES models. Chalmers University of Technology.

Piomelli, U., Scotti, A., & Balaras, E. (2001). *Large-Eddy Simulations of Turbulent Flows, from Desktop to Supercomputer*. Paper presented at the Selected Papers and Invited Talks from the 4th International Conference on Vector and Parallel Processing.

Raheja, I. (2001). On submerged stagnation points and bow vortices generation *Twenty-Third Symposium on Naval Hydrodynamics* (pp. 540-551). Washington, DC: The National Academies Press.

Reporter, D. M. (2012). Condemned to a watery grave: Dramatic moment U.S. Navy ship is sunk by torpedo from Australian submarine during target practice. Retrieved from http://www.dailymail.co.uk/news/article-2178197/Dramatic-moment-U-S-Navy-ship-sunk-torpedo-Australian-submarine-target-practice.html

Sagol, E., Reggio, M., & Ilinca, A. (2012). Assessment of Two-Equation Turbulence Models and Validation of the Performance Characteristics of an Experimental Wind Turbine by CFD. *ISRN Mechanical Engineering, 2012*, 10. doi:10.5402/2012/428671

Salim, S. M., Ong, K. C., & Cheah, S. C. (2011). *Comparison of RANS, URANS and LES in the Prediction of Airflow and Pollutant Dispersion* Paper presented at the Proceedings of the World Congress of Engineering and Computer Science, San Francisco, USA.

Schäfer, M., Turek, S., Durst, F., Krause, E., & Rannacher, R. (1996). Benchmark Computations of Laminar Flow Around a Cylinder. In E. H. Hirschel (Ed.), *Flow Simulation with High-Performance Computers II: DFG Priority Research Programme Results 1993–1995* (pp. 547-566). Wiesbaden: Vieweg+Teubner Verlag.

Slaouti, A., & Gerrard, J. H. (1981). An experimental investigation of the end effects on the wake of a circular cylinder towed through water at low Reynolds numbers. *Journal of Fluid Mechanics, 112*, 297-314.

Smagorinski, J. (1963). General circulation experiments with the primitive equations. *Monthly Weather Review, 91*(3).

Son, J. S., & Hanratty, T. J. (1969). Numerical solution for the flow around a cylinder at Reynolds numbers of 40, 200 and 500. *Journal of Fluid Mechanics, 35*(2), 369-386. doi:10.1017/S0022112069001169

Sumer, B. M., & Fredsoe, J. (1997). *Hydrodynamics around cylindrical structures* (Vol. 12). Singapore: World Scientific Publishing Co. Pte. Ltd.

Sumner, D. (2010). Two circular cylinders in cross-flow: A review. *Journal of Fluids and Structures, 26*(6), 849-899. doi:http://dx.doi.org/10.1016/j.jfluidstructs.2010.07.001

Tritton, D. J. (1988). *Physical fluid dynamics / D.J. Tritton*: Oxford [England] : Clarendon Press, 1988. 2nd ed.

Verhoeven, O. (2011). *Trailing Edge Noise Simulations using IDDES in OpenFOAM.* (Masters of Science), Delft University of Technology.

Wickramasinghe, D., & Wilkinson, R. H. (1997). Wakes and Waves Generated by Surface Piercing Cylinders.

Xing, T., Kandasamy, M., Wilson, R., & Stern, F. (2004). *DES and RANS of Unsteady Free-Surface Wave Induced Seperation*. Paper presented at the 42nd Aerospace Sciences Meeting and Exhibit, Reno, Nevada.

Yoshizawa, A., & Horiuti, K. (1985). A statistically-derived subgrid-scale kinetic energy model for the large-eddy simulation of turbulent flows. *Journal of the Physical Society of Japan, 54*(8), 2834-2839. Retrieved from http://www.scopus.com/inward/record.url?eid=2-s2.0-0022112910&partnerID=40&md5=14be9eccb8da47ebf88b470e6232d823

Young, M. E., & Ooi, A. (2007). *Comparative Assessment of LES and URANS for Flow Over a Cylinder at a Reynolds Number of 3900*. Paper presented at the 16th Australasian Fluid Mechanics Conference, Gold Coast, Australia.

Yu, G., Avital, E. J., & Williams, J. J. R. (2008). Large eddy simulation of flow past free surface piercing circular cylinders. *Journal of Fluids Engineering-Transactions of the Asme, 130*(10). doi:Artn 101304 Doi 10.1115/1.2969462

Yun, K. B. (2014). *Boundary Conditions - OpenFOAM-2.3.0*.

Appendix I

Uncertainty Analysis of the Experimental Data

The principal values and calculations used for the uncertainty analysis of the experimental data presented in Chapter 6 are presented here. The ITTC Recommended Procedures – Guide to the Expression of Uncertainty in Experimental Hydrodynamics section 14.3 (ITTC, 2014) were used to determine the total uncertainty factor of 1.96 (95% confidence) applied to the standard deviation. The two approaches recommended by ITTC were both utilised.

For the first approach, runs for Froude numbers 1.0, 2.5 and 4.0 were completed three times with the bow wave height recorded at five individual times per run. The results from this approach can be seen in Table I.1.

For the second approach, the same equations of determining the total certainty at 95% confidence was used. However, the data was collected using a single run and video footage to record the bow wave height. The bow wave height was recorded 25 times per second with the mean and standard deviation calculated. The data from the video analysis is presented in Figures I.1-I.3 with a summary of the data in Table I.2.

The greater % uncertainty from the two methods (Table I.1 and I.2) was used during the thesis.

Table I.1: Summary of uncertainty analysis from the first approach with a 95% certainty for Froude numbers 1.0, 2.5 and 4.0 using an average recorded from three runs and five measurements per run.

Fr	1.0	2.5	4.0
$\bar{q}$	44.1	291.8	598.2
s^2	16.8	423.2	637.5
% Uncertainty	2.3	1.8	1.0

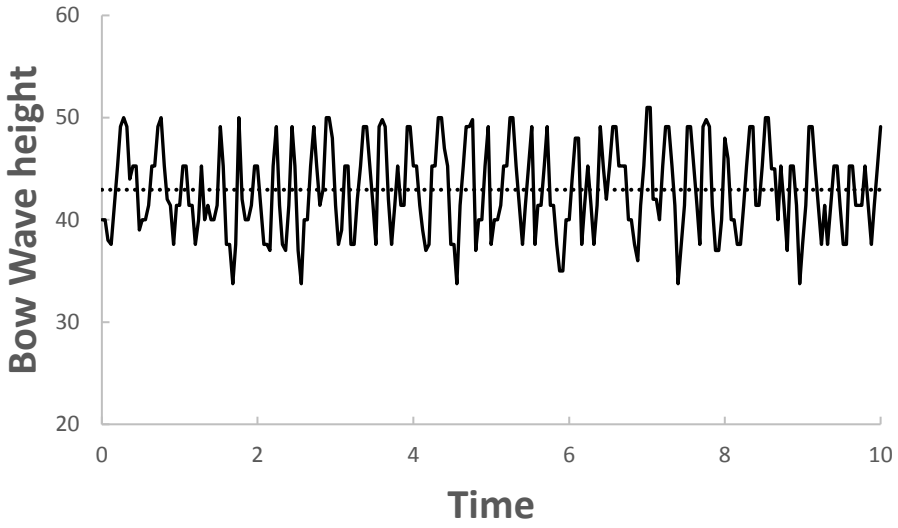

Figure I.1: Experimental bow wave height and mean bow wave height at Fr = 1.0 over a 10 second period.

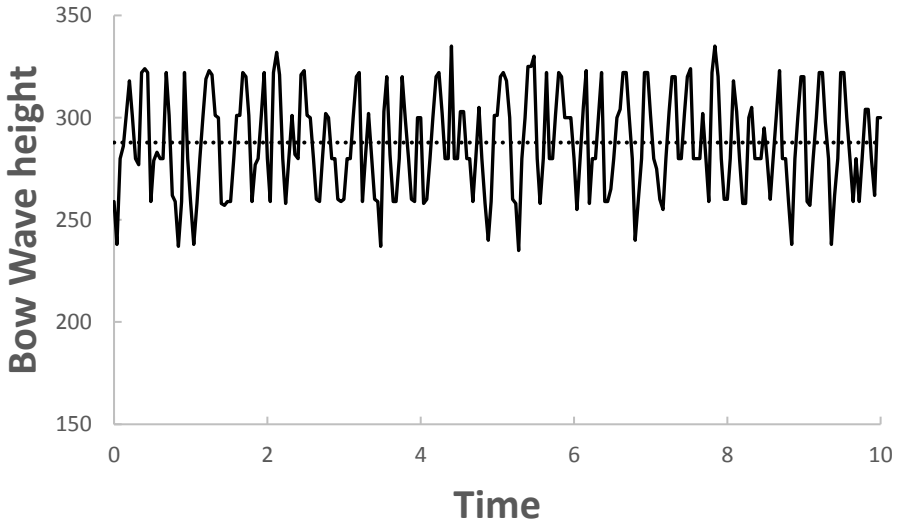

Figure I.2: Experimental bow wave height and mean bow wave height at Fr = 2.5 over a 10 second period.

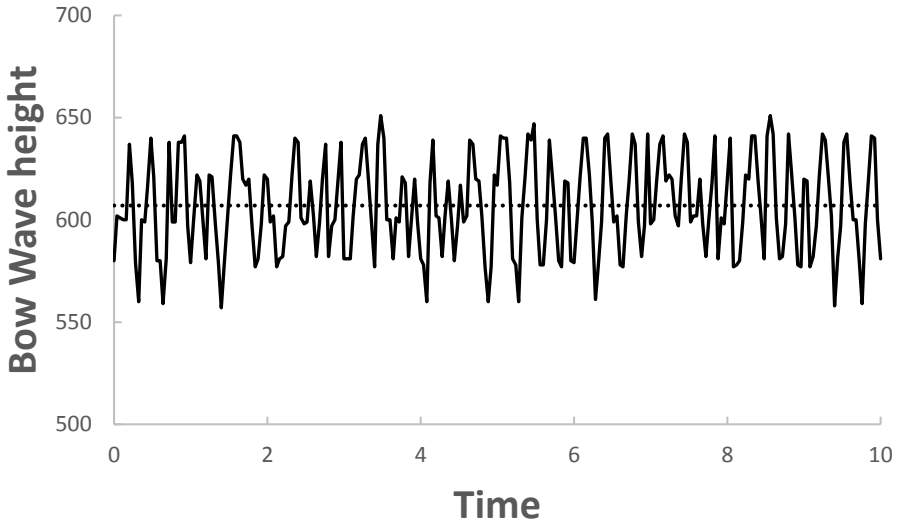

Figure I.3: Experimental bow wave height and mean bow wave height at Fr = 4 over a 10 second period.

Table I.2: Summary of uncertainty analysis from the second approach with a 95% certainty for Froude numbers 1.0, 2.5 and 4.0 using recorded bow wave height 25/second over 10 second period.

Fr	1.0	2.5	4.0
$\bar{q}$	42.9	287.8	607.0
s^2	18.9	601.9	537.8
% Uncertainty	2.5	2.1	0.9

Appendix II

Experimental and Numerical Analysis of Submarine Mast Surface Wakes

This conference paper has been presented in the "Pacific 2015 *International Maritime Conference*" and published in the Conference Proceedings. It is a summary of the data presented in Chapters 4 and 6 for the application in submarines. The citation for the research article is:

Conway, A. S. T., Ranmuthugala, D., Binns, J. R., & Renilson, M. R. (2015). Experimental and Numerical Analysis of Submarine Mast Surface Wakes. *Pacific 2015 International Maritime Conference.*

Appendix III

The Effect of Speed and Geometry on the Characteristics of the Plume Generated by Submarine Masts

This conference paper has been submitted to the "RINA Warship 2017" and will be published in the Conference Proceedings. It is a summary of the data presented in Chapters 5 and 6 for the application in submarines. The citation for the research article is:

Conway, A. S. T., Ranmuthugala, D., Renilson, M. R., & Binns, J. R. (2017). The Effect of Speed and Geometry on the Characteristics of the Plume Generated by Submarine Masts. *RINA Warship 2017.*

This appendix has been removed for copyright or proprietary reasons.